

**FLUORESCENCE AND EXCITED-STATE CONFORMATIONAL DYNAMICS OF
KETOCAROTENOIDS IN THE ORANGE CAROTENOID PROTEIN**

By

Jason Gurchiek

A DISSERTATION

Submitted to
Michigan State University
in partial fulfillment of the requirements
for the degree of

Chemistry—Doctor of Philosophy

2021

ABSTRACT

FLUORESCENCE AND EXCITED-STATE CONFORMATIONAL DYNAMICS OF KETOCAROTENOIDS IN THE ORANGE CAROTENOID PROTEIN

By

Jason Gurchiek

The Orange Carotenoid Protein (OCP) mediates nonphotochemical quenching (NPQ) mechanisms in cyanobacteria using a bound ketocarotenoid as a sensor of light intensity and as a quencher of phycocyanobilin excitons in the phycobilisome. During periods of high light intensity, the protein undergoes a conversion from a resting, orange state (OCP^O) to an active, red state (OCP^R) after optical preparation of the S₂ state of the ketocarotenoid. The mechanism by which this conversion is photochemically initiated remains an open question. We determined that the spectrum, polarization, and quantum yield of fluorescence from two examples of ketocarotenoids bound in OCP^O, 3'-hydroxyechinenone and canthaxanthin, reveal important details of the dynamics that follow optical preparation of the S₂ state. Additionally, by measuring the fluorescence emission anisotropy of a prototype carotenoid, β-carotene, we observed large-amplitude distortions after the S₂ state passes over a low activation-energy barrier that are consistent with twisting and pyramidalization near the center of the isoprenoid backbone. These results indicate that the ketocarotenoid is poised in OCP^O in a distorted conformation from which the photoactivation reaction is triggered by further excited-state torsional distortions of the conjugated polyene backbone.

Copyright by
JASON GURCHIEK
2021

for Brendan

ACKNOWLEDGMENTS

When I left the US navy 10 years ago, I wasn't exactly sure what path my life would take. I started talking to some career advisors who recommended that I should probably pursue a degree to improve my income potential. I followed that advice and eventually ended up writing this dissertation. I'd like to thank several of the individuals who supported and guided me along this path.

First, I'd like to thank my advisor, Professor Warren F. Beck, for inviting me to join your research group. We may not have always seen eye to eye, but you encouraged me and granted me the freedom to innovate and try new things. Under your guidance, I learned that I love the kinds of problem solving involved in designing and building a new instrument. Thank you.

I'd like to thank my undergraduate advisor, Professor P. Gregory Van Patten, for giving me my first introduction into academic research. Your mentorship is what drove me to consider continuing my education in graduate school. You motivated me to learn new things and broaden my horizons in ways that I never would have even considered alone. Thank you.

I'd also like to thank several of my colleagues from the Beck laboratory. Dan (Dr. Jerome Roscioli) and Dr. Soumen Ghosh, for the guidance you gave me when I was starting out. I learned so much from both of you. Thank you. Dr. Ryan Tilluck, for being the best friend I've ever had, for helping me through hard times, for nearly countless lunches at No Thai, and so many other things. Thank you for your friendship and support. Nila, Kunwei, Chase, Justin and Sourav, I wish you the best in your graduate and postgraduate careers. I've enjoyed working with you and I am excited to see how you carry the research forward.

I'm grateful to my committee members, Professors Marcos Dantus, Gary Blanchard, and Benjamin Levine, for their guidance and support during my graduate studies as well as their insightful questions.

I've been taught by some amazing professors during my studies and would like to thank them. I'd like to give a special thanks to Dr. Terrence Lee, Dr. Norma Dunlap, Dr. Scott Handy, Dr. Anatoliy Volkov, Dr. John McCracken, and Dr. Kathryn Severin for their support and encouragement in my studies.

Thank you to all of my wonderful friends that I've made on this journey. Thank you for the memories, the good times, the adventures, the advice, encouragement, and support over these years.

Finally, I'd like to thank my parents, Joe and Susan. Thank you for your support and endless encouragement. I would have never been able to make it this far without you. Thank you. I hope that I've made you proud.

The research described in this Dissertation in the Beck laboratory and some research assistantship stipends were principally supported by a research grant award (DE-SC0010847) from the Photosynthetic Systems program of the Chemical Sciences, Geosciences and Biosciences Division, Office of Basic Energy Sciences, Office of Science, U.S. Department of Energy. Additional support was provided by a collaborative research grant from the Chemistry of Life Sciences program of the U.S. National Science Foundation, award CHE-1904655.

TABLE OF CONTENTS

LIST OF TABLES	ix
LIST OF FIGURES	x
LIST OF SCHEMES	xvii
KEY TO ABBREVIATIONS	xviii
Overview of the Dissertation	1
Chapter 1. Introduction	3
1.1. Photophysics of Carotenoids	3
1.2. The Orange Carotenoid Protein	10
Chapter 2. Fluorescence and Excited State Conformational Dynamics of the Orange Carotenoid Protein	13
2.1. Summary	13
2.2. Introduction	14
2.3. Experimental Section	15
2.3.1. Sample Preparation	15
2.3.2. Spectroscopy	16
2.3.3. Structural Analysis	18
2.4. Results	18
2.4.1. Absorption and Fluorescence Lineshapes	18
2.4.2. System–Bath Coupling	22
2.5. Discussion	25
2.6. Conclusions	32
2.S. Supporting Information	33
2.S.1. Multimode Brownian oscillator (MBO) model	33
2.S.1.1. Introduction	33
2.S.1.2. Theory	33
2.S.1.3. Approach	36
2.S.1.4. Results	36
2.S.2. Numerical simulations of absorption and fluorescence spectra for OCPO with 3hECN using the Multimode Brownian Oscillator (MBO) model	38
2.S.3. Numerical simulations of absorption and fluorescence spectra for OCPO with CAN using the Multimode Brownian Oscillator (MBO) model	41
2.S.4. Absorption and Fluorescence Spectra from Canthaxanthin in Chloroform Solvent with Numerical Simulations	44
2.S.5. Comparison of ground-state absorption spectra for 3hECN-containing preparations of OCPO	45
2.S.6. Structure of the carotenoid binding site in OCPO	46

Chapter 3. Fluorescence anisotropy detection of barrier crossing and ultrafast conformational dynamics in the S2 state of β -carotene	49
3.1. Summary	49
3.2. Introduction	50
3.3. Experimental and Computational	51
3.3.1. Sample Preparation	51
3.3.2. Absorption spectroscopy	51
3.3.3. Fluorescence Spectroscopy	52
3.3.4. Electronic Structure Calculations	53
3.4. Results	54
3.4.1 Fluorescence Spectra	54
3.4.2. Fluorescence Anisotropy Spectra	56
3.4.3. Solvent dependence of the fluorescence emission and anisotropy from β -carotene	60
3.4.4. Temperature dependence of the fluorescence from β -carotene	67
3.4.5. DFT Calculations	75
3.5. Discussion	83
3.S. Supporting Information	92
3.S.1. Materials and Experimental Methods	92
3.S.1.1. Purification of β -carotene	92
3.S.1.2. Sample Handling for Fluorescence Spectroscopy	92
3.S.1.3. Linear Absorption Spectra	93
3.S.1.4. Fluorescence Instrumentation	93
3.S.1.5. Data Acquisition	95
3.S.1.6. Data Processing	96
3.S.1.7. Determination of Fluorescence Anisotropy	98
3.S.1.8. Rhodamine 6G reference spectra	99
3.S.1.9. Determination of Fluorescence Quantum Yield	100
3.S.1.10. Excitation wavelength dependence of the fluorescence emission and anisotropy wavelength spectra from β -carotene	102
3.S.2. MBO Simulations	112
REFERENCES	117

LIST OF TABLES

Table 2.1. Absorption and fluorescence spectral parameters for 3hECN and CAN in OCPO preparations and for CAN in chloroform solvent	24
Table 2S.2. MBO model parameters used for the simulation of the absorption spectra from 3hECN in OCP ⁰ in Figure 2S.2.	39
Table 2S.3. MBO model parameters used for the simulation of the absorption spectra from 3hECN in OCP ⁰ in Figure 2S.3.	40
Table 2S.4. MBO model parameters used for the simulation of the absorption spectra from CAN in OCP ⁰ in Figure 2S.4.	41
Table 2S.5. MBO model parameters used for the simulation of the absorption spectra from CAN in OCP ⁰ in Figure 2S.5.	42
Table 2S.6. MBO model parameters used for the simulation of the absorption spectra from CAN in OCP ⁰ in Figure 2S.6.	43
Table 2S.7. MBO model parameters for the simulation of the absorption and fluorescence spectra from CAN in trichloromethane solution.	44
Table 2S.8. Distances in OCP ⁰ crystal structures between protein groups to the carbonyl or hydroxyl substituents on the carotenoid β -cyclohexene rings.	47
Table 3.1. Fluorescence quantum yield and anisotropy parameters for β -carotene	66
Table 3.2. Permanent dipole moments and TDM rotations for the calculated β -carotene S ₂ structures	81
Table 3S.1. Energy gap time-correlation function parameters in the MBO model for the absorption spectrum from β -carotene in hexane at 296 K in Figure 3S.8.	114
Table 3S.2. Energy gap time-correlation function parameters in the MBO model for the absorption spectrum from β -carotene in 2-MTHF at 80 K in Figure 3.12a.	116
Table 3S.3. Energy gap time-correlation function parameters in the MBO model for the absorption spectrum from β -carotene in 2-MTHF at 296 K in Figure 3.12b.	117

LIST OF FIGURES

Figure 1.1. Schematic potential energy curves^{4,43,48} proposed for the singlet excited states of all-*trans*- β -carotene, as plotted with respect to a reaction coordinate for the structural response following optical preparation of the S_2 state. An activation-energy barrier (\ddagger) divides planar (BLA coordinates) and out-of-plane distorted (torsional and/or pyramidal coordinates, ϕ) regions of the potential energy surfaces. The S_2 and S_1 surfaces strongly interact at a CI seam near the S_2 minimum with respect to the ϕ coordinates. 7

Figure 1.2. Structures of the OCP and of its associated carotenoids. (Top) Structure in the resting, orange state (OCPO) from *Arthrospira maxima* (5UI2.pdb).⁵⁴ The N- and C-terminal domains (NTD and CTD, respectively) are rendered as red and grey ribbons; the peripheral N-terminal α helix and the linker between the NTD and CTD are rendered in green. The bound 3'-hydroxyechinenone (3hECN) is rendered as a stick structure, with carbon atoms in orange and oxygen atoms in red. (Bottom) Structures of the two ketocarotenoids discussed in this study, 3hECN and canthaxanthin (CAN). The *s*-cis and *s*-trans conformations of the β -cyclohexene end rings, as obtained by internal rotation with respect to the conjugated polyene backbone, are shown as fragments. 11

Figure 2.1. Room-temperature (23 °C) absorption (blue) and fluorescence (red) spectra of carotenoids in OCP⁰: (a) 3hECN; (b) CAN; and (c) CAN in chloroform solvent. The intensities are plotted as dipole strengths, $\epsilon(\nu)/\nu$ and $\lambda^2 F(\nu)/\nu^3$, respectively, with normalization to peak intensity. The excitation monochromator for the fluorescence was tuned to 500 nm (20000 cm^{-1}) for panels (a) and (b) and to 490 nm (20408 cm^{-1}) for (c). In panels (a) and (b), the asterisk at 16500 cm^{-1} marks the wavenumber of the nonresonant Raman band from water (shift of 3500 cm^{-1}). In panel (c), asterisks nonresonant Raman bands from the chloroform solvent at 17340, 19160, and 19640 cm^{-1} (shifts of 3034, 1220, and 774 cm^{-1}).⁹⁹ 21

Figure 2.2. Protein–ketocarotenoid hydrogen bonding interactions by the β_1 (CTD) and β_2 (NTD) β -cyclohexene rings of the carotenoids bound in OCP⁰: (a) for 3hECN, from structure 5UI2.pdb from *A. maxima*;⁵⁴ (b) for CAN, from structure 4XB5.pdb from *Synechocystis* sp. PCC 6803;⁶⁰ (c) detail from a rotated vantage point of the β_2 ring's hydrogen bonding interaction between the hydroxyl group and the carbonyl on Leu37 and (d) for the clash between the β_2 carbonyl on CAN and that on Leu37. Protons are not displayed in these diagrams. Figure 2S.9 shows the same views for 3hECN in the 5TV0.pdb structure from *Synechocystis* sp. PCC 6803,¹¹¹ which presents explicit protons. Table 2S.8 compares the distances from interacting protein groups for the β_1 and β_2 rings in the three structures. 27

Figure 2.3. Potential energy surfaces proposed for carotenoid chromophores in the OCP. The energies of the S_0 , S_1 , and S_2 states are plotted as a function of a reaction coordinate composed of motions of the conjugated polyene and β -cyclohexene end rings, first along C–C/C=C stretching coordinates and then by torsional or pyramidal out-of-plane distortions. Absorption (A) and fluorescence (F) transitions are marked. Progress along the reaction coordinate from the Franck–Condon structure of the carotenoid in OCP⁰ is depicted in terms of a series of Gaussian wavepackets, which broaden as displacement along the reaction coordinate increases due to the friction with the surrounding protein. 28

Figure 2S.1. Absorption (blue) and fluorescence (red data points) spectra of OCP⁰ measured at 23 °C with 3hECN incorporated as the bound carotenoid. The excitation monochromator for the fluorescence was tuned to 500 nm (20000 cm⁻¹). The intensities are plotted as dipole strengths, $\epsilon(\nu)/\nu$ and $\lambda^2 F(\nu)/\nu^3$, with normalization to peak intensity. The asterisk at 16500 cm⁻¹ marks the wavenumber of the nonresonant Raman band from water (shift of 3500 cm⁻¹). Superimposed on the experimental spectra are calculated absorption (blue dotted curve) and fluorescence (red dotted curve) spectra obtained from a numerical simulation with the multimode Brownian oscillator (MBO) model. The model parameters are listed below in Table 2S.2. This is the best model we obtained. The parameter choices obtain a good description of the vibronic structure observed in the absorption spectrum; the simulated fluorescence spectrum obtained with the same parameters exhibits approximately the same Stokes shift observed in the experimental spectrum, but the line width and vibronic structure is not well described. 38

Figure 2S.2. Absorption and fluorescence spectra of OCP⁰ measured at 23 °C with 3hECN incorporated as the bound carotenoid. The simulated spectra obtained here with the model parameters listed below in Table 2S.2 obtain a better description of the red onset of the absorption spectrum, in the 15000–17000 cm⁻¹ region; but the result is a much larger Stokes shift for the fluorescence than is observed. 39

Figure 2S.3. Absorption and fluorescence spectra of OCP⁰ measured at 23 °C with 3hECN incorporated as the bound carotenoid. The simulated spectra obtained here with the model parameters listed below in Table 2S.3 model the resolved vibronic structure using an alternate set of parameters. The vibronic features at peak absorption are well described, but these parameters produce a stronger 0–0 peak at 18500 cm⁻¹ than observed in the experimental spectrum. Also, the Stokes shift of the fluorescence is much larger than is observed. 40

Figure 2S.4. Absorption and fluorescence spectra of OCP⁰ measured at 23 °C with 3hECN incorporated as the bound carotenoid. The simulated spectra obtained here with the model parameters listed below in Table 2S.4 describe the best model we obtained for CAN in OCP⁰. As for the best model for 3hECN in OCP⁰ (Figure 2S.1), a good description of the vibronic structure observed in the absorption spectrum is provided by this model, but here the Stokes shift, line width, and vibronic structure is not well described. 41

Figure 2S.5. Absorption and fluorescence spectra of OCP⁰ measured at 23 °C with CAN incorporated as the bound carotenoid. The simulated spectra obtained here with the model parameters listed below in Table 2S.5 describe the red tail of the absorption spectrum pretty well, but the result is a much larger Stokes shift for the fluorescence than is observed. 42

Figure 2S.6. Absorption and fluorescence spectra of OCP⁰ measured at 23 °C with CAN incorporated as the bound carotenoid. The simulated spectra obtained here with the model parameters listed below in Table 2S.6 provide an alternate description of the vibronic structure. The vibronic features at peak absorption are well described, but these parameters produce a stronger 0–0 transition than observed. Also, the Stokes shift of the fluorescence is much larger than observed. 43

Figure 2S.7. Absorption and fluorescence spectra of CAN in chloroform solvent at 23 °C. The excitation monochromator for the fluorescence was tuned to 490 nm (20408 cm⁻¹). Asterisks mark nonresonant Raman bands from the chloroform solvent. The simulated spectra shown here were obtained with the parameters listed in Table 2S.7. 44

Figure 2S.8. Comparison of ground-state absorption spectra from OCP⁰ preparations from *Arthrospira platensis* containing 3hECN from the present work (Figure 2.1(a)) and from the Kirilovski⁵⁷ and Blankenship⁷⁰ laboratories. The spectra are normalized at the peak of the second vibronic peak to project out differences in the intensity of the first vibronic peak and of the red absorption onset. 45

Figure 2S.9. Alignment of the amino acid sequences in the NTD from *Arthrospira platensis* (Accession number YP_005071727) and *Arthrospira maxima* (from structure 5UI2.pdb). The NTD amino acid sequence is fully conserved over these two species. 46

Figure 2S.10. Protein–ketocarotenoid hydrogen bonding interactions in *Synechocystis* sp. PCC 6803 OCP⁰: (a) for 3hECN, from structure 5TV0.pdb; (b) detail from a rotated vantage point of the β_2 ring's hydrogen bonding interaction between the hydroxyl group and the carbonyl on Leu37. The crystal structure in this case explicitly includes hydrogen atoms for the carotenoid. For comparison with Figure 2.2. 46

Figure 2S.11. Conformation of the end rings of 3hECN (orange, top) and CAN (teal, bottom) in the 5UI2 (3hECN) and 4XB5 (CAN) crystal structures, respectively, as viewed from the (a,b) β_1 and (c,d) β_2 ends. The dihedral angle between the plane of the ring and the plane of the conjugated polyene backbone is indicated for each structure. 48

Figure 2S.12. As in Figure 2S.8, but for 3hECN in the 5TV0.pdb structure: as viewed from the (a) β_1 and (b) β_2 ends. 48

Figure 3.1. Absorption (blue) and fluorescence emission (red) spectra at four excitation wavelengths from β -carotene in hexane solvent at 23 °C. For the fluorescence spectra, the emission polarizer was oriented at the magic angle (54.6°) with respect to the excitation polarizer. The excitation wavelength is marked in each panel with a vertical dashed line. The positions of resonance Raman peaks from β -carotene ($\nu_1 = 1517$ cm⁻¹ and $\nu_2 = 1157$ cm⁻¹)¹³⁴ and for a non-resonance Raman peak from the hexane solvent ($\nu_A = 2966$ cm⁻¹)¹³⁵ are marked. 57

Figure 3.2. Fluorescence oscillator strength and anisotropy (r) spectra for β -carotene in hexane at 293 K: (a) with excitation at 490 nm ($20,400\text{ cm}^{-1}$); (b) with excitation at 430 nm ($23,250\text{ cm}^{-1}$). The magic-angle fluorescence oscillator strength (red) is plotted after correction for the intensity of the excitation light at the two wavelengths with the same intensity scaling in panels (a) and (b). The excitation wavenumber is marked in each panel with a vertical dashed line. The absorption oscillator strength (blue) is arbitrarily scaled to mirror that of the S_2 fluorescence emission line shape. A baseline for the S_1 emission is suggested by a lognormal lineshape for the red tail of the S_2 emission. F_{S_1} (purple) estimates the fraction of the fluorescence oscillator strength from the S_1 state; $F_{S_1} = 0.5$ is marked by the dashed line. The positions of resonance Raman peaks from β -carotene ($\nu_1 = 1517\text{ cm}^{-1}$ and $\nu_2 = 1157\text{ cm}^{-1}$)¹³⁴ and for a non-resonance Raman peak from the hexane solvent ($\nu_A = 2966\text{ cm}^{-1}$)¹³⁵ are marked. Also marked (*) is the second-order excitation light scattering peak. 58

Figure 3.3. Fluorescence oscillator strength and anisotropy (r) spectra for β -carotene in chloroform at 293 K: (a) with excitation at 500 nm ($20,000\text{ cm}^{-1}$); (b) with excitation at 435 nm ($23,000\text{ cm}^{-1}$). Other details are as indicated in the caption to Figure 3.2, including plotting the fluorescence oscillator strength spectra with the same intensity scaling in panels (a) and (b). The positions of resonance Raman peaks from β -carotene ($\nu_1 = 1517\text{ cm}^{-1}$ and $\nu_2 = 1157\text{ cm}^{-1}$)¹³⁴ and non-resonance Raman peaks from the chloroform solvent ($\nu_A = 2966\text{ cm}^{-1}$ and $\nu_B = 732\text{ cm}^{-1}$)¹⁴² are marked. 63

Figure 3.4. Fluorescence oscillator strength and anisotropy (r) spectra for β -carotene in 2-MTHF at 293 K: (a) with excitation at 495 nm ($20,200\text{ cm}^{-1}$); (b) with excitation at 430 nm ($23,250\text{ cm}^{-1}$). Other details are as indicated in the caption to Figure 3.2, including plotting the fluorescence oscillator strength spectra with the same intensity scaling in panels (a) and (b). The positions of resonance Raman peaks from β -carotene ($\nu_1 = 1517\text{ cm}^{-1}$ and $\nu_2 = 1157\text{ cm}^{-1}$)¹³⁴ and for a non-resonance Raman peak from the 2-MTHF solvent ($\nu_A = 2915\text{ cm}^{-1}$)¹⁴³ are marked. 64

Figure 3.5. Fluorescence oscillator strength and anisotropy (r) spectra for β -carotene in carbon disulfide at 293 K: (a) with excitation at 510 nm ($19,600\text{ cm}^{-1}$); (b) with excitation at 450 nm ($22,200\text{ cm}^{-1}$). Other details are as indicated in the caption to Figure 3.2, including plotting the fluorescence oscillator strength spectra with the same intensity scaling in panels (a) and (b). The positions of resonance Raman peaks from β -carotene ($\nu_1 = 1517\text{ cm}^{-1}$ and $\nu_2 = 1157\text{ cm}^{-1}$)¹³⁴ and for a non-resonance Raman peak from the CS_2 solvent ($\nu_A = 658\text{ cm}^{-1}$)¹⁴⁴ are marked. 65

Figure 3.6. Absorption (blue) and fluorescence (red) oscillator strength and anisotropy (r) spectra for β -carotene in 2-MTHF with excitation at 430 nm ($23,250\text{ cm}^{-1}$) at: (a) 80 K; (b) 120 K; (c) 200 K; and (d) 258 K. Other details are as indicated in the caption to Figure 3.2, including plotting the fluorescence oscillator strength spectra with the same intensity scaling in all four panels. In (d) the fluorescence oscillator strength is also replotted at $\times 50$ scaling. The positions of resonance Raman peaks from β -carotene ($\nu_1 = 1517\text{ cm}^{-1}$ and $\nu_2 = 1157\text{ cm}^{-1}$)¹³⁴ and for a non-resonance Raman peak from the 2-MTHF solvent ($\nu_A = 2915\text{ cm}^{-1}$)¹⁴³ are marked. 70

Figure 3.7. Comparison of the temperature dependences of (a) the minimum fluorescence anisotropy and (b) the quantum yield of fluorescence for β -carotene in 2-MTHF solvent with excitation at 430 nm. In (a), the trend of the fluorescence anisotropy measured for the emission from the spectral intermediate (Figure 3.6a–c) observed over the 80–200 K range (\bullet) is extended to compare with the anisotropy measured over the 258–296 K range for the S_2 (\square) and S_1 (\square) bands. Error bars report the \pm standard deviations over the sampled spectral regions. In the Arrhenius-style plot shown in (b), $E_a = 140 \pm 20 \text{ cm}^{-1}$ for 80–200 K (\bullet) and $E_a = 850 \pm 5 \text{ cm}^{-1}$ for 258–296 K (\circ).

74

Figure 3.8. (a) Minimum energy structure of β -carotene and of a truncated model, with a numbering scheme indicated (as also used in Scheme 1) for the carbon atoms in the isoprenoid backbone. (b) Optical transition densities for the $S_0 \rightarrow S_2$ absorption transition for the all-*trans* structure and for the C_{15} - $C_{15'}$ 90° -twisted structure. Orange/blue orbital colors denote an instantaneous gain or loss of electron density, respectively, upon excitation. Green arrows indicate the direction of the TDM with the vector origins drawn at the center of mass. (c) Calculated TDM rotations with respect to the all-*trans* structure as a function of the choice of the bond undergoing a 90° torsion for the $S_0 \rightarrow S_2$ absorption TDM, the latter for the truncated model. (d) Calculated rotations for the $S_0 \rightarrow S_2$ absorption and $S_2 \rightarrow S_0$ emission TDMs with respect to torsions of the C_{15} - $C_{15'}$ bond of β -carotene, the latter for the truncated model.

79

Figure 3.9. Modeled structures representing the Franck-Condon S_2 structure (gray), the 90° twisted conformer (yellow), and a conformer with a pyramidal distortion (light blue). The inset is a zoomed-in view of the circled region, which shows the modeled β -carotene pyramidal structure superimposed with the pyramidal structure of the CI of ethylene.¹⁵⁹

81

Figure 3.10. Orientations of the emission TDM vectors for the Franck-Condon S_2 state and those of the 90° twisted and pyramidal S_2 conformations with respect to the ground-state structure of β -carotene. The reference axis is the C_6 - C_6' vector.

82

Figure 3.11. Preliminary structural hypothesis for the photoswitching response in OCPO using the *Synechocystis* PCC 6803 (4xb5.pdb) structure. The resting CAN structure (orange) is superimposed with a hypothetical distorted S_2 structure (green) with torsions of the polyene along the C_9 - C_{10} , C_{11} - C_{12} , C_{13} - C_{14} , and C_{15} - $C_{15'}$ bonds. (b) Detail of the binding site, with protein surfaces tinted to indicate hydrophobic (blue), polar (pink), and charged/hydrophobic (red) residues.

91

Figure 3S.1. Schematic diagram of the home-built fluorescence spectrometer used in the present work. Symbols: DM, double monochromator; GTh, Glan-Thompson polarizer; GTa, Glan-Taylor polarizer; SP, grating spectrograph.

97

Figure 3S.2. Fluorescence emission anisotropy (top panel) and linearly polarized fluorescence emission spectra (bottom panel) from rhodamine 6G in glycerol at 23 °C with excitation at 532 nm. The angles indicated for the emission polarizer are with respect to the vertically polarized excitation polarizer. The green anisotropy trace was calculated conventionally using the F_0 and F_{90} spectra. The superimposed dotted anisotropy trace was calculated using the magic angle, $F_{54.7}$, and F_{90} spectra using equations 3S.1–3S.7. The red trendline in the >650 nm region of the anisotropy spectrum was used to calculate the minimum anisotropy value, 0.34 ± 0.003 . 101

Figure 3S.3. Parallel (F_{\parallel} , red) and perpendicular (F_{\perp} , blue) polarization components of the fluorescence emission and the fluorescence anisotropy (r) for β -carotene in hexane at 23 °C, with excitation at (a) 490 nm and (b) 430 nm. The anisotropy spectrum is superimposed with a smoothing spline trendline, with the red bolded section indicating the region used to estimate the minimum anisotropy and its confidence interval. The positions of resonance Raman peaks from β -carotene ($\nu_1 = 1517 \text{ cm}^{-1}$ and $\nu_2 = 1157 \text{ cm}^{-1}$)¹³⁴ and of a non-resonant Raman peak from the hexane solvent ($\nu_A = 2966 \text{ cm}^{-1}$)¹³⁵ are marked. 102

Figure 3S.4. Excitation wavelength (λ_{ex}) dependence of the fluorescence anisotropy for β -carotene in hexane solvent at 23 °C, with the trend indicated by a smoothing spline curve. The minimum anisotropy, r_{min} , was determined by averaging over the wavelength region marked in red. The highly polarized Raman scattering peak from the hexane solvent ($\nu_A = 2966 \text{ cm}^{-1}$)¹³⁵ is marked. 103

Figure 3S.5. Absorption (blue) and fluorescence emission (red) spectra at four excitation wavelengths from β -carotene in chloroform solvent at 23 °C. The emission polarizer was oriented at the magic angle (54.6°) with respect to the excitation polarizer for the fluorescence spectra. The excitation wavelength (dotted black line) and Raman scattering peaks from β -carotene ($\nu_1 = 1517 \text{ cm}^{-1}$ and $\nu_2 = 1157 \text{ cm}^{-1}$)¹³⁴ and from the chloroform solvent ($\nu_A = 2966 \text{ cm}^{-1}$ and $\nu_B = 732 \text{ cm}^{-1}$)¹⁴² are marked. 104

Figure 3S.6. Excitation wavelength (λ_{ex}) dependence of the fluorescence lineshape and anisotropy for β -carotene in chloroform solvent at 23 °C, with the trend indicated by a smoothing spline curve. The minimum anisotropy, r_{min} , was determined by averaging over the wavelength region marked in red. The highly polarized Raman scattering peak from the chloroform solvent ($\nu_A = 2966 \text{ cm}^{-1}$)¹⁴² is marked. 105

Figure 3S.7. Absorption (blue) and fluorescence emission (red) spectra at four excitation wavelengths from β -carotene in carbon disulfide solvent at 23 °C. For the fluorescence spectra, the emission polarizer was oriented at the magic angle (54.6°) with respect to the excitation polarizer for the fluorescence spectra. The excitation wavelength (dotted black line) is marked. Also marked (*) is the second-order excitation light scattering peak. 106

Figure 3S.8. Excitation wavelength (λ_{ex}) dependence of the fluorescence lineshape and anisotropy for β -carotene in carbon disulfide solvent at 293 K, with the trend indicated by a smoothing spline curve. The minimum anisotropy, r_{min} , was determined by averaging over the wavelength region marked in red. The highly polarized Raman scattering peak from the CS_2 solvent ($\nu_A = 658 \text{ cm}^{-1}$)¹⁴⁴ is marked. 107

Figure 3S.9. Absorption (blue) and fluorescence emission (red) spectra at four excitation wavelengths from β -carotene in 2-MTHF at 23 °C. For the fluorescence spectra, the emission polarizer was oriented at the magic angle (54.6°) with respect to the excitation polarizer for the fluorescence spectra. The excitation wavelength (dotted black line) and Raman scattering features from β -carotene ($\nu_1 = 1517 \text{ cm}^{-1}$ and $\nu_2 = 1157 \text{ cm}^{-1}$)¹³⁴ and from the 2-MTHF solvent ($\nu_A = 2915 \text{ cm}^{-1}$)¹⁴³ are marked. 108

Figure 3S.10. Excitation wavelength (λ_{ex}) dependence of the fluorescence anisotropy for β -carotene in 2-MTHF at 293 K, with the trend shown superimposed with a smoothing spline curve. The minimum anisotropy, r_{min} , was determined by averaging over the wavelength region marked in red. The highly polarized Raman scattering peak from the 2-MTHF solvent ($\nu_A = 2915 \text{ cm}^{-1}$)¹⁴³ is marked. 109

Figure 3S.11. Absorption, fluorescence emission, and fluorescence anisotropy spectra of β -carotene in 2-MTHF over the 80–296 K range. The absorption (blue) and fluorescence (red) spectra (left panel) are scaled relative to those at 80 K; autoscaled fluorescence spectra (red dotted) are superimposed to allow comparison of the emission line shapes. The fluorescence anisotropy spectra (right panel) are shown superimposed with a smoothing spline curve. The Raman scattering features from β -carotene ($\nu_1 = 1517 \text{ cm}^{-1}$ and $\nu_2 = 1157 \text{ cm}^{-1}$)¹³⁴ and from the 2-MTHF solvent ($\nu_A = 2915 \text{ cm}^{-1}$)¹⁴³ are marked. 110

Figure 3S.12. Absorption (blue) and fluorescence emission (red) spectra at 23 °C from β -carotene in hexane, plotted with arbitrary vertical scaling as relative oscillator strengths, $\epsilon(\nu)/\nu$ and $\lambda^2 F(\nu)/\nu^3$, respectively, as a function of the wavenumber ν . The fluorescence spectra were recorded with excitation at (a) 490 nm (20,400 cm^{-1}) and (b) 430 nm (23,260 cm^{-1}), as indicated by dotted black lines. The positions of resonance Raman peaks from β -carotene ($\nu_1 = 1517 \text{ cm}^{-1}$ and $\nu_2 = 1157 \text{ cm}^{-1}$)¹³⁴ and of a non-resonant Raman peak from the hexane solvent ($\nu_A = 2966 \text{ cm}^{-1}$)¹³⁵ are marked. Numerical simulations of the absorption and fluorescence emission oscillator strength spectra (blue and red dashed, respectively) using the MBO model are superimposed. The model parameters (Table 2S.1) were optimized to fit the experimental absorption spectrum; two exponential and two underdamped vibrational components were incorporated in the model, as previously implemented.¹¹⁹ 112

Figure 3S.13. Absorption (blue) and fluorescence emission (red) spectra at 296 K from β -carotene in 2-MTHF, plotted with arbitrary vertical scaling as relative oscillator strengths, $\epsilon(\nu)/\nu$ and $\lambda^2 F(\nu)/\nu^3$, respectively, as a function of the wavenumber ν . The sample temperature was maintained at (a) 80 K and (b) 296 K. The fluorescence spectra were recorded with excitation at 430 nm (23,300 cm^{-1}), as indicated by dotted black lines. The positions of resonance Raman lines from β -carotene ($\nu_1 = 1517 \text{ cm}^{-1}$ and $\nu_2 = 1157 \text{ cm}^{-1}$)¹³⁴ and of a non-resonant Raman line from the 2-MTHF solvent ($\nu_A, 2915 \text{ cm}^{-1}$)¹⁴³ are marked. Numerical simulations of the absorption and fluorescence emission oscillator strength spectra (blue and red dashed, respectively) using the MBO model are superimposed. The model parameters (Tables 2S.2 and 2S.3) were optimized to fit the experimental absorption spectrum at each temperature; two exponential and two underdamped vibrational components were incorporated in the model, as previously implemented.¹¹⁹ 114

LIST OF SCHEMES

Scheme 1. Structure of β -carotene

3

KEY TO ABBREVIATIONS

OCP	Orange Carotenoid Protein
NPQ	nonphotochemical quenching
OCP ^O	Orange Carotenoid Protein orange state
OCP ^R	Orange Carotenoid Protein red state
3hECN	3'-hydroxyechinenone
CAN	canthaxanthin
BLA	bond length alternation
CI	conical intersection
ESA	excited state absorption
PSB	protonated Schiff bases
SE	stimulated emission
ICT	intramolecular charge-transfer
NTD	N-terminal domain
CTD	C-terminal domain
RCP	Red Carotenoid Protein
EDTA	ethylenediaminetetraacetic acid
EGTA	(ethylene glycol-bis(β -aminoethyl ether)-N,N,N,N'-tetraacetic acid
MBO	multimode Brownian oscillator
TDM	transition dipole moment
HPLC	high-performance liquid chromatography
TD-DFT	time-dependant density functional theory
SADS	species associated difference spectrum

Overview of the Dissertation

The purpose of my dissertation is to address the photochemical mechanisms involved in the photoactivation of the Orange Carotenoid Protein (OCP). The OCP is a two domain protein with a bound ketocarotenoid which mediates nonphotochemical quenching (NPQ) mechanisms in cyanobacteria. The bound carotenoid serves both as a sensor of mid-visible light intensity and as a quencher of phycocyanobilin excitons in the phycobilisome. Upon the optical preparation of the carotenoid S_2 state, the conversion of the protein from a resting, orange state (OCP^O) to an active, red state (OCP^R) is triggered.

In my dissertation, we employed several fluorescence studies in order to probe the carotenoid excited state and learn about the details of the photophysics involved which lead to the photoactivation from OCP^O to OCP^R . The intent of these studies was to test the hypothesis that torsional distortions of the conjugated polyene backbone of the ketocarotenoid in OCP^O trigger the subsequent response.

In the first study, we report that the fluorescence spectrum and quantum yield of the bound carotenoids in OCP^O report important details of the motions that follow optical preparation of the S_2 state. The fluorescence spectra from OCP^O preparations containing 3'-hydroxyechinenone (3hECN) or canthaxanthin (CAN) are markedly mirror asymmetric with respect to the absorption line shape and more than an order of magnitude more intense than for carotenoids in solution. These results strongly suggest that large-amplitude motions of the carotenoid's β 2-cyclohexene ring and of the conjugated polyene backbone are involved in the photochemistry of OCP^O .

In the second study, we carried out a series of fluorescence lineshape and anisotropy measurements with a prototype carotenoid, β -carotene, in four aprotic solvents to probe the

structural mechanisms that promote nonradiative decay of the S_2 state to the S_1 state. The anisotropy values observed in the fluorescence emission bands originating from the S_2 and S_1 states reveal that large internal rotations of the emission transition dipole moment are initiated during ultrafast evolution on the S_2 state potential energy surface and persist upon nonradiative decay to the S_1 state. Electronic structure calculations of the orientation of the transition dipole moment account for the anisotropy results in terms of torsional and pyramidal distortions near the center of the isoprenoid backbone. The excitation wavelength dependence of the fluorescence anisotropy indicates that these out-of-plane conformational motions are initiated by passage over a low activation energy barrier from the Franck–Condon S_2 structure. This conclusion is consistent with detection over the 80–200 K range of a broad, red-shifted fluorescence band from a dynamic intermediate evolving on a steep gradient of the S_2 state potential energy surface after crossing the activation barrier. The temperature dependence of the oscillator strength and anisotropy indicate that nonadiabatic passage from S_2 through a conical intersection seam to S_1 is promoted by out-of-plane motions of the isoprenoid backbone with strong hindrance by solvent friction.

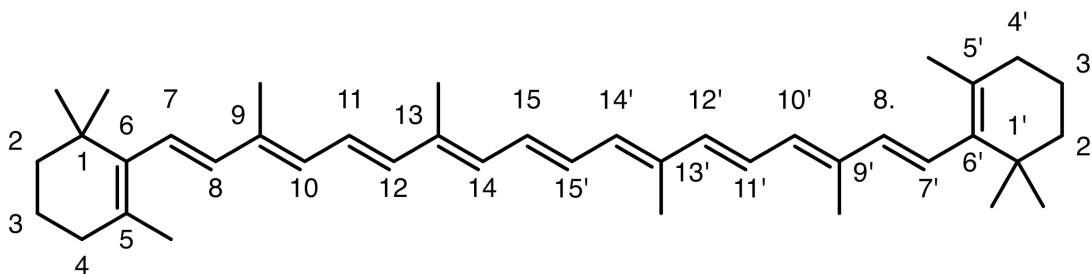
The results of these studies support the idea that torsional distortions along the carotenoid backbone are involved in the photoactivation process of the OCP. The results further suggest that this torsional movement may allow the C terminal end of the carotenoid to move into the cavity between the domains of the protein.

Chapter 1. Introduction

1.1. Photophysics of Carotenoids

Carotenoids perform essential roles in light harvesting and photoprotection in photosynthetic organisms.^{1,2} These functions arise principally from the properties of the two lowest energy excited singlet states, the S_1 and S_2 states.^{1,3-5} The S_2 state is optically populated by $\pi \rightarrow \pi^*$ transitions in the strong, mid-visible absorption band, which gives solutions of the carotenoids a characteristic yellow or orange color. In condensed phases and in the binding sites of proteins, the S_2 state decays usually in < 200 fs after absorption of light. Such short lifetimes, on the order of the mid-frequency vibrations of the isoprenoid backbone (Scheme 1), suggest that passage to the S_1 state is mediated by a nonadiabatic mechanism,^{6,7} involving strong coupling of the nonradiative electronic transitions to vibrational motions. The fluorescence quantum yield is $\sim 10^{-6}$,⁸ much smaller than that of many other $\pi \rightarrow \pi^*$ chromophores. Unusually for the lowest singlet excited states of $\pi \rightarrow \pi^*$ chromophores because it violates Kasha's rule,⁹ fluorescence from the S_1 state of carotenoids is weaker than that from S_2 or not observed^{10,11} despite the S_1 state's having a much longer lifetime, usually in the ~ 10 ps range.³

Scheme 1. Structure of β -carotene



The distinct spectroscopic properties of the S_1 and S_2 states in all-trans polyenes and carotenoids are usually rationalized in terms of the selection rules for optical transitions for planar structures belonging to the C_{2h} point group.¹ The S_0 and S_2 states are assigned the A_g and B_u characters, respectively, so one-photon electric-dipole transitions between them are fully allowed. The S_1 state is assigned the A_g character, however, so absorption and fluorescence transitions between it and the S_0 state are forbidden by the Laporte rule.^{12,13} This scheme is consistent with the finding by Holtom and McClain¹⁴ that the S_1 state of polyenes can be populated from the S_0 state by two-photon optical transitions.^{11,15,16}

Nonradiative decay of the S_2 state to the S_1 state of carotenoids has been mainly attributed to activity in the resonance Raman-active C–C and C=C bond-stretching normal coordinates of the isoprenoid backbone. Displacements along these coordinates results in a partial inversion of the carbon–carbon bond-length alternation (BLA) pattern along the isoprenoid backbone upon optical preparation of the S_2 state and gives rise to a vibronic progression in the ground-state absorption spectrum.^{1,3,11,17} Relaxation from S_2 to S_1 would involve passage through a conical intersection (CI)^{18,19} after a significant displacement from the photoexcited Franck–Condon S_2 structure along the BLA coordinates.^{19–21} Because the C_{2h} symmetry would be maintained if only the BLA coordinates are involved, nonradiative decay from S_2 to S_1 would account for quenching of the fluorescence due to the symmetry selection rules. The S_1 state is readily detected in carotenoids, however, by virtue of its strong excited-state absorption (ESA) transitions in the 500–600 nm region, which populate a range of higher energy singlet excited states S_n with B_u character.^{22,23}

The S_1 state is nevertheless spectroscopically dark when carotenoids assume asymmetric conformations with symmetries lower than C_{2h} . The ground electronic state, S_0 , often favors

nonplanar structures in solution; steric clashing of methyl substituents with the adjacent isoprenoid backbone results in canting out-of-plane of the β -ionone (cyclohexene) rings of β -carotene and related carotenoids and an overall sigmoidal distortion along the length of the intervening isoprenoid backbone.^{24–27} Further, direct one-photon optical preparation of the S_1 state of carotenoids is not observed even when relief from the symmetry selection rules would be expected, such as in structures lacking an inversion center owing to asymmetric substitution,²³ cis stereochemistry,²⁸ or nonlinear configurations.²⁹ Overall, these findings raise the argument that the distinct spectroscopic and dynamical properties of the S_1 and S_2 states in carotenoids arise from the underlying details of their electronic structures³⁰ and from the Franck–Condon overlaps of their potential energy surfaces with the ground state,²⁹ not as much from simple selection rules determined by symmetry or pseudoparity. The electronic character and the energy ordering³¹ of the lowest singlet states of even the shortest polyenes remains controversial because of their considerable theoretical complexity, requiring multireference calculations to approach chemical accuracy in computational studies.^{32–34} The use of multireference calculations to characterize the doubly excited character of the S_1 excited states of carotenoids has been noted in recent work by Mennucci and coworkers.^{35,36} Because the carotenoids are large molecules, their potential energy surfaces and CIs have not yet been determined by accurate quantum chemical calculations.

As a further indication of the complexity of the electronic structures of carotenoids, studies of their photophysical properties persistently include mention of several additional dark electronic states at energies adjacent to the S_2 and S_1 states.^{1,3} Resonance Raman excitation profiles³⁷ and time-resolved spectroscopy with broadband, femtosecond pulses^{38–41} have implicated one of these dark states, S_x , in mediating nonradiative transfer of population from the

S_2 state to the S_1 state. There are two current proposals for the nature of the S_x state.^{3,4} The first assigns the S_x state to a discrete singlet excited state with an energy lying below that of the bright S_2 state.³⁸ In the scheme introduced by Tavan and Schulten,⁴² this state would have a B_u character in the C_{2h} point group.

An alternative recent proposal is that the S_x state is actually a dynamic intermediate moving on the S_2 state surface along out-of-plane vibrational coordinates of the isoprenoid backbone.⁴ This hypothesis accounts for several key aspects of the femtosecond time evolution of the ESA signals from β -carotene observed by Cerullo et al.³⁸ and of the heterodyne transient grating signals from β -carotene and the ketocarotenoid peridinin observed in our laboratory.^{43,44} As sketched in Figure 1.1 in terms of schematic potential energy surfaces, an initial excursion along the BLA coordinates after absorption of a photon would drive the molecule in less than a vibrational period to the vicinity of a low activation energy barrier, which divides the regions of the S_2 potential energy surface for planar and out-of-plane distorted conformations. Crossing the barrier leads to a steep potential energy gradient with respect to torsional and/or pyramidal coordinates of the isoprenoid backbone.^{4,43-45} The presence of the barrier was initially suggested⁴ in analogy to that determined by electronic structure calculations of the potential energy surfaces for the $\pi \rightarrow \pi^*$ excited states of models for retinal protonated Schiff bases (PSBs) and of medium-conjugation length cyanines.⁴⁶ Qualitatively, the barrier height would be expected to increase with longer polyenes because the π^* character per bond would accordingly decrease; for ethene, the potential energy surface is barrierless.⁴⁷

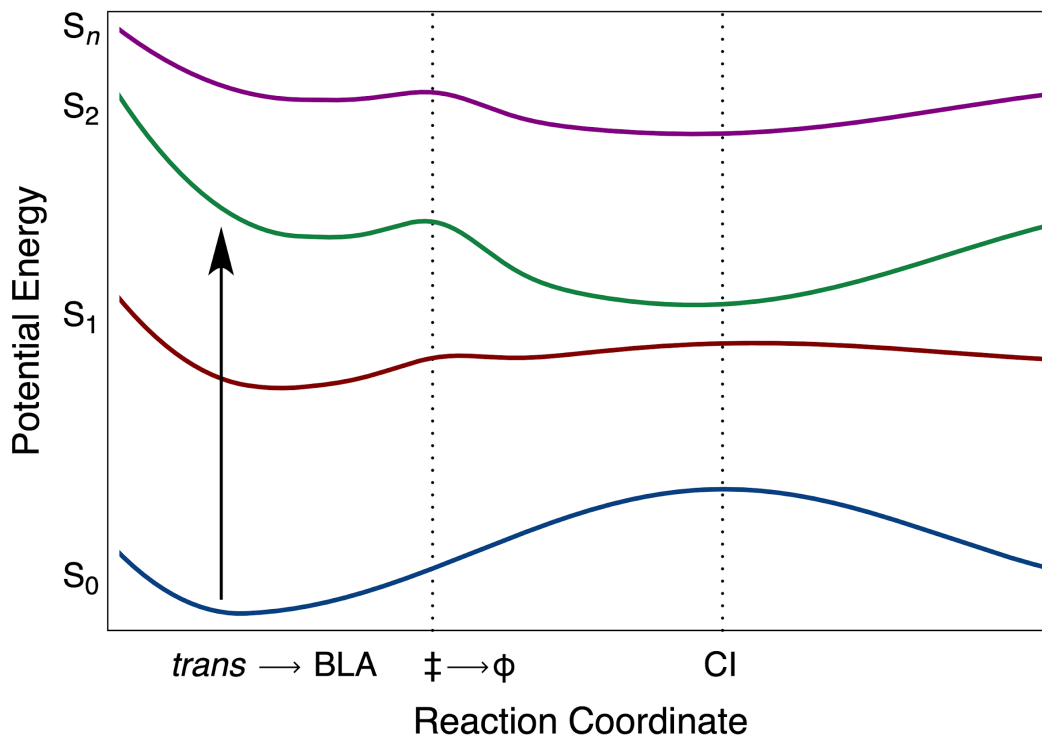


Figure 1.1. Schematic potential energy curves^{4,43,48} proposed for the singlet excited states of all-*trans*- β -carotene, as plotted with respect to a reaction coordinate for the structural response following optical preparation of the S_2 state. An activation-energy barrier (\ddagger) divides planar (BLA coordinates) and out-of-plane distorted (torsional and/or pyramidal coordinates, ϕ) regions of the potential energy surfaces. The S_2 and S_1 surfaces strongly interact at a CI seam near the S_2 minimum with respect to the ϕ coordinates.

Following the barrier, the proposed S_2 and S_1 potential curves are depicted as converging along the out-of-plane coordinates at a seam of CIs,^{19,31} where the two states are expected to be strongly mixed. Rather than the harmonic single-coordinate picture discussed in previous work, then, the photophysics of carotenoids is discussed in this hypothesis in terms of anharmonic multicoordinate dynamics. The shape of the S_1 potential energy curve suggested in Figure 1.1 follows the main features of that proposed by de Weerd et al.⁴⁸ in a discussion of their femtosecond pump–continuum probe results, but we have added a low barrier at the onset of torsions corresponding to that proposed for the S_2 state. Because the S_1 state has a doubly excited character, corresponding to two spin-coupled triplet excitations,³¹ the barrier height would be expected to be lower than that of the S_2 state, which is a singly excited state. The de Weerd et al. results suggest that the S_1 state should exhibit a global minimum near the planar, all-trans structure. Accordingly, crossing from the S_2 state to the S_1 state near the CI seam would usually be followed by conformational relaxation back to the planar structure. This aspect is consistent with the recent suggestion by Wei et al.³⁰ that the S_1 state of carotenoids should be conformationally stiffer (e.g., favoring planar structures) than the S_2 state. In a minor fraction of photoexcitations, of course, this scheme anticipates that relaxation from the CI would occur to the cis configuration on the S_0 surface after internal conversion from the S_1 state. We need to reiterate, however, that these aspects of the S_2 and S_1 potentials are merely hypotheses that are consistent with some, but not necessarily all, of the currently available experimental information.

S_x is detected in heterodyne transient grating spectra as a dynamic intermediate, following the decay of the stimulated emission (SE) from the Franck–Condon S_2 state and prior to the rise of the strong ESA from the S_1 state.⁴³ For peridinin, we found that the lifetime of S_x in a range of solvents exhibits a power law dependence with respect to the viscosity or the polar solvation

time of the solvent. This behavior indicates that radiationless decay from the S_x intermediate on the S_2 surface to the S_1 state is promoted by large-amplitude out-of-plane distortions of the isoprenoid backbone, with the polar solvation dependence implicating formation of an intramolecular charge-transfer (ICT) character.⁴⁵ The changes in electronic structure that accompany twisting and pyramidal distortions of a isoprenoid backbone have been extensively discussed by Bonačić-Koutecký et al.⁴⁹⁻⁵¹ In peridinin, the electron-withdrawing tendency of the carbonyl substituent on the γ -lactone ring in conjugation with the isoprenoid backbone would be expected to enhance the ICT character significantly, which would increase the solvent friction for the motions that promote decay to the S_1 state. This proposal accounts for the observation that the lifetime of the S_x state of peridinin is substantially longer than that of β -carotene, which lacks a carbonyl substituent.⁴⁵

An important implication of the assignment of S_x to a dynamic intermediate in the S_2 state is that the spontaneous fluorescence and SE signals should evolve rapidly to longer wavelengths, well into the near-IR, as molecules descend along the out-of-plane potential energy gradient. The femtosecond pump-probe experiments and global target modeling by de Weerd et al.⁴⁸ suggested this possibility for β -carotene early on. The SE from the S_2 state is red shifted from the ground-state bleaching signal at short time delays following photoexcitation, but at longer time delays it is partially obscured by a much stronger ESA band at longer wavelengths. This time evolution to the red was interpreted in terms of progress along a torsional potential energy gradient, which would narrow the energy gap between the S_2 and S_1 surfaces as they converge at a CI. In recent work, Liebel et al.⁵² used femtosecond transient absorption spectroscopy to observe in β -carotene that passage through the CI between the S_2 and S_1 states occurs with retention of vibrational coherence in modes that lack resonance Raman activity. In Figure 1.1,

the out-of-plane coordinates lack resonance Raman activity because the gradient is accessed only after a significant displacement with respect to the BLA coordinates.

1.2. The Orange Carotenoid Protein

The preceding photophysical picture may help explain the photophysics of the ketocarotenoid bound within the Orange Carotenoid Protein (OCP).^{53–60} The OCP is composed of two domains (Figure 1.2) that play distinct roles in photoprotection and nonphotochemical quenching (NPQ)⁶¹ mechanisms in cyanobacteria.^{62,63} The fold of the N-terminal domain (NTD) is unique to cyanobacteria, whereas the C-terminal domain (CTD) shares structural similarity to other proteins within the widespread nuclear transport factor 2-like (NTF2) superfamily.⁶⁴ The CTD is considered a sensory domain that mediates photoactivation.^{57,65} The NTD binds to the phycobilisome as the effector domain that quenches excitons in the phycobilisome.^{62,66–68}

Considerable progress has been made on the structural mechanism for the photoactivation of the OCP.^{60,69–71} The carotenoid spans both domains in the OCP^O state and is held in a distorted conformation. Upon photoconversion to the OCP^R state, which exhibits a red-shifted absorption spectrum, the carotenoid assumes a more planar conformation, and it slides more than 12 Å into the NTD.⁶⁰ This process accompanies a change in the aggregation state of the protein, from a dimer in OCP^O to a monomer in OCP^R.⁷⁰ Removal of the CTD by proteolysis obtains a NTD-only protein termed the Red Carotenoid Protein (RCP), which is constitutively active as a quencher of excitons in the phycobilisome.⁶⁹

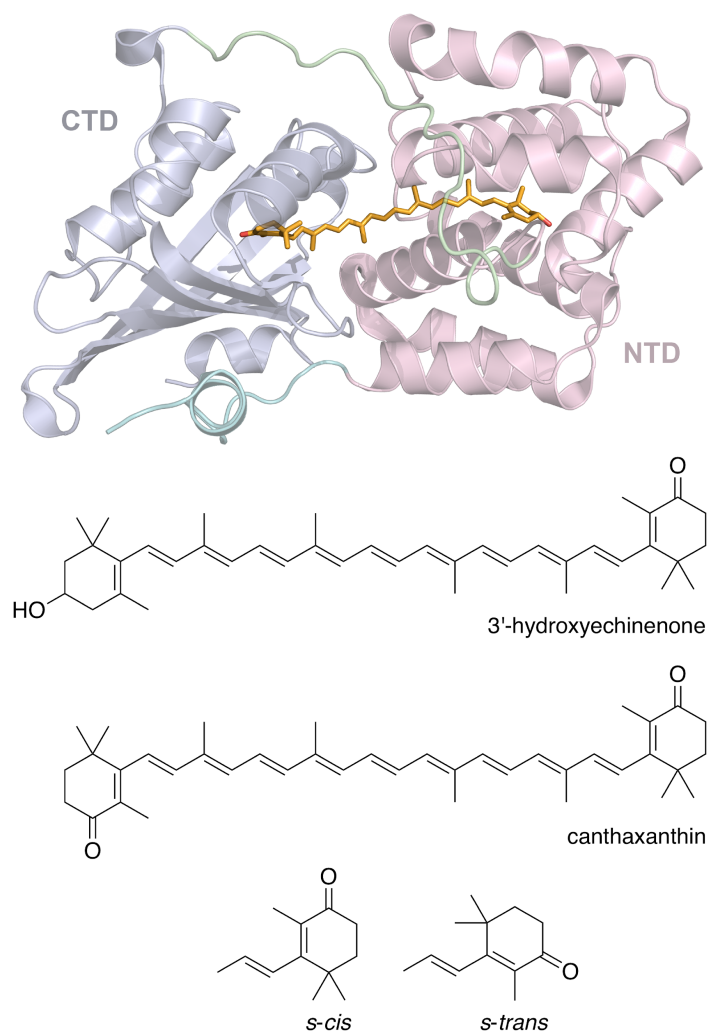


Figure 1.2. Structures of the OCP and of its associated carotenoids. (Top) Structure in the resting, orange state (OCPO) from *Arthrospira maxima* (5UI2.pdb).⁵⁴ The N- and C-terminal domains (NTD and CTD, respectively) are rendered as red and grey ribbons; the peripheral N-terminal α helix and the linker between the NTD and CTD are rendered in green. The bound 3'-hydroxyechinenone (3hECN) is rendered as a stick structure, with carbon atoms in orange and oxygen atoms in red. (Bottom) Structures of the two ketocarotenoids discussed in this study, 3hECN and canthaxanthin (CAN). The *s-cis* and *s-trans* conformations of the β -cyclohexene end rings, as obtained by internal rotation with respect to the conjugated polyene backbone, are shown as fragments.

Photoactivation and the photoprotection function of the OCP apparently depend on the specific photophysical and photochemical properties afforded by carbonyl-substitution of the bound carotenoid. Figure 1.2 includes the structures of the two examples considered in this study: 3'-hydroxyechinenone (3hECN) and canthaxanthin (CAN). Echinenone (ECN) is also functional when incorporated in OCP, but it is notable that zeaxanthin, which presents hydroxyl groups instead of carbonyls on both of its β -cyclohexene rings, can be incorporated in vivo or reconstituted in vitro but yields nonfunctional OCP proteins that cannot be photoactivated.⁷² As in peridinin,^{23,73-76} the carbonyl substituent's electron-withdrawing properties impart an intramolecular charge-transfer (ICT) character to the carotenoid's singlet excited states.⁷⁷⁻⁸¹

Chapter 2. Fluorescence and Excited State Conformational Dynamics of the Orange Carotenoid Protein*

2.1. Summary

The Orange Carotenoid Protein (OCP) mediates nonphotochemical quenching (NPQ) mechanisms in cyanobacteria. A bound ketocarotenoid serves as a sensor of mid-visible light intensity and as a quencher of phycocyanobilin excitons in the phycobilisome. The photochemical mechanism that triggers conversion of the protein from a resting, orange state (OCP^O) to an active, red state (OCP^R) after optical preparation of the S₂ state of the carotenoid remains an open question. We report here that through fluorescence spectroscopy and quantum yield measurement of the bound carotenoids in OCP^O important details of the motions that follow optical preparation of the S₂ state are revealed. The fluorescence spectra from OCP^O preparations containing 3'-hydroxyechinenone (3hECN) or canthaxanthin (CAN) are markedly mirror asymmetric with respect to the absorption line shape and more than an order of magnitude more intense than for carotenoids in solution. Further, 3hECN exhibits a narrower fluorescence line shape and a larger quantum yield than CAN because its excited-state motions are hindered by a hydrogen bonding interaction between the 3'-hydroxyl group on its β₂ ring and Leu37 in the N-terminal domain. These results show that large-amplitude motions of the carotenoid's β₂-cyclohexene ring and of the conjugated polyene backbone initiate photochemistry in OCP^O.

* This chapter is adapted from the following publication:
Gurchiek, J. K.; Bao, H.; Domínguez-Martín, M. A.; McGovern, S. E.; Marquardt, C. E.; Roscioli, J. D.; Ghosh, S.; Kerfeld, C. A.; Beck, W. F. Fluorescence and Excited-State Conformational Dynamics of the Orange Carotenoid Protein. *J. Phys. Chem. B* **2018**, *122* (6), 1792–1800.

2.2. Introduction

In this chapter, we demonstrate that the continuous-wave fluorescence spectrum from OCP⁰ reveals important details about the dynamics that follow optical preparation of the carotenoid's S₂ state and that lead to photoactivation. To our knowledge, this is the first report of fluorescence observations from any carotenoprotein. In comparison to resonance Raman spectroscopy, which provides information on the instantaneous changes in structure that accompany optical excitation of the carotenoids,⁸²⁻⁸⁴ the fluorescence line shape and quantum yield provide information on excited-state changes in structure occurring over the much longer time window associated with radiationless decay and photochemistry.^{85,86} Compared to carotenoids in solution, we find that the quantum yield of fluorescence of the ketocarotenoids in OCP is enhanced and that the fluorescence line shapes are commensurately narrower. These results indicate that the binding site in OCP lengthens the lifetime of the emissive S₂ state by guiding the excited-state motions that eventually lead to the production of OCP^R. The larger fluorescence quantum yield and narrower line shape observed for 3hECN compared to those of CAN indicate that specific interactions with the substituent on the β₂ ring control the large amplitude out-of-plane motions that promote nonradiative decay to the S₁ state.

2.3. Experimental Section

2.3.1. Sample Preparation*

OCP preparations incorporating 3hECN were obtained from *Arthrospira platensis*. Frozen cells were lysed by thawing them in a buffer solution at pH 8.0 (4 °C) containing 100 mM tris(hydroxymethyl)aminomethane (Tris)-HCl, 100 mM NaCl, 5% (v/v) glycerol, 4 mM phenylmethylsulfonylfluoride (PMSF), 4 mM ethylenediaminetetraacetic acid (EDTA), and 2 mM (ethylene glycol-bis(β -aminoethyl ether)-N,N,N,N'-tetraacetic acid (EGTA). The cells were then broken in a bead beater with 0.1 mm glass beads for 3–8 cycles of 15 s. The extract was centrifuged at $10,000 \times g$ and then precipitated with 1.5 M ammonium sulfate. The supernatant was centrifuged at $40,000 \times g$ to pellet the remaining thylakoids and phycobiliproteins. OCP was then isolated using hydrophobic interaction chromatography. Orange fractions containing OCP were reserved and desalted on a 2.5 cm \times 60 cm Superdex G-25 column (GE Health Sciences) using 20 mM Tris-HCl, pH 8.5 and 1 mM EDTA as the elution buffer. An intermediate purification of the desalted OCP was performed using anion exchange chromatography. OCP-containing fractions with A496/A280 > 1.5 were pooled and concentrated using Amicon concentrators. These fractions were desalted using a Mono-Q HR 16/10 ion exchange column (GE Health Sciences). A final size exclusion separation was then performed. The purity of the final OCP fractions was confirmed by absorption spectroscopy and SDS-PAGE.

OCP preparations incorporating CAN were obtained by expressing the gene for OCP from *Synechocystis* sp. PCC 6803 in BL21(DE3) competent *Escherichia coli* cells with a C-terminal 6 \times His tag added and cloned in a pCDFDuet-1 vector (Novagene). BL21(DE3) cells were

* The sample preparation described here was performed by Han Bao in the Kerfeld Laboratory.

OCP preparations incorporating CAN were obtained by expressing the gene for OCP from *Synechocystis* sp. PCC 6803 in BL21(DE3) competent *Escherichia coli* cells with a C-terminal 6×His tag added and cloned in a pCDFDuet-1 vector (Novagene). BL21(DE3) cells were transformed simultaneously with the pCDFDuet-1 vector and the pAC-CANTHipi plasmid (Addgene plasmid #53301)⁸⁷ containing the genes enabling CAN biosynthesis in *E. coli*. The OCP–CAN holoprotein was isolated according to the method described previously⁶⁰ with some modifications. Purification of OCP by Ni-NTA affinity chromatography (HisTrap Affinity column, GE Healthcare) yielded a mixture of apo- and holoproteins. The OCP-CAN holoprotein was further isolated by hydrophobic interaction chromatography (HiTrap HIC phenyl column, GE Healthcare). Concentrations of isolated OCP-CAN holoproteins were determined using the absorption maximum extinction coefficient of CAN ($118,000 \text{ M}^{-1} \text{ cm}^{-1}$) and the known 1:1 binding stoichiometry of CAN:OCP. The purity of the final OCP fractions was confirmed by absorption spectroscopy and SDS-PAGE.

CAN was prepared biosynthetically for fluorescence studies in solution. BL21(DE3) cells containing the pAC-CANTHipi plasmid were grown in LB medium at 37 °C overnight. The culture was harvested at $5000 \times g$ for 10 min, and then CAN was extracted from the pellet with acetone at –20 °C. The acetone was removed subsequently by evaporation under a stream of nitrogen gas.

2.3.2. Spectroscopy

Absorption spectra were recorded at room temperature (23 °C) by a Shimadzu UV-2600 spectrophotometer (2 nm bandpass).

Fluorescence spectra were recorded at room temperature (23 °C) with a home-built fluorescence spectrometer. Excitation light at 500 nm (5 μ W) was obtained from a Jobin-Yvon AH10 quartz halogen lamp and a H10 single monochromator (4 nm bandpass) or a Thorlabs MNWHL4 broadband white LED and a Spectral Products CM112 double monochromator (2 nm bandpass). Emission was detected by an Acton Research SP-150 spectrograph (4 nm bandpass) and a Princeton Instruments Versarray 1300B CCD detector (back-illuminated sensor chip, liquid nitrogen cooled). Calcite Glan-Thompson polarizers were placed in the excitation and emission beams. The emission polarizer was rotated to the magic angle, 54.7°, with respect to the excitation beam's plane of polarization in order to record dichroism-free spectra.⁸⁸ Multiple timed exposures of the CCD detector were accumulated; the dark background was subtracted, and then the cosmic ray spikes were removed by an analysis of the statistics of the individual exposures. For the 3hECN and CAN in OCP⁰, four 2.5 min exposures were accumulated. For CAN in chloroform solvent, six 10 min scans were accumulated.

For the samples used in absorption and fluorescence spectroscopy, the 3hECN and CAN OCP preparations were suspended in a buffer solution containing 50 mM Tris-HCl, pH 8.0, and 200 mM NaCl to obtain an absorbance of 0.2 at 500 nm in a 1 cm cuvette. CAN was dissolved to obtain the same absorbance in chloroform solvent. All of the samples were centrifuged to pellet undissolved particles prior to recording fluorescence spectra. Sample handling of the OCP preparations was conducted in darkness and the fluorescence spectra were acquired with dark-adapted samples; the sample cuvette was held in total darkness in the fluorescence spectrometer for at least two hours prior to exposure to excitation light. The intention here was to obtain dark-stable OCP preparations with predominantly the OCP⁰ state present. The resting ground-state ensemble apparently contains, however, a small fraction of OCP^R that contributes

especially to the red onset of the absorption spectrum.^{83,89-92} The absorption spectrum was measured before and after the fluorescence measurements to determine whether any OCP^R had been photoaccumulated. No changes in the absorption spectra were observed over the total exposures at the low excitation light intensities used in these experiments.

2.3.3. Structural Analysis

Structures of OCP were obtained from the Protein Data Bank (<https://www.rcsb.org>).⁹³ They were visualized and arranged as shown in the figures using PyMOL (<https://pymol.org>).⁹⁴ Routines provided with PyMOL were used to measure distances and dihedral angles.

2.4. Results

2.4.1. Absorption and Fluorescence Lineshapes

Figure 2.1(a,b) compares the ground-state absorption and fluorescence spectra from OCP^O preparations at room temperature with 3hECN or CAN incorporated. The spectra are plotted as relative dipole (or oscillator) strengths, $\epsilon(\nu)/\nu$ and $\lambda^2 F(\nu)/\nu^3$, respectively, to allow proper comparison of their line shapes. Here $\epsilon(\nu)$ and $F(\nu)$ are the absorbance and the fluorescence intensity at a given wavenumber ν ; λ is the emission wavelength. The λ^2 factor compensates for the fixed emission bandpass in wavelength units.⁸⁸

3hECN and CAN exhibit comparable absorption spectra in OCP^O with partially resolved vibronic structure. The absorption spectrum arises from strong transitions from the ground state, S_0 , to the second excited singlet state, S_2 . The S_0 and S_2 states correspond to the $1^1A_g^-$ and $1^1B_u^+$ states in planar carotenoids with C_{2h} symmetry, but in OCP the carotenoids are held in distorted ground-state conformations with low symmetry.^{54,60} In contrast, the oscillator strength for

transitions from the S_0 state to the S_1 state ($2^1A_g^-$ for planar structures) of carotenoids is extremely weak.^{29,95} As is commonly observed in carotenoids of comparable conjugation length, the main contributions to the vibronic structure are involve the totally symmetric, resonance Raman-active C–C and C=C vibrational coordinates of the conjugated polyene backbone.⁸³ Strong displacements occur along these coordinates from the Franck–Condon excited-state structure immediately upon optical preparation of the S_2 state.

Despite having similar absorption spectra, 3hECN and CAN exhibit distinct fluorescence line shapes when bound by OCP⁰. Both fluorescence spectra lack resolved vibronic structure, and they are markedly mirror asymmetric with respect to the absorption spectrum's line shape. The mirror asymmetry indicates that large-amplitude excited-state distortions of the carotenoid's β -cyclohexene end rings and conjugated polyene backbone occur prior to or during the emission of fluorescence. The vibrational modes that are involved lack strong resonance Raman activity, so the resulting Franck–Condon factors that control the vibronic structure of the fluorescence are much different than for the absorption transitions. The fluorescence spectrum from 3hECN displays an asymmetric Gaussian or lognormal⁹⁶ lineshape, indicating unresolved vibronic structure owing to displacements along mainly low-frequency modes, whereas the much broader spectrum from CAN is essentially a Lorentzian, implying uncertainty broadening due to a very short emissive lifetime. It is also interesting that the spectrum from 3hECN has a larger Stokes shift, the shift in wavenumbers from the absorption maximum to the fluorescence maximum, than that from CAN, respectively. These observations indicate that the fluorescence emission occurs over a very short time as the carotenoid's structure evolves on the S_2 potential surface.

Most importantly, in addition to having a much different lineshape, the fluorescence spectrum from 3hECN in OCP⁰ is almost ten times more intense than that observed with the

CAN-containing OCP⁰ preparations under the same measurement conditions. The relative yields can be judged qualitatively in Figure 2.1 by comparing the relative intensities of the fluorescence and the nonresonance Raman band from water at a 3500 cm⁻¹ shift, which provides an internal intensity reference. Further, by comparing the integrated area of the fluorescence spectrum with that of rhodamine 6G in methanol⁹⁷ under the same illumination and detection conditions, we estimate that the quantum yields of fluorescence for 3hECN and CAN are 3.8×10^{-3} and 6.0×10^{-4} , respectively.

In comparison, Figure 2.1(c) shows that the fluorescence spectrum for CAN dissolved in chloroform solvent exhibits a much broader Lorentzian line shape and is fifteen times weaker than in OCP⁰; the quantum yield is 4×10^{-5} , again as determined relative to rhodamine 6G in methanol. This quantum yield is in the range reported for the fluorescence of carotenoids with and without carbonyl substitution; an identical quantum yield and a similar spectrum was obtained previously for CAN in chloroform.⁹⁸ This comparison indicates a major impact of the binding site of OCP⁰ on the excited-state dynamics of the bound carotenoid. The quantum yield is larger for the carotenoids in OCP⁰ than in solution because the emissive lifetime of the S₂ state is significantly lengthened in the protein environment.

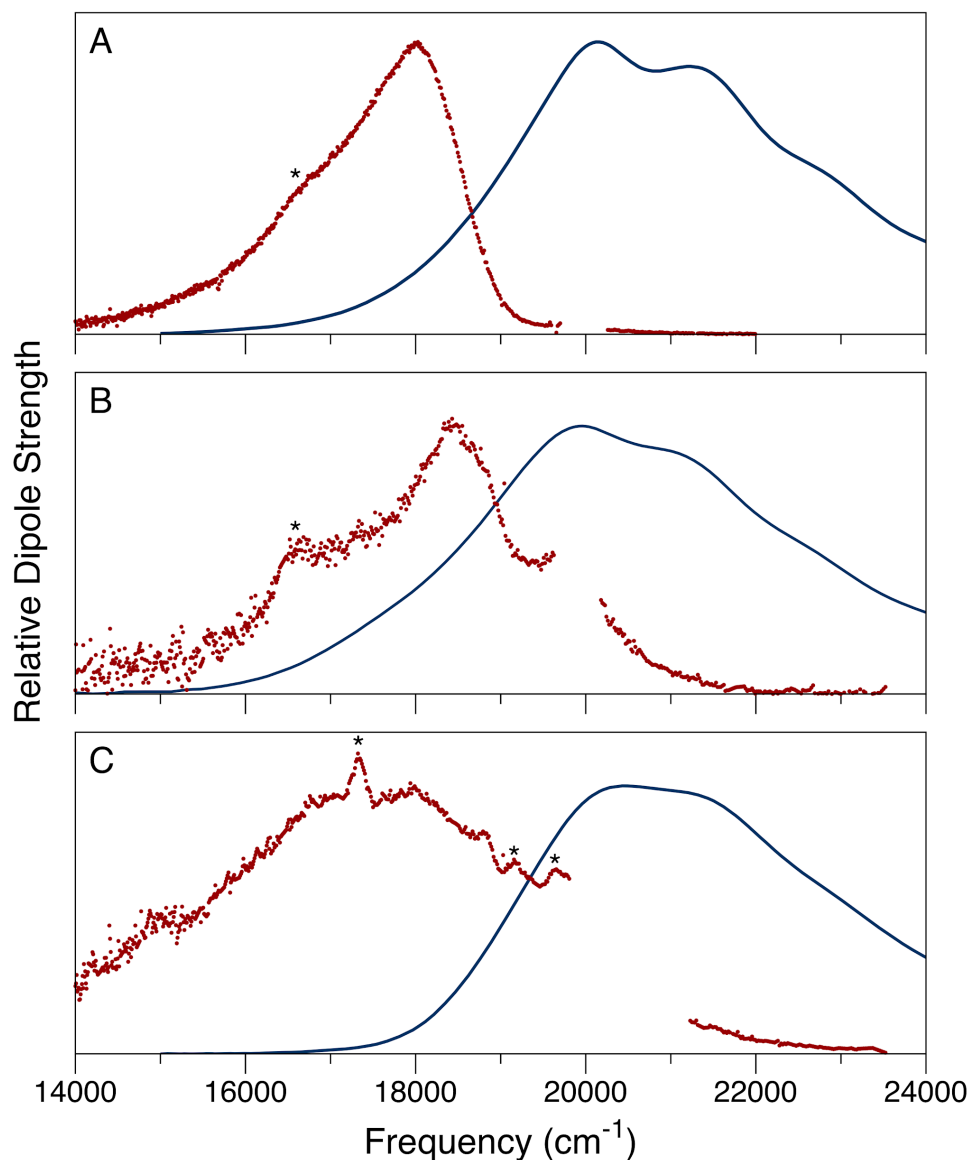


Figure 2.1. Room-temperature (23 °C) absorption (blue) and fluorescence (red) spectra of carotenoids in OCP⁰: (a) 3hECN; (b) CAN; and (c) CAN in chloroform solvent. The intensities are plotted as dipole strengths, $\epsilon(\nu)/\nu$ and $\lambda^2 F(\nu)/\nu^3$, respectively, with normalization to peak intensity. The excitation monochromator for the fluorescence was tuned to 500 nm (20000 cm^{-1}) for panels (a) and (b) and to 490 nm (20408 cm^{-1}) for (c). In panels (a) and (b), the asterisk at 16500 cm^{-1} marks the wavenumber of the nonresonant Raman band from water (shift of 3500 cm^{-1}). In panel (c), asterisks nonresonant Raman bands from the chloroform solvent at 17340, 19160, and 19640 cm^{-1} (shifts of 3034, 1220, and 774 cm^{-1}).⁹⁹

2.4.2. System–Bath Coupling

Additional insight into the structural origin of the excited-state structural dynamics that control the fluorescence yield and line shape for carotenoids in OCP⁰ can be obtained from numerical simulations using the multimode Brownian oscillator (MBO) model.^{100–104} The MBO model describes the time-dependent broadening of the absorption and fluorescence spectroscopic line shapes resulting from the coupling of the transition dipole moment of a chromophore with its vibrational modes and with the motions of its surroundings. A summary of the relevant theory (Equations S1–S4) and a brief discussion is provided in the Supporting Information. Simulations of the ground-state absorption spectrum for 3hECN (Figure 2S.1) and CAN (Figure 2S.4) in OCP⁰ and for CAN in chloroform (Figure 2S.7) provide estimates in each system for the total strength of the system–bath coupling or solvation reorganization energy, λ in the ground state.¹⁰⁰ In the following, the system–bath coupling is correlated with the fluorescence quantum yield and line width to infer whether the excited-state dynamics are determined just by the number of carbonyl substituents or whether one should expect to find stronger, specific interactions between the carotenoids and groups in the binding site of OCP⁰.

The MBO model has been applied in previous work to describe the absorption spectrum and third-order nonlinear optical response of carotenoids in solution and in light-harvesting proteins.^{43–45,105,106} This work has shown for carotenoids how the vibronic structure displayed in the absorption spectrum reveals the strength of the system–bath coupling. In general, as λ increases, the breadth of the vibronic transitions increases and the resolved vibronic structure accordingly decreases in modulation amplitude. Of especial interest here is the expectation that a stronger coupling to the surroundings results from carbonyl substitution owing to the addition of electron-withdrawing character to the conjugated polyene backbone and a resulting ICT

character. As previously discussed for peridinin in polar solution,⁴⁵ λ is related to the friction for the excited-state motions that promote nonradiative decay.^{107,108}

Along with a listing of the other parameters that characterize the absorption and fluorescence spectra from the two carotenoids in OCP⁰ and for CAN in chloroform solution, Table 2.1 compares the reorganization energies from an MBO simulation of the absorption spectrum, here denoted by λ_{abs} , with the reorganization energy determined from the fluorescence Stokes shift, λ_{fluor} . The fluorescence Stokes shift is usually equated with 2λ . We use here a spectral moment-based approach (equation 2S.5)¹⁰⁹ that avoids the assumption of Gaussian line shapes.

In line with previous work on carotenoids, because the vibronic structure is less well resolved for CAN (Figures 2.1(b) and 2S.4–2S.6) than for 3hECN in OCP⁰ (Figures 2.1(a) and 2S.1–2S.3), the best simulations of the resolved vibronic structure return a significantly larger value of λ_{abs} for CAN. This finding is consistent with the carbonyl substitution of CAN, on both of its β -cyclohexene rings, compared to the single carbonyl substitution of 3hECN. Further, the λ_{abs} obtained for CAN in chloroform solution is even larger than in OCP⁰. But this increasing trend in λ_{abs} is directly anticorrelated with the fluorescence quantum yield; the largest quantum yield is observed for 3hECN in OCP and the smallest for CAN in chloroform. This finding strongly suggests that radiationless decay of the carotenoid in OCP⁰ is controlled by a specific structural interactions of the β_2 ring's substituent with the OCP⁰ binding site in the NTD.

Table 2.1. Absorption and fluorescence spectral parameters for 3hECN and CAN in OCP⁰ preparations and for CAN in chloroform solvent

Parameter	3hECN	CAN	CAN in CHCl ₃
organism	<i>A. platensis</i>	<i>Synechocystis</i> 6803	—
ω_{0-0}^a	19160 cm ⁻¹	18672 cm ⁻¹	18850 cm ⁻¹
λ_{abs}^b	2205 cm ⁻¹	2425 cm ⁻¹	2570 cm ⁻¹
λ_{fluor}^c	1993 cm ⁻¹	1416 cm ⁻¹	2011 cm ⁻¹
$\Delta\omega_F^d$	1930 cm ⁻¹	1702 cm ⁻¹	4210 cm ⁻¹
Φ_F^e	3.8×10^{-3}	6.0×10^{-4}	4×10^{-5}

^aEnergy gap for S₀ to S₂, from MBO simulation of the absorption spectrum (Figures 2S.1, 2S.4, and 2S.7)

^btotal reorganization energy, from MBO simulation of the absorption spectrum (Figures 2S.1, 2S.4, and 2S.7);

^cobserved reorganization energy, using moment analysis of the absorption and fluorescence line shapes¹⁰⁹

^dfluorescence line width (fwhm);

^efluorescence quantum yield

2.5. Discussion

The fluorescence line shapes, quantum yields, and system–bath couplings observed for 3hECN and CAN in OCP^o reveal important aspects of the excited state dynamics that follow optical preparation of the carotenoid's S₂ state. The lognormal fluorescence lineshape exhibited by 3hECN indicates that several vibrations along low frequency modes occur during the emissive lifetime. In contrast, the broad Lorentzian lineshape and much lower quantum yield for the fluorescence from CAN reports a very short effective emissive lifetime, <20 fs; an even much broader spectrum is observed for CAN in chloroform. These fluorescence properties are anticorrelated with the system–bath coupling determined from simulations of the absorption spectrum. This finding indicates that one should expect to find specific structural interactions in the binding sites for the carotenoids in OCP^o that control the motions that mediate nonradiative decay of the S₂ state in competition with fluorescence emission.

As shown in the following, the two OCP orthologs used in this study have essentially identical carotenoid-binding sites. Because the only difference between the two carotenoids is the replacement of a carbonyl (CAN) with a hydroxyl (3hECN), the excited-state motions that promote nonradiative decay are very likely to include large-amplitude twisting or bending motions of the β₂ β-cyclohexene end rings of the carotenoids in OCP and of the intervening conjugated polyene backbone. The likely structural origin for the larger fluorescence quantum yield for 3hECN compared to CAN in OCP^o is the presence of a hydrogen bonding interaction between the NTD part of the binding site and the β₂ ring.

Figure 2.2 compares the binding of 3hECN and CAN in two orthologs of OCP^o, from structures 5IU2 and 4XB5, respectively. The structure used in the figure for the 3hECN-binding ortholog is from *A. maxima* rather than from *A. platensis*, the source of the preparations used in

the fluorescence experiments; a crystal structure from the latter organism is not currently available. Figure 2S.9 shows, however, that the amino acid sequences in the binding site region are almost completely conserved for the two organisms.

As shown in Figures 2.2(a) and 2.2(b), the carbonyl substituents on the $\beta 1$ rings of 3hECN and CAN accept analogous hydrogen bonding interactions with tyrosine and tryptophan residues in the CTD. These hydrogen bonds have been discussed previously.^{54,110} Owing to its hydroxyl substituent, however, an additional hydrogen bond restricts the motion of the $\beta 2$ ring of 3hECN in the NTD. Figure 2.2(c) shows that the hydroxyl group on the $\beta 2$ ring of 3hECN in the 5UI2 structure is oriented so that it can serve as a hydrogen bond donor to the peptide carbonyl on Leu37. The measured distance between the hydroxyl oxygen and the carbonyl oxygen, 2.7 Å, corresponds to a hydrogen bond length of 2.0–2.1 Å between the hydroxyl proton and the acceptor carbonyl oxygen. In the 5TV0 structure,¹¹¹ which explicitly includes coordinates for the protons, the distance between the hydroxyl proton and the carbonyl oxygen from Leu37 is 2.1 Å and the hydrogen bond angle is 152° (Figure 2S.10 and Table 2S.8). Note that Leu37 also makes a hydrogen bond along the α helix with the amide proton of Trp41. This competing hydrogen bond would be expected to weaken the interaction of Leu37 with 3hECN.

Figure 2.2(d) shows that the formation of an analogous hydrogen bond by the $\beta 2$ ring of CAN is impossible because it lacks a hydroxyl group. Instead, the carbonyl on CAN clashes with that of Leu37, causing the two carbonyls to be tilted and displaced away from each other to an oxygen to oxygen distance of 4.4 Å. The $\beta 2$ ring for CAN is accordingly freer to make torsional or other out-of-plane motions that modulate the ring's coupling to the conjugated polyene backbone. As explained below, motions of this type mediate nonradiative decay of the S_2 state to the S_1 state because the potential surfaces converge at a conical intersection.

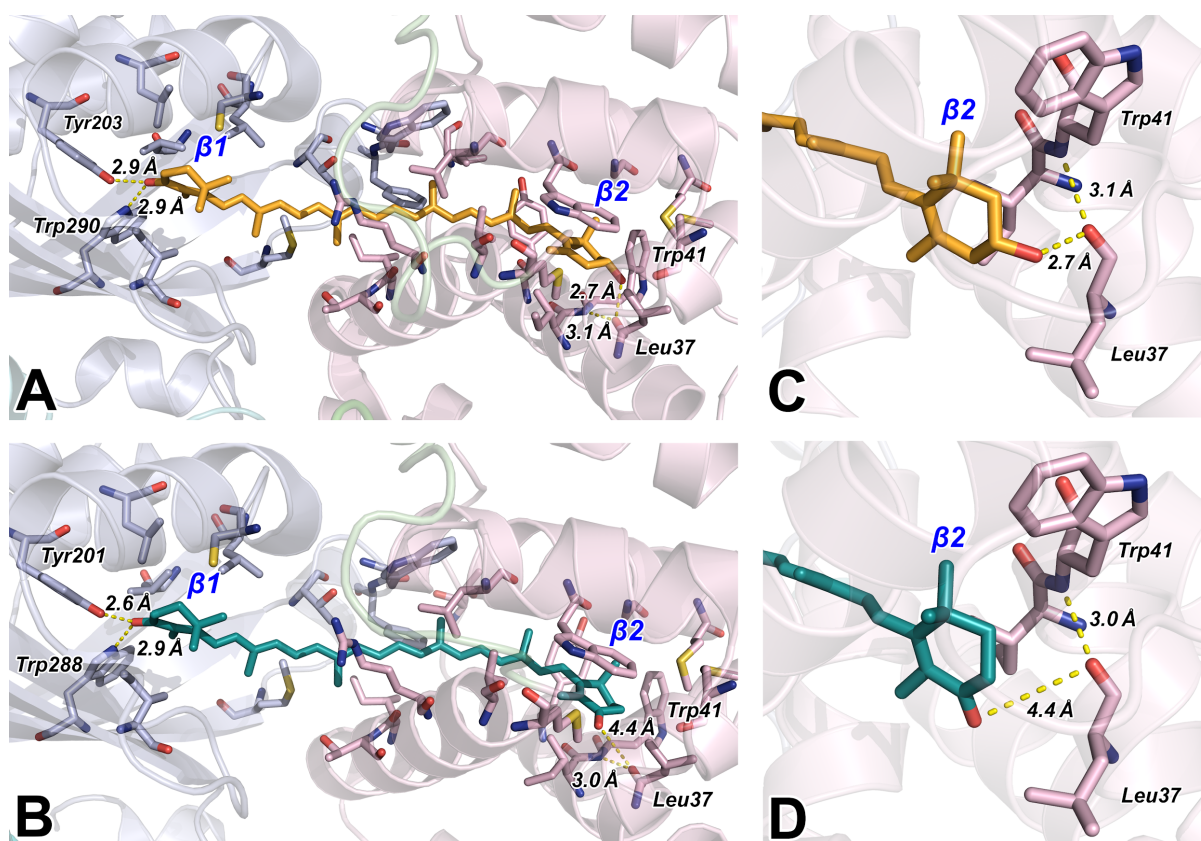


Figure 2.2. Protein–ketocarotenoid hydrogen bonding interactions by the $\beta 1$ (CTD) and $\beta 2$ (NTD) β -cyclohexene rings of the carotenoids bound in OCP^O: (a) for 3hECN, from structure 5UI2.pdb from *A. maxima*;⁵⁴ (b) for CAN, from structure 4XB5.pdb from *Synechocystis* sp. PCC 6803;⁶⁰ (c) detail from a rotated vantage point of the $\beta 2$ ring's hydrogen bonding interaction between the hydroxyl group and the carbonyl on Leu37 and (d) for the clash between the $\beta 2$ carbonyl on CAN and that on Leu37. Protons are not displayed in these diagrams. Figure 2S.9 shows the same views for 3hECN in the 5TV0.pdb structure from *Synechocystis* sp. PCC 6803,¹¹¹ which presents explicit protons. Table 2S.8 compares the distances from interacting protein groups for the $\beta 1$ and $\beta 2$ rings in the three structures.

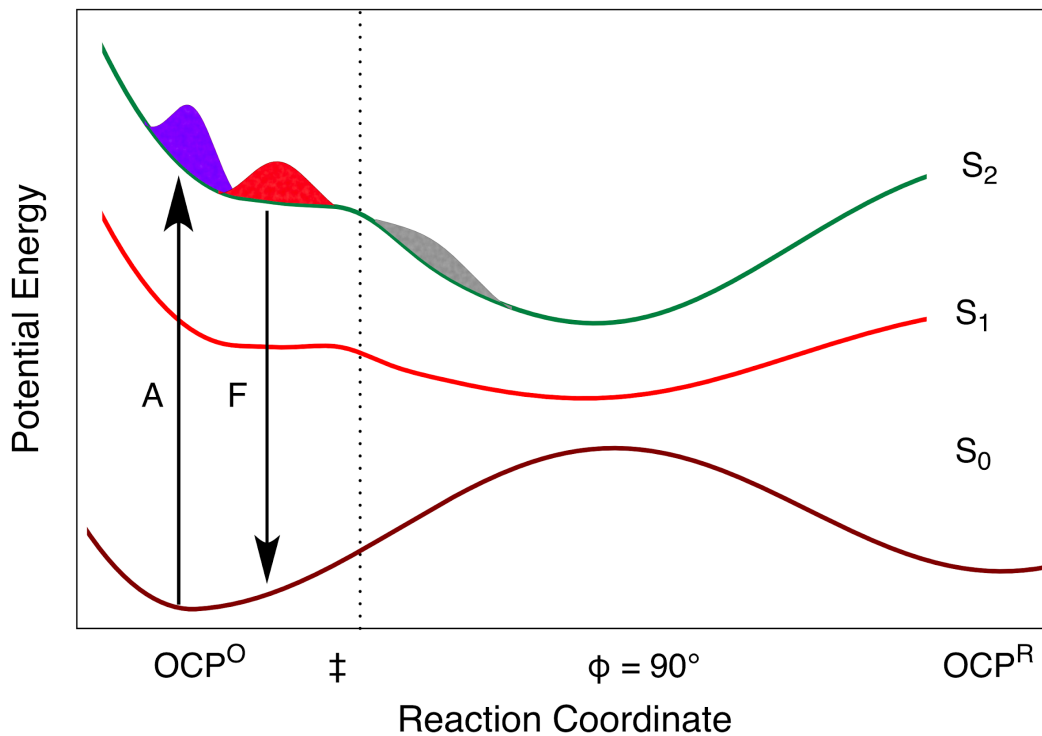


Figure 2.3. Potential energy surfaces proposed for carotenoid chromophores in the OCP. The energies of the S_0 , S_1 , and S_2 states are plotted as a function of a reaction coordinate composed of motions of the conjugated polyene and β -cyclohexene end rings, first along C–C/C=C stretching coordinates and then by torsional or pyramidal out-of-plane distortions. Absorption (A) and fluorescence (F) transitions are marked. Progress along the reaction coordinate from the Franck–Condon structure of the carotenoid in OCP⁰ is depicted in terms of a series of Gaussian wavepackets, which broaden as displacement along the reaction coordinate increases due to the friction with the surrounding protein.

Figure 2.3 presents a potential-energy scheme that accounts qualitatively for the impact of excited-state distortions of the conjugated polyene backbone of the carotenoids in OCP⁰ on the yield and spectrum of the fluorescence emission. The diagram is derived from that discussed previously for β -carotene and peridinin.^{4,43–45,112} The potential energies of the S₀, S₁, and S₂ states are depicted in this diagram as functions of a generalized reaction coordinate that describes what happens structurally to the carotenoid after optical preparation of the S₂ state. Similar potential-surface diagrams have been discussed for protonated Schiff bases and cyanines of intermediate to long conjugation lengths.^{46,113}

Instantaneously upon optical preparation of the S₂ state, strong forces act along the resonance Raman-active C-C and C=C stretching coordinates of the carotenoid in OCP⁰. The conjugated polyene backbone is lengthened abruptly, launching the motion of a wavepacket on the S₂ potential surface towards a low transition-state barrier that divides predominantly planar conformations of the conjugated polyene backbone from those that are distorted along out-of-plane coordinates. Upon reaching the barrier and most likely without recurrence to the Franck–Condon structure, the carotenoid begins twisting and bending motions that sharply lower the energy of the S₂ state; the S₂, S₁, and S₀ potential energy surfaces converge at a conical intersection.^{4,20} The twisting distortions advance the wavepacket diffusively along the reaction coordinate and promote nonradiative transitions from S₂ to S₁. The wavepacket is increasingly likely to jump from S₂ to S₁ as it approaches the conical intersection, but relaxation through a seam¹¹⁴ to the S₁ state probably occurs well prior to the formal intersection at a 90° twist. Subsequent vibrational cooling on the S₁ state surface would be expected to partition the excited-state population into the two possible ground-state products: the original OCP⁰ conformation, or with a much lower yield of the conformation that triggers the protein response

to generate the photoactivated OCPR product. The vertical energy gap from the OCPR minimum to the S_2 state is smaller than that for OCP^0 , consistent with a red-shifted absorption spectrum. This scheme should be compared with the viewpoint of previous work, where the red-shifted absorption spectrum from OCP^0 is attributed to a lengthening of the effective conjugation length due to changes in the conformations of the β -cyclohexene end rings.^{70,83} The scheme proposed here includes additionally distortion of the intervening conjugated polyene backbone.

As detected previously in studies of peridinin in a range of polar solvents,⁴⁵ the out-of-plane motions of the conjugated polyene backbone that promote nonradiative decay from the S_2 state of a carotenoid would be expected to be frictionally damped by the surrounding medium, so the lifetime of the distorted S_2 state is lengthened by increasing the solvent viscosity. The ketocarotenoids should experience an even larger frictional coupling to the surroundings because the twisting motions promote ICT and assumption of a pyramidal conformation¹¹⁵ due to the electron-withdrawing properties of the carbonyl substituents. In peridinin, the lifetime of the distorted S_2 state correlates best with the polar solvation time because part of the solvent friction arises from the reorganizational motions of the solvent in response to the separation of charge along the conjugated polyene backbone.⁴⁵ The impact of ICT from the carbonyls is less significant in 3hECN and CAN because the carbonyls are located on the β -cyclohexene rings, which are significantly canted out of the plane of conjugation in the ground state (Figures 2S.11 and 2S.12).

The scheme shown in Figure 2.3 readily accounts for the fluorescence properties of OCP^0 and the differences observed for the two incorporated carotenoids. The MBO simulations show directly that the fluorescence emission from the two carotenoids in OCP^0 and from CAN in solution is unconventional. The lack of mirror symmetry for the absorption and fluorescence

spectra is inconsistent with emission principally from a thermally equilibrated excited-state structure after an initial displacement along the resonance Raman-active vibrational coordinates. Instead, the fluorescence is clearly dynamic in character, reflecting the fast motions made by the carotenoid continuously along the reaction coordinate discussed above. Because the oscillator strength of the S_2 state drops rapidly as displacement along the out-of-plane coordinates increases, due to the diminishing Franck–Condon overlap with the photoselected ground-state structure and also to mixing with the dark S_1 state,²⁹ the fluorescence emission from the S_2 state would be expected to be strongest during the wavepacket's progress near to the activation-energy barrier. In this picture, the fluorescence line shape and yield accordingly report how strongly the environment frictionally retards the motions of the carotenoid.

The specific, hydrogen-bonding interaction between the β_2 ring of 3hECN plays a dominant role in controlling the dynamics, mostly likely owing to its raising of the barrier that leads to the torsional gradient on the S_2 potential surface. Even in the absence of this interaction, it is clear that the binding site for the carotenoids in OCP^o imparts significantly more friction for the out-of-plane distortions that quench the fluorescence from the S_2 state than a molecular solvent, resulting in narrower line shapes and larger quantum yields.

2.6. Conclusions

The finding that the intrinsic carotenoids bound by OCP⁰ exhibit observable fluorescence spectra opens the door to a range of new investigations of protein–carotenoid interactions in OCP and possibly in other systems. The fluorescence yield and lineshape can now be used as a sensitive probe of the interactions in OCP with polar or polarizable groups that alter the electronic structure of the carotenoid and of the dynamics that lead to photoactivation. The results presented here establish that OCP⁰ exerts considerable constraint over the excited-state motions of its bound carotenoid. The finding that the fluorescence spectra and yields from 3hECN and CAN in OCP⁰ are controlled by friction and are modulated by specific interactions of the β 2 rings with Leu37 in the NTD is significant because it implicates the out-of-plane motions of the β 2 rings and of the intervening conjugated polyene backbone in the excited-state motions that initiate photoactivation of OCP. These motions are followed by nonradiative formation of nonequilibrium ground-state carotenoid structures with distorted conformations. The results also suggest that nonradiative decay dynamics in carotenoids are promoted in general by excited state motions. The role of the ICT character in ketocarotenoids in the fast motions that distort the optically prepared S₂ state can now be readily studied in a range of solvents using the line shape and quantum yield of fluorescence.

2.S. Supporting Information

2.S.1. Multimode Brownian oscillator (MBO) model

2.S.1.1. Introduction

Additional information on excited-state dynamics can be obtained from numerical simulations of the absorption and fluorescence lineshapes for the carotenoids in OCP using the multimode Brownian oscillator (MBO) model.¹⁰⁰ MBO simulations of the absorption spectra of the two ketocarotenoids in OCP, 3'hydroxyechinenone (3hECN) and canthaxanthin (CAN), are used here to estimate the strength of the system–bath coupling, λ , in the ground state. These values are correlated with the fluorescence quantum yield and line width to determine whether the excited-state dynamics are determined just by the number of carbonyl substituents or whether there are specific interactions between the carotenoids and groups in the binding site of OCP⁰.

2.S.1.2. Theory

The MBO model describes the broadening of the spectroscopic line shapes for a chromophore resulting from the coupling of its optical transition dipole moment with its intramolecular vibrations and with the motions of its surroundings. By hypothesis, each mode of motion is described by a damped harmonic oscillator. A time-correlation function, $M(t)$, determines how the ground-to-excited-state energy gap of the chromophore fluctuates with respect to time due to these motions. As in previous carotenoid simulations,^{43–45,105,106} $M(t)$ was composed with respect to time as the sum of the following Brownian modes: a Gaussian (G) for inertial solvation, the sum of two exponentials ($E,1$ and $E,2$) for diffusive solvation, and two cosinusoids for underdamped intramolecular vibrational modes ($\nu,1$ and $\nu,2$).^{101–104}

$$\begin{aligned}
M(t) = & \lambda_G \exp\left(-\frac{t}{\tau_G}\right) + \sum_i \lambda_{E,i} \exp\left(-\frac{t}{\tau_{E,i}}\right) \\
& + \sum_i \lambda_{v,i} \exp\left(-\gamma_{v,i}t\right) \left(\cos(\Omega_{v,i}t) \left(\frac{\gamma_{v,i}}{2\Omega_{v,i}} \right) \sin(\Omega_{v,i}t) \right)
\end{aligned} \tag{2S.1}$$

For each of the underdamped vibrational modes, the natural frequency of the corresponding harmonic oscillator is ω_v and the damping time is $1/\tau_v$; the resulting mode frequency is $\Omega_v = (\omega_v^2 - (\gamma_v/2)^2)^{1/2}$. The key parameters that control the spectroscopic line shapes are those for the reorganization energies, λ_i , which relate the change in the energy gap due to the displacement of the ground and excited state structures along a particular mode's coordinates.

As discussed by Mukamel,¹⁰² by using the Condon approximation and a second-order cumulant expansion, an internally consistent calculation of all of the linear and nonlinear optical responses of a system is obtained from $M(t)$ by calculating a line-broadening function, $g(t)$.^{101–104}

$$g(t) = i\lambda \int_0^t dt_1 M(t_1) + \Delta^2 \int_0^t dt_1 \int_0^{t_1} dt_2 M(t_2) \tag{2S.2}$$

In equation 2S.2, the term $\Delta^2 = \sum_i 2\lambda_i k_B T / \hbar$ represents the square of the total coupling strength, the modulation of the energy gap by the Brownian modes, and here λ the sum of all the reorganization energies. The ground-state absorption and fluorescence spectra are then expressed in terms of $g(t)$ as $\sigma_A(\omega)$ and $\sigma_F(\omega)$, respectively,^{102,104}

$$\sigma_A(\omega) \propto \omega \operatorname{Re} \int_0^\infty dt \exp\left(i(\omega - \omega_{eg})t - g(t)\right) \tag{2S.3}$$

$$\sigma_F(\omega) \propto \omega^3 \operatorname{Re} \int_0^\infty dt \exp \left(i(\omega - \omega_{eg} + 2\lambda)t - g^*(t) \right) \quad (2S.4)$$

where $\omega_{eg} = \omega_{00} + \lambda$ is the vertical transition frequency, the energy gap between the ground (*g*) and excited (*e*) potential surfaces at the equilibrium ground-state structure, ω_{00} is the energy gap for the 0–0 vibronic transition, and $g^*(t)$ is the complex conjugate of the line-broadening function. When applied to a carotenoid, the states *g* and *e* correspond to the ground state S_0 and the S_2 excited state, respectively.

As is required by hypothesis for the displaced harmonic potentials used in the MBO picture, the calculated absorption and fluorescence spectra are mirror symmetric with respect to ω_{00} . If Gaussian line shapes are observed, the fluorescence Stokes shift, the shift in energy from the absorption maximum to the fluorescence maximum, is equal to 2λ . A better estimate for λ is obtained using the spectral-moment theory introduced by Jordanides et al. (Fleming group)¹⁰⁹ by integrating over the absorption and fluorescence line shapes,

$$\lambda = \hbar \frac{\int_0^\infty d\tilde{\omega} [\sigma_a(\tilde{\omega}) - \sigma_f(\tilde{\omega})] \tilde{\omega}}{\int_0^\infty d\tilde{\omega} [\sigma_a(\tilde{\omega}) + \sigma_f(\tilde{\omega})]} \quad (2S.5)$$

In equation 2S.5, $\tilde{\omega} = \omega - \omega_{eg}$. This equation was used to obtain the estimates for λ_{fluor} listed in Table 2.1.

2.S.1.3. Approach

Starting parameters for the simulations of the absorption spectra from the ketocarotenoids in OCP were taken from the simulations performed previously for β -carotene and peridinin in solution.^{43-45,105,106} For the underdamped vibrational modes (subscripts v , i in equation 2S.1), the models include only the principal C–C and C=C stretching modes, which can be obtained independently from resonance Raman spectra. The parameters were then varied to optimize the fitting of the absorption spectrum's position on the wavenumber axis, the vibronic structure, and, as much as possible as explained below, the width of the spectrum. The main parameters that were varied from the starting set were the vertical transition frequency, the vibrational mode frequencies, and the reorganization energies. It should be kept in mind that the damping times were not varied significantly and are poorly established here and in the previous work based just on simulations of the continuous-wave linear spectra.

2.S.1.4. Results

The best models obtained for 3hECN and CAN in OCP⁰ are shown in Figures 2S.1 and 2S.4, respectively. Figure 2S.7 shows the best model obtained for CAN in chloroform solution. These models provide the values of λ_{abs} tabulated in Table 2.1. The total reorganization energies are similar to that determined previously for peridinin.^{44,45} Additional models are shown for 3hECN and CAN in OCP to explore how increasing the reorganization energy results in loss of resolution of the vibronic structure. Note that the deviation of the simulated and experimental spectra in the blue part of the spectrum, at wavenumbers past the peak maximum, is comparable to that obtained in previous carotenoid modeling,^{43-45,105,106} a better simulation of this region of

the spectrum would likely be obtained by inclusion in the model of a more complete set of resonance Raman-active vibrations, especially for low frequency modes.¹⁰⁴

In all of the simulations, the very broad low wavenumber onset of the experimental absorption spectra over the 14000–18000 cm^{-1} region is not well described. This is consistent with the previous conclusion that the ground state in OCP^{O} contains a significant fraction of a thermally populated, distorted conformation for the bound carotenoids with a smaller ground-to-excited energy gap, which may arise from a dark stable population of the photoactivated form of OCP, OCP^{R} .^{83,89–92} As noted in the Experimental section, however, the absorption spectra shown for OCP^{O} were obtained after extensive dark adaptation and are not significantly changed by the weak illumination used in the fluorescence experiments. Figure 2S.8 compares these spectra with those reported for OCP^{O} in 3hECN-containing preparations in previous work. It is notable that the simulation for CAN in chloroform solution (Figure 2S.7) deviates less from the experimental spectrum, which suggests that the fraction of the ground-state ensemble with distorted conformations is smaller than in OCP^{O} .

Having simulated the absorption spectra, we then calculated the fluorescence spectra that would result from the same model parameters. The calculated fluorescence spectra exhibit mirror symmetry with respect to the calculated absorption spectra, as is required by hypothesis for the displaced harmonic potentials used in the MBO picture, so they exhibit the same line shapes and resolved vibronic structure. The evidently poor description of the fluorescence spectra by the MBO models indicates that the fluorescence emission arises from an excited-state structure undergoing fast dynamics along resonance Raman inactive coordinates (Figure 2.3).

2.S.2. Numerical simulations of absorption and fluorescence spectra for OCP^o with 3hECN using the Multimode Brownian Oscillator (MBO) model

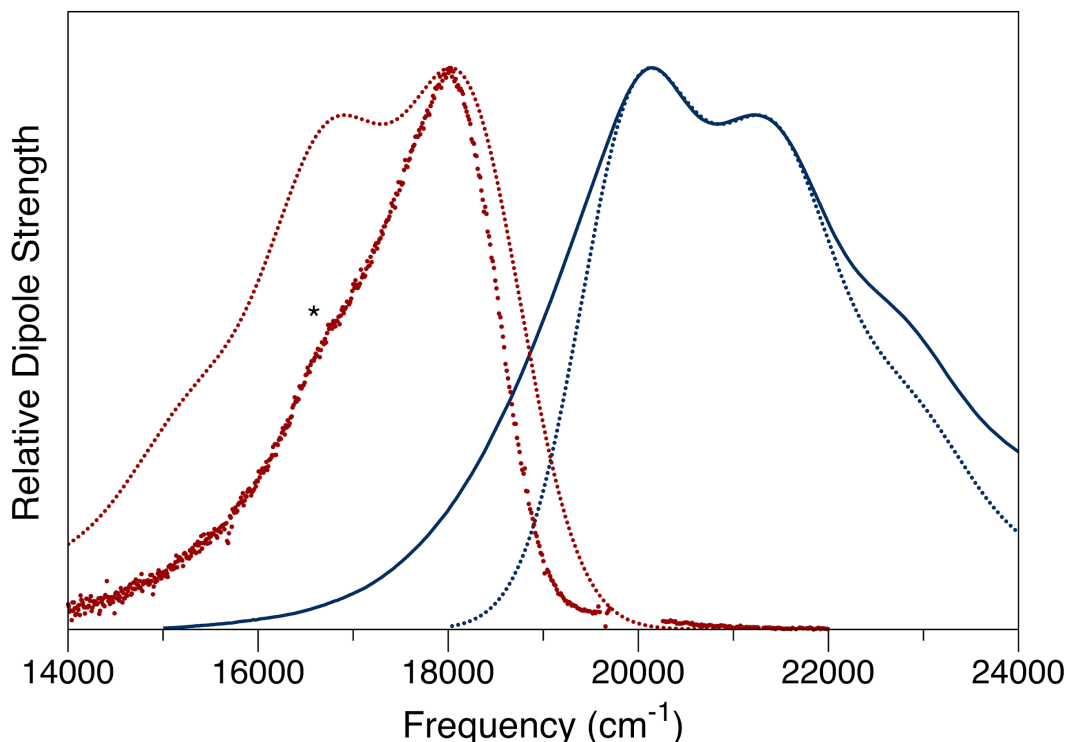


Figure 2S.1. Absorption (blue) and fluorescence (red data points) spectra of OCP^o measured at 23 °C with 3hECN incorporated as the bound carotenoid. The excitation monochromator for the fluorescence was tuned to 500 nm (20000 cm⁻¹). The intensities are plotted as dipole strengths, $\epsilon(\nu)/\nu$ and $\lambda^2 F(\nu)/\nu^3$, with normalization to peak intensity. The asterisk at 16500 cm⁻¹ marks the wavenumber of the nonresonant Raman band from water (shift of 3500 cm⁻¹). Superimposed on the experimental spectra are calculated absorption (blue dotted curve) and fluorescence (red dotted curve) spectra obtained from a numerical simulation with the multimode Brownian oscillator (MBO) model. The model parameters are listed below in Table 2S.2. This is the best model we obtained. The parameter choices obtain a good description of the vibronic structure observed in the absorption spectrum; the simulated fluorescence spectrum obtained with the same parameters exhibits approximately the same Stokes shift observed in the experimental spectrum, but the line width and vibronic structure is not well described.

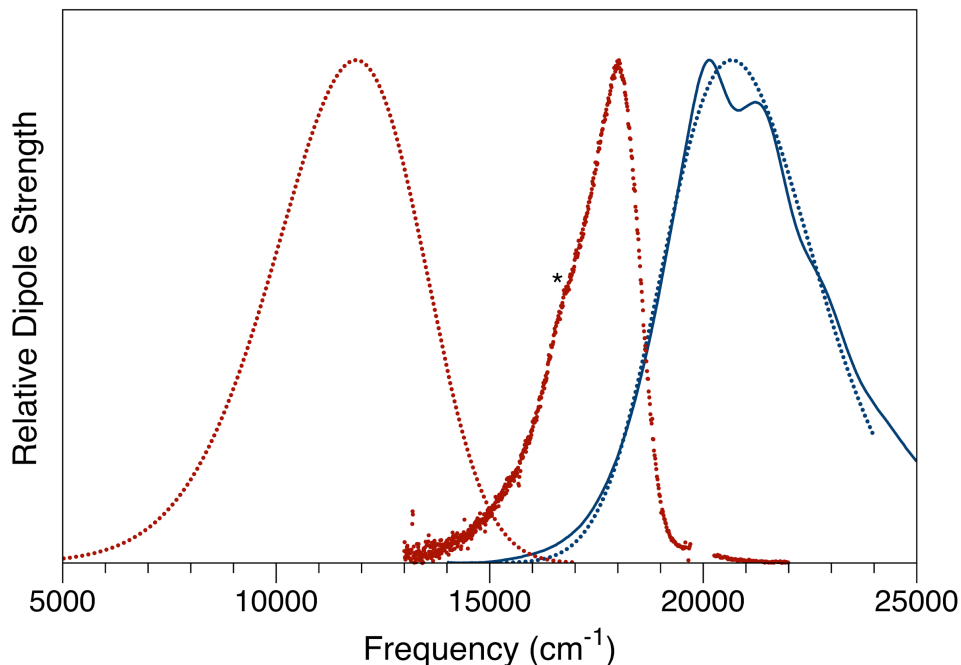


Figure 2S.2. Absorption and fluorescence spectra of OCP⁰ measured at 23 °C with 3hECN incorporated as the bound carotenoid. The simulated spectra obtained here with the model parameters listed below in Table 2S.2 obtain a better description of the red onset of the absorption spectrum, in the 15000–17000 cm⁻¹ region; but the result is a much larger Stokes shift for the fluorescence than is observed.

Table 2S.2. MBO model parameters^a used for the simulation of the absorption spectra from 3hECN in OCP⁰ in Figure 2S.2.

Mode	λ (cm ⁻¹)	ω_v (cm ⁻¹)	τ (fs)
Gaussian (<i>G</i>)	350	—	30
Exponential (<i>E</i> ,1)	1200	—	3000
Exponential (<i>E</i> ,2)	2000	—	100000
Vibrational (<i>v</i> ,1)	300	1150	2000
Vibrational (<i>v</i> ,2)	980	1525	2000
Total	4830	—	—

^aSee Equation 2S.1 and the text; $\omega_{eg} = 21100$ cm⁻¹.

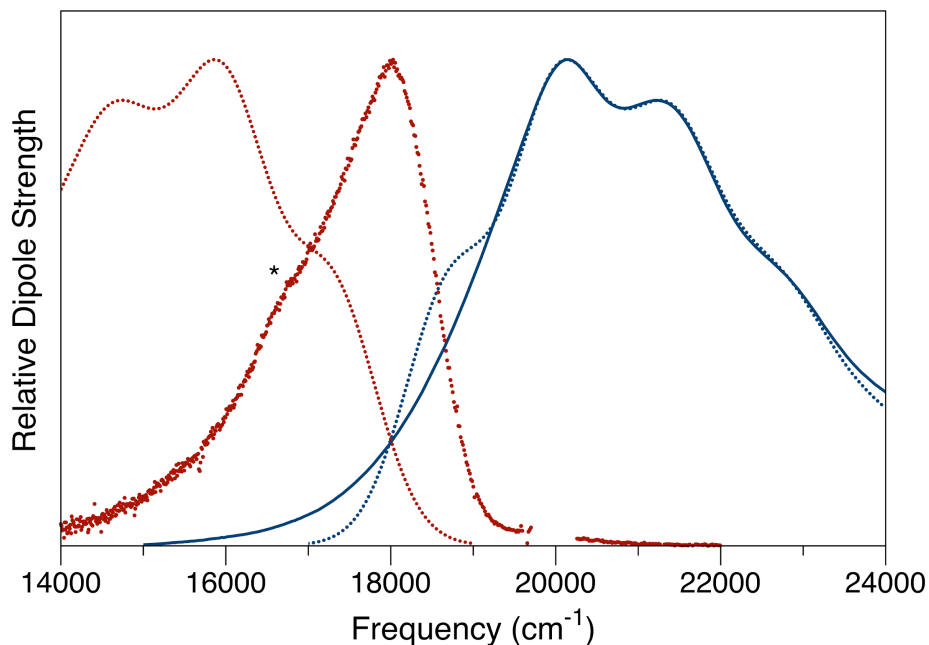


Figure 2S.3. Absorption and fluorescence spectra of OCP⁰ measured at 23 °C with 3hECN incorporated as the bound carotenoid. The simulated spectra obtained here with the model parameters listed below in Table 2S.3 model the resolved vibronic structure using an alternate set of parameters. The vibronic features at peak absorption are well described, but these parameters produce a stronger 0–0 peak at 18500 cm⁻¹ than observed in the experimental spectrum. Also, the Stokes shift of the fluorescence is much larger than is observed.

Table 2S.3. MBO model parameters^a used for the simulation of the absorption spectra from 3hECN in OCP⁰ in Figure 2S.3.

Mode	λ (cm ⁻¹)	ω_v (cm ⁻¹)	τ (fs)
Gaussian (<i>G</i>)	250	—	30
Exponential (<i>E</i> ,1)	240	—	3000
Exponential (<i>E</i> ,2)	395	—	100000
Vibrational (<i>v</i> ,1)	1120	1150	2000
Vibrational (<i>v</i> ,2)	1250	1525	2000
Total	3255	—	—

^aSee Equation 2S.1 and the text; $\omega_{eg} = 21200$ cm⁻¹.

2.S.3. Numerical simulations of absorption and fluorescence spectra for OCP⁰ with CAN using the Multimode Brownian Oscillator (MBO) model

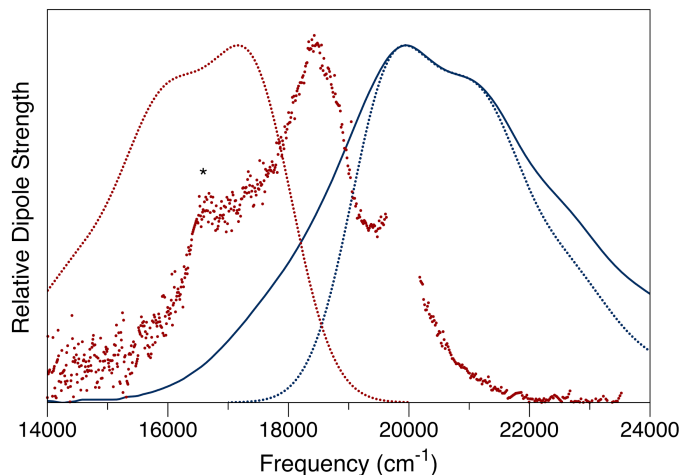


Figure 2S.4. Absorption and fluorescence spectra of OCP⁰ measured at 23 °C with 3hECN incorporated as the bound carotenoid. The simulated spectra obtained here with the model parameters listed below in Table 2S.4 describe the best model we obtained for CAN in OCP⁰. As for the best model for 3hECN in OCP⁰ (Figure 2S.1), a good description of the vibronic structure observed in the absorption spectrum is provided by this model, but here the Stokes shift, line width, and vibronic structure is not well described.

Table 2S.4. MBO model parameters^a used for the simulation of the absorption spectra from CAN in OCP⁰ in Figure 2S.4.

Mode	λ (cm ⁻¹)	ω_v (cm ⁻¹)	τ (fs)
Gaussian (<i>G</i>)	350	—	30
Exponential (<i>E</i> ,1)	175	—	3000
Exponential (<i>E</i> ,2)	650	—	100000
Vibrational (<i>v</i> ,1)	140	1150	2000
Vibrational (<i>v</i> ,2)	1110	1525	2000
Total	2425	—	—

^aSee Equation 2S.1 and the text; $\omega_{eg} = 20975$ cm⁻¹.

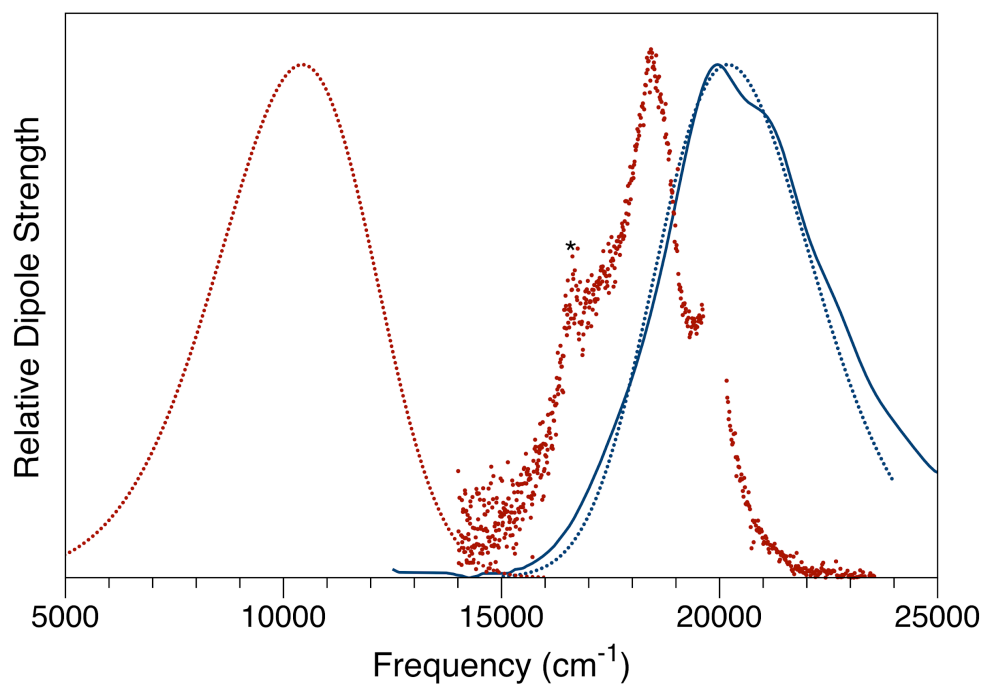


Figure 2S.5. Absorption and fluorescence spectra of OCP⁰ measured at 23 °C with CAN incorporated as the bound carotenoid. The simulated spectra obtained here with the model parameters listed below in Table 2S.5 describe the red tail of the absorption spectrum pretty well, but the result is a much larger Stokes shift for the fluorescence than is observed.

Table 2S.5. MBO model parameters^a used for the simulation of the absorption spectra from CAN in OCP⁰ in Figure 2S.5.

Mode	λ (cm ⁻¹)	ω_v (cm ⁻¹)	τ (fs)
Gaussian (<i>G</i>)	350	—	30
Exponential (<i>E</i> ,1)	1600	—	3000
Exponential (<i>E</i> ,2)	2100	—	100000
Vibrational (<i>v</i> ,1)	140	1150	2000
Vibrational (<i>v</i> ,2)	1100	1525	2000
Total	5290	—	—

^aSee Equation 2S.1 and the text; $\omega_{eg} = 20600$ cm⁻¹.

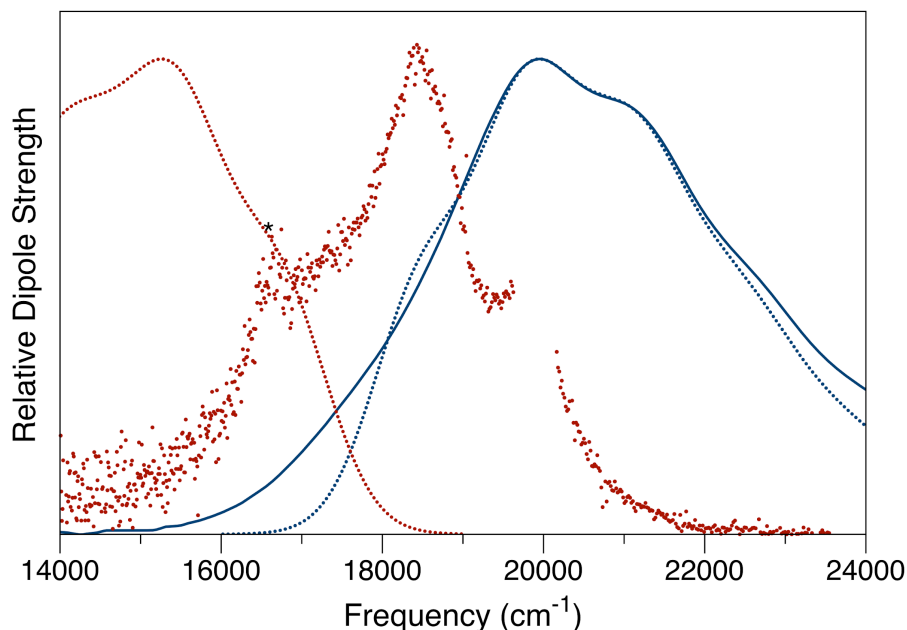


Figure 2S.6. Absorption and fluorescence spectra of OCP⁰ measured at 23 °C with CAN incorporated as the bound carotenoid. The simulated spectra obtained here with the model parameters listed below in Table 2S.6 provide an alternate description of the vibronic structure. The vibronic features at peak absorption are well described, but these parameters produce a stronger 0–0 transition than observed. Also, the Stokes shift of the fluorescence is much larger than observed.

Table 2S.6. MBO model parameters^a used for the simulation of the absorption spectra from CAN in OCP⁰ in Figure 2S.6.

Mode	λ (cm ⁻¹)	ω_v (cm ⁻¹)	τ (fs)
Gaussian (<i>G</i>)	220	—	30
Exponential (<i>E</i> ,1)	2200	—	3000
Exponential (<i>E</i> ,2)	2500	—	100000
Vibrational (<i>v</i> ,1)	150	1150	2000
Vibrational (<i>v</i> ,2)	935	1525	2000
Total	6005	—	—

^aSee Equation 2S.1 and the text; $\omega_{eg} = 20860$ cm⁻¹.

2.S.4. Absorption and Fluorescence Spectra from Canthaxanthin in Chloroform Solvent with Numerical Simulations

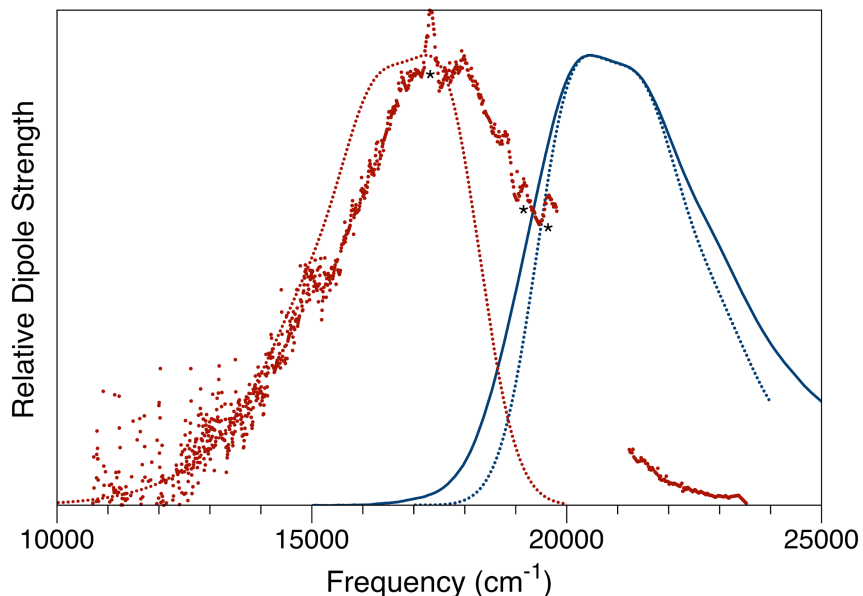


Figure 2S.7. Absorption and fluorescence spectra of CAN in chloroform solvent at 23 °C. The excitation monochromator for the fluorescence was tuned to 490 nm (20408 cm⁻¹). Asterisks mark nonresonant Raman bands from the chloroform solvent. The simulated spectra shown here were obtained with the parameters listed in Table 2S.7.

Table 2S.7. MBO model parameters^a for the simulation of the absorption and fluorescence spectra from CAN in trichloromethane solution.

Mode	λ (cm ⁻¹)	ω_v (cm ⁻¹)	τ (fs)
Gaussian (<i>G</i>)	300	—	30
Exponential (<i>E</i> ,1)	300	—	285
Exponential (<i>E</i> ,2)	630	—	4150
Vibrational (<i>v</i> ,1)	300	1150	2000
Vibrational (<i>v</i> ,2)	1040	1525	2000
Total	2570	—	—

^aSee Equation 2S.1 and the text; $\omega_{eg} = 21420$ cm⁻¹.

2.S.5. Comparison of ground-state absorption spectra for 3hECN-containing preparations of OCP⁰

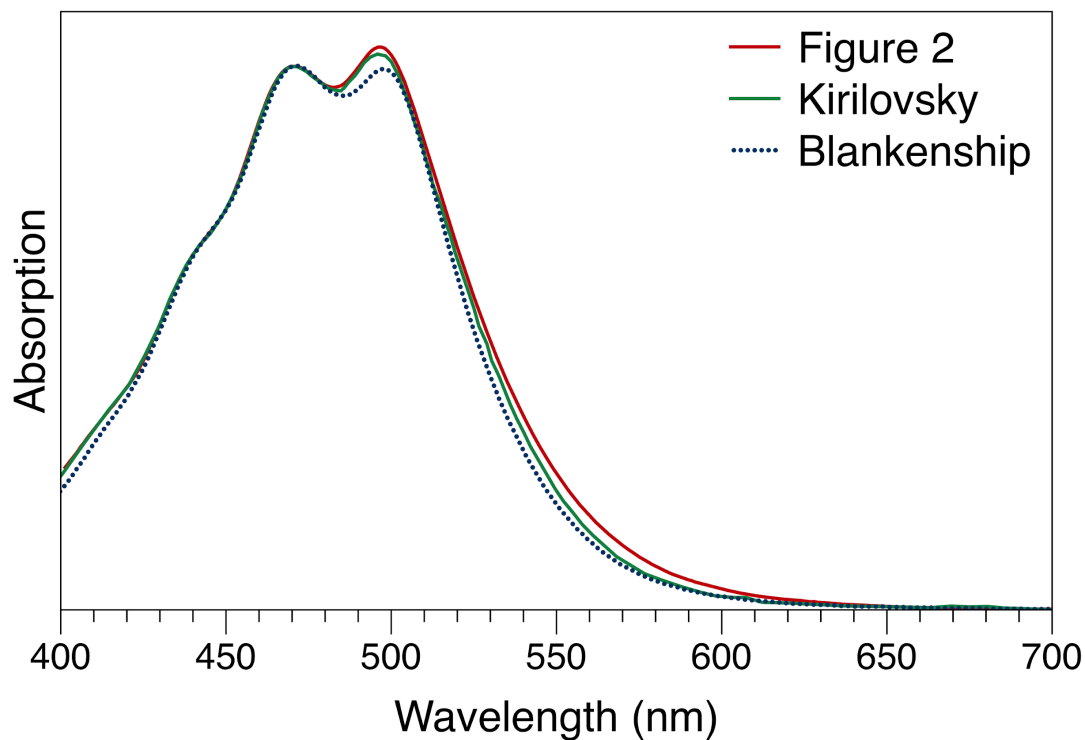


Figure 2S.8. Comparison of ground-state absorption spectra from OCP⁰ preparations from *Arthrospira platensis* containing 3hECN from the present work (Figure 2.1(a)) and from the Kirilovski⁵⁷ and Blankenship⁷⁰ laboratories. The spectra are normalized at the peak of the second vibronic peak to project out differences in the intensity of the first vibronic peak and of the red absorption onset.

2.S.6. Structure of the carotenoid binding site in OCP^o

```
Arthrospira_Platensis 19 DVVPAT I ARFKQLSAEDQLAL IWFAYLEMGKT IT I AAPGAANMQFAENT 67
Arthrospira_Maxima 19 DVVPAT I ARFKQLSAEDQLAL IWFAYLEMGKT IT I AAPGAANMQFAENT 67

Arthrospira_Platensis 68 LQE I ROMTPLQQTQAMCDLANRTDTP I CRTYASWSPN I KLGFWYELGRF 116
Arthrospira_Maxima 68 LQE I ROMTPLQQTQAMCDLANRTDTP I CRTYASWSPN I KLGFWYELGRF 116

Arthrospira_Platensis 117 MDQGLVAP I PEGYKLSANANA I LVT IQG IDPGQO I TVLRNCVVDMGF 163
Arthrospira_Maxima 117 MDQGLVAP I PEGYKLSANANA I LVT IQG IDPGQO I TVLRNCVVDMGF 163
```

Figure 2S.9. Alignment of the amino acid sequences in the NTD from *Arthrospira platensis* (Accession number YP_005071727) and *Arthrospira maxima* (from structure 5UI2.pdb). The NTD amino acid sequence is fully conserved over these two species.

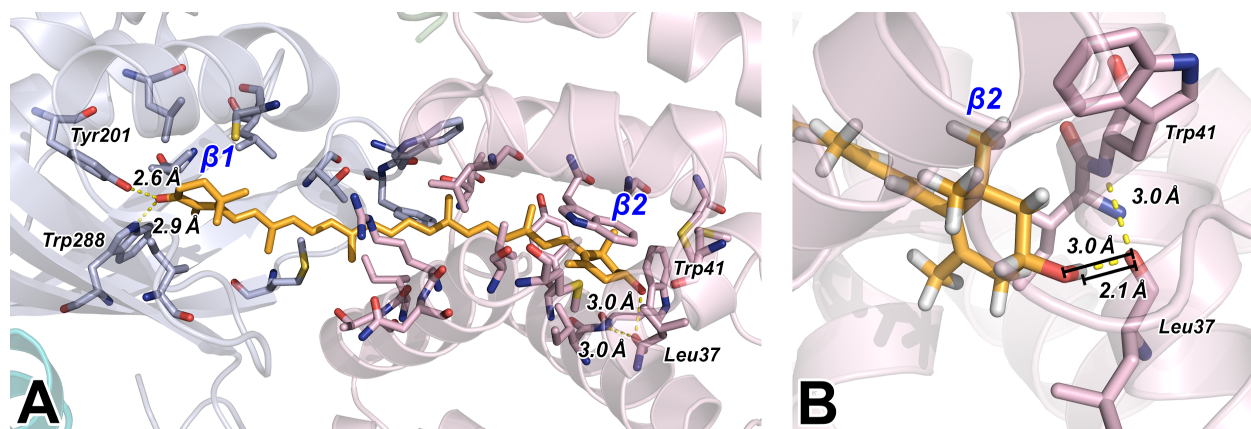


Figure 2S.10. Protein–ketocarotenoid hydrogen bonding interactions in *Synechocystis* sp. PCC 6803 OCP^o: (a) for 3hECN, from structure 5TV0.pdb; (b) detail from a rotated vantage point of the $\beta 2$ ring's hydrogen bonding interaction between the hydroxyl group and the carbonyl on Leu37. The crystal structure in this case explicitly includes hydrogen atoms for the carotenoid. For comparison with Figure 2.2.

Table 2S.8. Distances in OCP^O crystal structures between protein groups to the carbonyl or hydroxyl substituents on the carotenoid β -cyclohexene rings.^a

	4XB5 (CAN)	5UI2 (3hECN)	5TV0 (3hECN)
Tyr 201/203 R–OH ... β 1 O=C	2.6 Å	2.9 Å	2.6 Å
Trp 288/290 R–NH ... β 1 O=C	2.9 Å	2.9 Å	2.9 Å
β 2 C–O ... O=C Leu37	—	2.7 Å	3.0 Å
β 2 C–OH ... O=C Leu37	—	—	2.1 Å ^b
β 2 C=O ... O=C Leu37	4.4 Å	—	—

^aThe β 1 and β 2 rings are as labelled in Figures 2.4 and 2S.10.

^bThe 5TV0 structure has explicit protons on the 3hECN carotenoid, so this is the only structure that provides the apparent hydrogen-bonding distance between the β 2 hydroxyl proton and the Leu37 carbonyl acceptor. The hydroxyl O–H ... O (carbonyl) bond angle is 152 degrees.

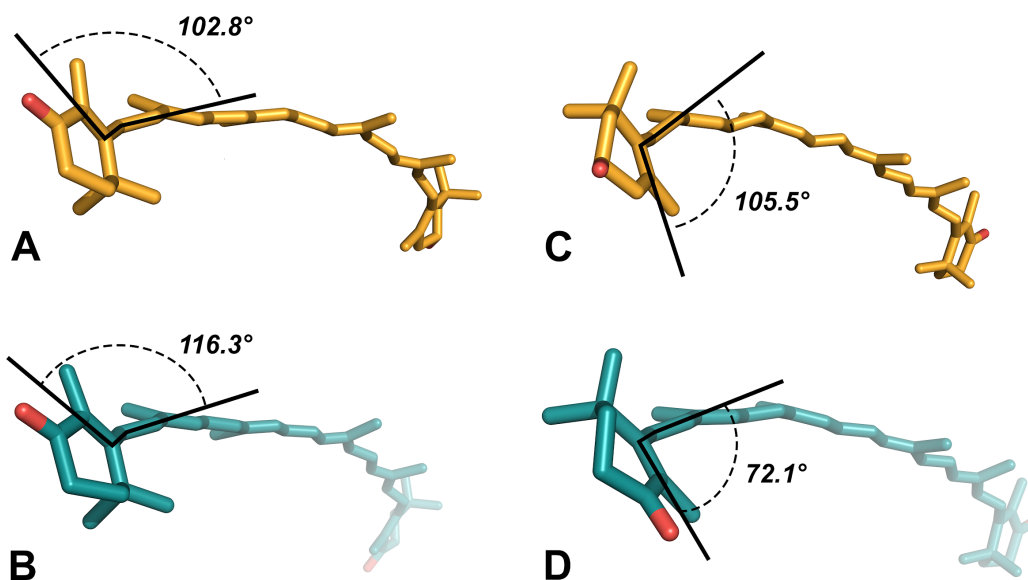


Figure 2S.11. Conformation of the end rings of 3hECN (orange, top) and CAN (teal, bottom) in the 5UI2 (3hECN) and 4XB5 (CAN) crystal structures, respectively, as viewed from the (a,b) β 1 and (c,d) β 2 ends. The dihedral angle between the plane of the ring and the plane of the conjugated polyene backbone is indicated for each structure.

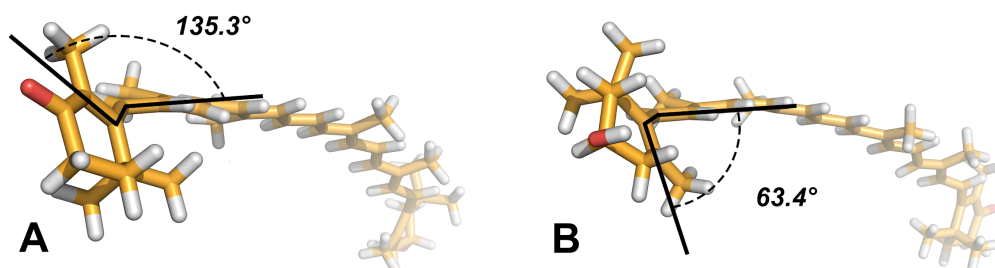


Figure 2S.12. As in Figure 2S.8, but for 3hECN in the 5TV0.pdb structure: as viewed from the (a) β 1 and (b) β 2 ends.

Chapter 3. Fluorescence anisotropy detection of barrier crossing and ultrafast conformational dynamics in the S₂ state of β-carotene*

3.1. Summary

Carotenoids are usually only weakly fluorescent despite being very strong absorbers in the mid visible because their first two excited singlet states, S₁ and S₂, have very short lifetimes. In order to probe the structural mechanisms that promote nonradiative decay of the S₂ state to the S₁ state, a series of fluorescence lineshape and anisotropy measurements were made using a prototype carotenoid, β-carotene, in four aprotic solvents. The anisotropy measurements of the fluorescence emission bands originating from the S₂ and S₁ states reveal that the emission transition dipole moment rotates as much as 50° relative to that of the absorption transition dipole moment. These rotations are initiated during ultrafast evolution on the S₂ state potential energy surface and persist upon nonradiative decay to the S₁ state. Electronic structure calculations account for the anisotropy results in terms of torsional and pyramidal distortions near the center of the isoprenoid backbone. The temperature dependence of the oscillator strength and anisotropy indicate that nonadiabatic passage from S₂ through a conical intersection to S₁ is promoted by out-of-plane motions of the isoprenoid backbone being hindered by solvent friction.

* This chapter is adapted from the following publication:
J. K. Gurchiek, Justin B. Rose, Matthew J. Guberman-Pfeffer, Ryan W. Tilluck, Soumen Ghosh, José A. Gascón, and Warren F. Beck. Fluorescence Anisotropy Detection of Barrier Crossing and Ultrafast Conformational Dynamics in the S₂ State of β-Carotene. *J. Phys. Chem. B* 2020, 124 (41), 9029-9046

3.2. Introduction

In this chapter, a test of this picture for the light-induced dynamics in carotenoids using the continuous-wave line shape, quantum yield, and anisotropy of the fluorescence emission from the β -carotene in several aprotic solvents is reported. Emission from molecules moving on a gradient on the S_2 potential energy surface with respect to out-of-plane coordinates after passage over a low activation energy barrier gives rise to a broad fluorescence spectrum with a low anisotropy, with the anisotropy decreasing as the excitation source is scanned to the blue over the vibronic structure of the absorption spectrum from the 0–0 region. A weaker fluorescence spectrum with partially resolved vibronic structure arising from the S_1 state is detected in the near-IR, and it also exhibits a strong intensity dependence on the excitation wavelength. The minimum fluorescence anisotropy detected at long emission wavelengths is consistent with a large internal rotation of the emission transition dipole moment (TDM), as much as 50° in nonpolar solvents. Because the TDM is aligned within a few degrees of the molecular frame of the isoprenoid backbone in all-trans polyenes,^{16,116,117} these results indicate directly that β -carotene undergoes large-amplitude out-of-plane conformational motions as nonradiative decay from the S_2 state to the S_1 state occurs. This picture is further supported by studies of the fluorescence emission at low temperatures, which show that it is possible to observe stronger emission from a dynamic intermediate evolving on the S_2 state that may correspond to S_x or to its precursor from the photoexcited Franck–Condon structure. Companion electronic structure calculations are then used to determine how the permanent dipole moment and the rotation of the emission TDM are induced by torsional and pyramidal distortions of the isoprenoid backbone.

These calculations suggest that the fluorescence anisotropy results are consistent with a zwitterionic structure with a pyramidal conformation in the center of the isoprenoid backbone.

3.3. Experimental and Computational

3.3.1. Sample Preparation

β -carotene from Sigma/Aldrich (C9750-5G) was purified by Amy LaFountain in the Frank laboratory at the University of Connecticut by high-performance liquid chromatography (HPLC) on a Waters 600E/600S multisolvent delivery system equipped with a 2996 photodiode array detector, as described previously.¹¹⁸ Additional details are provided in the Supporting Information. After removal of the solvent under a stream of nitrogen gas, the purified β -carotene samples were stored in darkness in a -70 °C freezer. For the present experiments, β -carotene samples were removed from cold storage, divided into aliquots, and then dissolved in a particular solvent to obtain an absorbance of 0.2 at the peak of the absorption spectrum (460 nm in hexane) for a 1 cm optical path length. The samples were then centrifuged at $17000 \times g$ in a desktop microcentrifuge for 10 min to remove light-scattering particles. Samples were held in 1 cm fused-silica cuvettes either in a Quantum Northwest Peltier-effect temperature controller or in a Janis liquid nitrogen cryostat (for $T < 200$ K).

3.3.2. Absorption spectroscopy

Room temperature (23°C) absorption spectra were recorded with a Shimadzu UV-2600 spectrophotometer with a spectral bandpass of 2 nm. With fluorescence samples mounted in the Peltier-effect temperature controller or the liquid nitrogen cryostat, absorption spectra were recorded in situ at the indicated temperature with a single-beam spectrometer, which was

assembled from an Ocean Optics DH-2000 light source, Ocean Optics QP400-1-UV-VIS fiber optic cables, and an Ocean Optics USB4000 spectrograph/CCD detector (0.1 nm bandpass).

3.3.3. Fluorescence Spectroscopy

Fluorescence spectroscopy with continuous excitation was performed with a home-built spectrometer incorporating a broadband LED and a compact double monochromator (2 nm bandpass) for the excitation light source. A grating spectrograph with a 0.15 m focal length (4 nm bandpass) and a back-illuminated CCD detector was used as the detection system. This instrument is an improved setup based on the one we described previously.¹¹⁹ The orientations of the linear planes of polarization of the excitation and emission beams were selected by calcite Glan-Thompson and Glan-Taylor polarizers, respectively, with the latter mounted in a motorized rotation stage. The emission spectra were corrected for the wavelength dependences of the emission optics, spectrograph, and CCD detector. The details of the instrumentation and of the protocols used to measure the fluorescence emission and anisotropy are reported in the Supporting Information. The spectra shown in this paper were acquired with very low intensity excitation beams (for example, 5.86 μW at 460 nm), and the samples were repeatedly allowed to recover in darkness during acquisition of dark background spectra prior to the recording of additional spectra. Each reported spectrum was obtained as the average, after scan-to-scan rejection of cosmic ray spikes, of 16 four-minute exposures of the CCD camera for a given polarization state. Figure 2S.1 presents fluorescence emission and anisotropy spectra from rhodamine 6G in glycerol, which was employed as a reference sample for the quantum yield and anisotropy measurements.

The absorption spectrum of the β -carotene samples was measured before and after the fluorescence data acquisition cycle in order to determine if permanent photobleaching occurred or if photoproducts were accumulated. Photobleaching of β -carotene due to formation of radical cation species via photoinduced charge transfer reactions¹²⁰ has been detected in chloroform solutions via near-IR absorption transients.^{121,122} No changes in absorption were detected in any of the samples monitored during these experiments.

3.3.4. Electronic Structure Calculations

Electronic structure calculations were performed with the B3LYP hybrid functional,^{123,124} a 6-31G(d) basis set, and an ultrafine grid for integration, as implemented in Gaussian 16 revision A.01.¹²⁵ As discussed below, relaxed potential energy scans were conducted around each double bond of β -carotene and of those in a truncated analogue in which the β -ionone rings were replaced by hydrogens. These scans were conducted around each bond by varying the dihedral angle from 180° to 90°. The all-trans and twisted conformers were submitted to time-dependent density functional theory (TD-DFT) calculations under the Tamm-Dancoff approximation using the CAM-B3LYP/6-31G(d) model chemistry.¹²⁶ For full-length, all-trans β -carotene, this level of theory delivers an $S_0 \rightarrow S_2$ vertical excitation energy within ~ 0.08 eV (~ 12 nm) of the experimental absorption maximum at 460 nm. This combination of two different levels of DFT and/or basis sets, one for ground state optimization and the other for excited state energies, has been used before and particularly in the context of carotenoids.^{35,36} The transition density for the $S_0 \rightarrow S_2$ excitation was generated with MultiWFN¹²⁷ and visualized in Gaussview.

3.4. Results

3.4.1 Fluorescence Spectra

Figure 2 compares the room temperature (23 °C) absorption spectrum with the fluorescence spectra observed at four excitation wavelengths from β -carotene in hexane solvent. As discussed previously by Gillbro and Cogdell,⁸ the fluorescence and absorption spectra overlap over the ~480–520 nm region, which is consistent with an assignment of the emission to the S_2 state. Owing to the low quantum yield, $\sim 10^{-6}$, the broad fluorescence lineshape is decorated with sharper line shapes arising from light scattering at the excitation wavelength, from resonance Raman scattering at the C-C and C=C mode frequencies, and from non-resonance Raman scattering from the hexane solvent. The Raman signals move at fixed Stokes shifts (in wavenumbers) as the excitation wavelength is scanned across the absorption spectrum, revealing as they move that the obscured part of the fluorescence line shape lacks any resolved vibronic structure. In contrast, the absorption spectrum exhibits a partially resolved vibronic progression in the BLA coordinates. This observation indicates that the optically prepared S_2 state abruptly undergoes a change in electronic structure that increases the solvation reorganization energy (or system–bath coupling). Simulations of the absorption and fluorescence spectra using the multimode Brownian oscillator (MBO) model¹⁰⁰ are presented in the Supporting Information. The absorption transition would be expected to impact the chromophore–solvent interactions by increasing the chromophore's permanent dipole moment and/or the molecular size relative to that of the surrounding solvent cavity.

As the excitation wavelength is scanned from the 0–0 region (Figure 3.1a) over the vibronic structure of the absorption spectrum (Figures 3.1b–d), the fluorescence spectrum exhibits a

significant broadening in the emission bandwidth. Especially with excitation at 450 nm (Figure 3.1c) or 430 nm (Figure 3.1d), the emission is strengthened especially in the near-IR, >600 nm region. The origin of the broadening is made clearer by comparing the 490 nm and 430 nm spectra replotted as the emission oscillator strength in comparison to the fluorescence anisotropy (Figure 3.2).

The oscillator (or dipole) strengths $\epsilon(\nu)/\nu$ and $\lambda^2 F(\nu)/\nu^3$ express the squares of the absorption and fluorescence transition probabilities^{88,128} with respect to the wavenumber, ν , as determined by the absorption and the fluorescence intensity, $\epsilon(\nu)$ and $F(\nu)$, respectively, and with λ standing for the wavelength.¹²⁹⁻¹³² In Figure 3.2, the fluorescence oscillator strength spectra obtained with excitation at 490 nm and 430 nm are plotted with consistent scaling factors after normalizing them for the excitation light intensity. Tuning of the excitation wavelength to 430 nm from 490 nm substantially increases the oscillator strength of the fluorescence emission across the entire detection range but especially below $\sim 18000 \text{ cm}^{-1}$.

The oscillator strength spectra make it clear that a second fluorescence band is superimposed on the tail of the main emission band from S_2 . This second band is assigned to emission from the S_1 state following nonradiative decay from S_2 . The contribution from the S_1 fluorescence band is not nearly as obvious in the intensity spectra plotted in Figure 3.1 due to the effective attenuation by the fixed wavelength bandpass of the emission spectrograph. Although the signal/noise ratio is relatively poor in this region of the spectrum owing to the decreasing sensitivity at long wavelengths of the silicon CCD detector used in these experiments, one can discern the weak emission band from S_1 in the spectrum obtained with 490 nm excitation (Figure 3.1a) from its apparent peak maximum in the $\sim 12500\text{--}13000 \text{ cm}^{-1}$ range. A weak S_1 spectrum from β -carotene

in carbon disulfide in this wavenumber region was detected previously with a germanium detector and laser excitation by Andersson et al.¹³³

The S_1 band observed with excitation at 430 nm (Figure 3.1b), however, is substantially stronger than observed with 490 nm excitation. Its line shape is broader, extending at least from 18000 cm^{-1} to the low frequency limit of the detected spectra, and its peak maximum is markedly blue shifted. Further, the intensity is modulated over the 13500–14000 cm^{-1} range, which may arise from partially resolved vibronic structure. The S_1 fluorescence spectrum reported by Andersson et al.¹³³ was assigned a weak vibronic progression in the BLA mode frequencies.

3.4.2. Fluorescence Anisotropy Spectra

The fluorescence anisotropy, r , is calculated from the linear polarization emission components detected parallel and perpendicular to the plane of polarization of the excitation light, F_{\parallel} and F_{\perp} , as

$$r = \frac{F_{\parallel} - F_{\perp}}{F_{\parallel} + 2F_{\perp}} \quad (3.1)$$

The anisotropy reports the angle θ between the emission and absorption TDMs, the latter as photoselected from the randomly oriented ground-state ensemble present in solution,⁸⁸

$$r = r_0 P_2(\theta) = r_0(3 \cos^2 \theta - 1)/2 \quad (3.2)$$

In this equation, r_0 is for the maximum anisotropy, 0.4, which corresponds to parallel TDM directions for the absorption and emission TDMs, and P_2 is the second Legendre polynomial. As the emission TDM is rotated away from alignment with the absorption TDM, the anisotropy

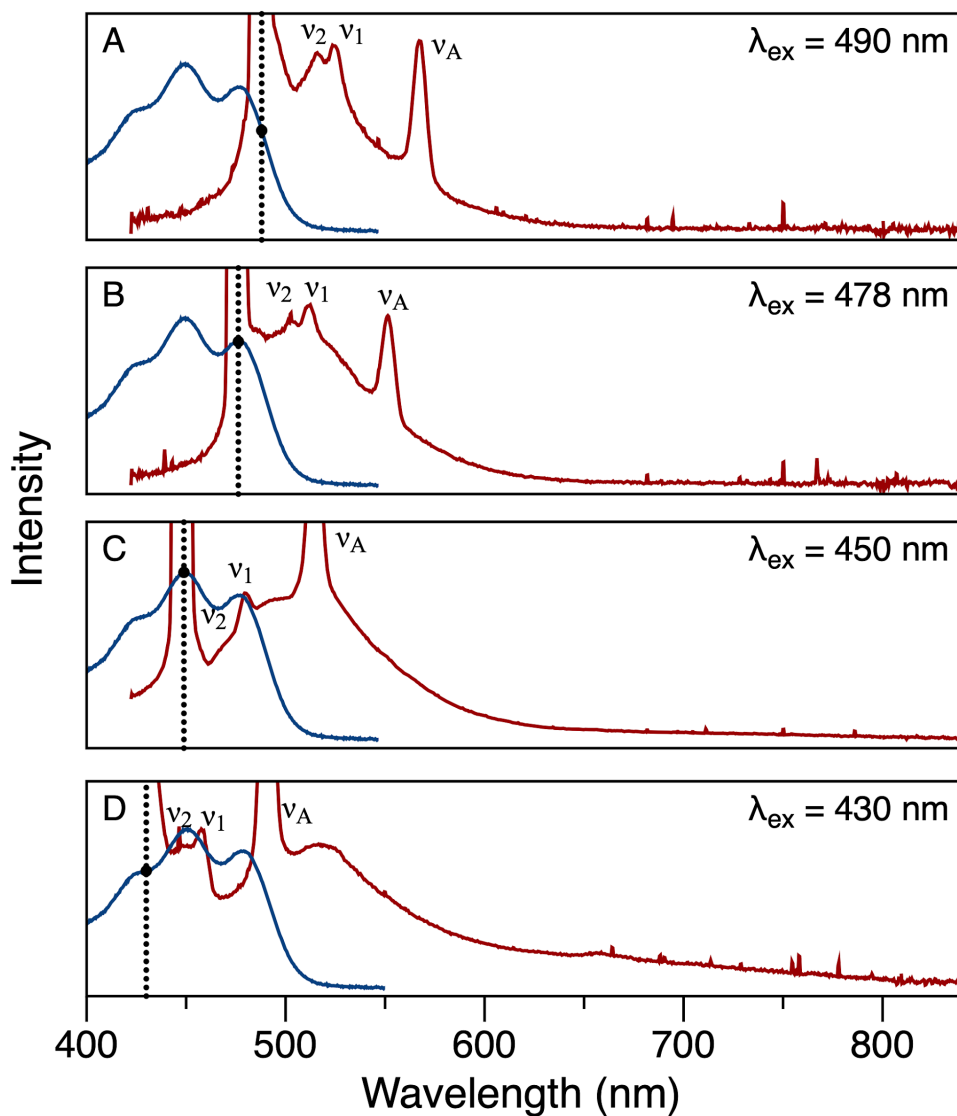


Figure 3.1. Absorption (blue) and fluorescence emission (red) spectra at four excitation wavelengths from β -carotene in hexane solvent at 23 °C. For the fluorescence spectra, the emission polarizer was oriented at the magic angle (54.6°) with respect to the excitation polarizer. The excitation wavelength is marked in each panel with a vertical dashed line. The positions of resonance Raman peaks from β -carotene ($\nu_1 = 1517 \text{ cm}^{-1}$ and $\nu_2 = 1157 \text{ cm}^{-1}$)¹³⁴ and for a non-resonance Raman peak from the hexane solvent ($\nu_A = 2966 \text{ cm}^{-1}$)¹³⁵ are marked.

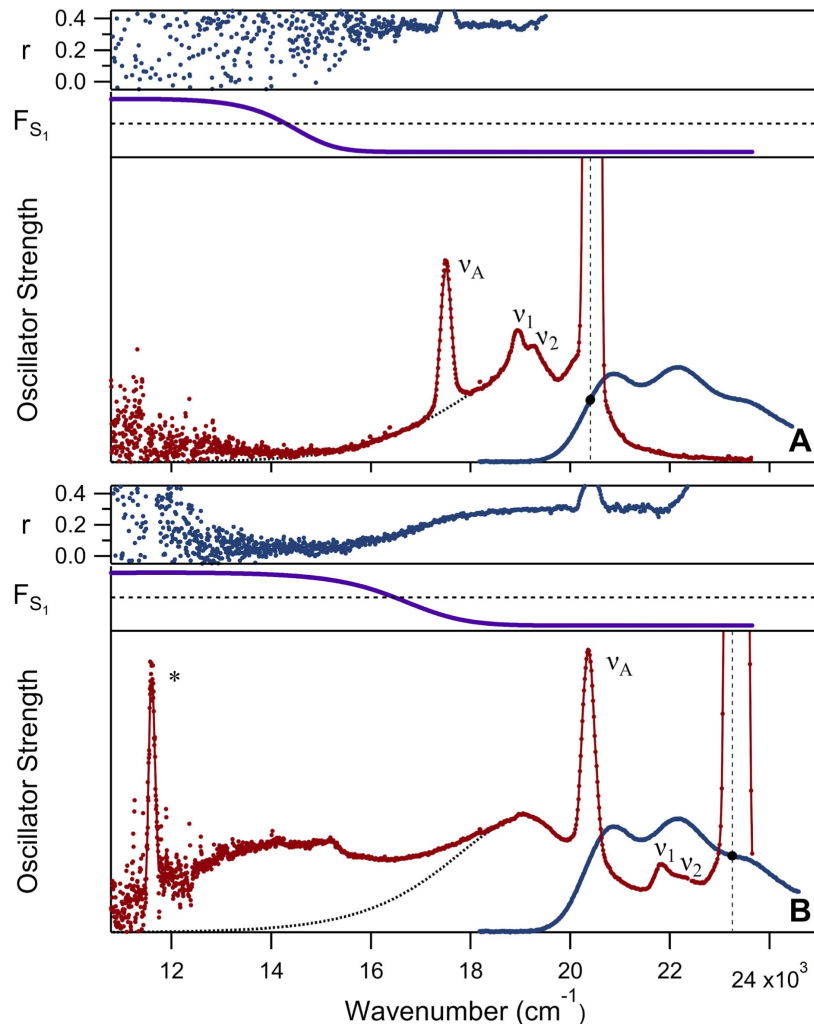


Figure 3.2. Fluorescence oscillator strength and anisotropy (r) spectra for β -carotene in hexane at 293 K: (a) with excitation at 490 nm ($20,400 \text{ cm}^{-1}$); (b) with excitation at 430 nm ($23,250 \text{ cm}^{-1}$). The magic-angle fluorescence oscillator strength (red) is plotted after correction for the intensity of the excitation light at the two wavelengths with the same intensity scaling in panels (a) and (b). The excitation wavenumber is marked in each panel with a vertical dashed line. The absorption oscillator strength (blue) is arbitrarily scaled to mirror that of the S_2 fluorescence emission line shape. A baseline for the S_1 emission is suggested by a lognormal lineshape for the red tail of the S_2 emission. F_{S_1} (purple) estimates the fraction of the fluorescence oscillator strength from the S_1 state; $F_{S_1} = 0.5$ is marked by the dashed line. The positions of resonance Raman peaks from β -carotene ($\nu_1 = 1517 \text{ cm}^{-1}$ and $\nu_2 = 1157 \text{ cm}^{-1}$)¹³⁴ and for a non-resonance Raman peak from the hexane solvent ($\nu_A = 2966 \text{ cm}^{-1}$)¹³⁵ are marked. Also marked (*) is the second-order excitation light scattering peak.

decreases. Complete loss of memory of the photoselected absorption TDM direction due to rotational diffusion would result in a full depolarization of the fluorescence emission and an anisotropy of 0.0, but the rotational correlation time measured for β -carotene in hexane determined using optical Kerr effect measurements is 115 ps at 20°C.¹³⁶ Depolarization of the fluorescence from S_2 from rotational diffusion is entirely negligible owing to the <150 fs lifetime of the S_2 state. Further, for the S_1 emission, at most a 5 percent decrease in the fluorescence anisotropy would accompany rotational diffusion averaged over the 10 ps lifetime^{22,43,137,138} of the S_1 state. Thus, fluorescence anisotropies much lower than 0.4 arise in β -carotene from an internal rotation of the emission TDM relative to the photoselected direction of the absorption TDM.

The fluorescence anisotropy spectra plotted in Figure 3.2 decrease monotonically as the emission frequency extends into the near-IR region except in the neighborhood of Raman scattering features, which are highly polarized. This trend indicates that the fluorescence from the S_1 state exhibits a lower anisotropy than the S_2 state. The contribution of the fluorescence from the S_1 state to the measured anisotropy at a given wavenumber can be estimated from the fraction of the total oscillator strength from the S_1 state, F_{S_1} , which is plotted above the main oscillator strength panels in Figure 3.2. Lognormal lineshapes⁹⁶ were applied here to estimate the oscillator strength from the S_2 state where it overlaps with that from the S_1 state; a similar approach was used by Andersson et al.¹³³

With excitation at 490 nm (Figure 3.2a), the minimum anisotropy observed in the S_2 emission region at 16,500 cm^{-1} is ~ 0.35 , which indicates only a 17° rotation of the emission TDM from the direction of the vertical absorption TDM using equation 3.2. A similar anisotropy value extends across the weak S_1 emission region, though the signal/noise ratio is very poor. With excitation at 430 nm (Figure 3.2b), however, the anisotropy is as low as 0.28 in the S_2 region,

implying a rotation of the emission TDM by 26° . An even lower anisotropy is then observed in the S_1 region, 0.05, corresponding to a rotation of the TDM by almost 50° . These results make it clear that tuning the excitation wavelength to shorter wavelengths over about a 3000 cm^{-1} range from the 0–0 transition results in an increased rotation of the emission TDM in both the S_2 and S_1 bands. Additional fluorescence anisotropy spectra from β -carotene in hexane showing this trend are presented in wavelength spectra provided in the Supporting Information.

3.4.3. Solvent dependence of the fluorescence emission and anisotropy from β -carotene

We carried out additional studies of the fluorescence properties of β -carotene in three additional aprotic solvents affording comparable solubility to that in hexane: chloroform (Figure 3.3), 2-methyltetrahydrofuran (2-MTHF, Figure 3.4), and carbon disulfide (Figure 3.5). These figures present the fluorescence oscillator strength and anisotropy spectra in these solvents in the same manner used above in Figure 3.2 for β -carotene in hexane. The Supporting Information presents wavelength plots of the fluorescence emission and anisotropy spectra in for these solvents as the excitation wavelength is tuned over the vibronic structure of the ground-state absorption spectrum. The fluorescence quantum yields and minimum anisotropies in the S_2 and S_1 fluorescence bands in each of the four solvents are compared in Table 3.1. The reported anisotropies are the minimum values observed in the spectral regions assigned to the S_2 and S_1 bands, estimated as discussed above as guided by the apparent fraction of the emission oscillator strength from S_1 , F_{S_1} . For S_2 we chose to measure the anisotropy at Stokes shifts above $\sim 3500\text{ cm}^{-1}$ so as to avoid regions where Raman scattering would be expected.

The trends in fluorescence lineshape, oscillator strength, and anisotropy described above for β -carotene in hexane that accompany tuning of the excitation wavelength over the $\sim 3000\text{ cm}^{-1}$

region above the 0–0 absorption transition are also observed in the three additional solvents. In chloroform (Figure 3.3b) and 2-MTHF (Figure 3.4b), the S_1 emission exhibits some weakly resolved vibronic structure; in contrast, the S_1 emission observed in carbon disulfide (Figure 3.5b) displays less vibronic structure but is perhaps ten times more intense than observed in the other solvents. In all three solvents, the S_2 fluorescence anisotropy is ~ 0.2 , somewhat lower than observed in hexane, whereas the fluorescence anisotropy from the S_1 state is significantly lower in the nonpolar solvents, ~ 0.06 , compared to that in the polar solvents, ~ 0.15 .

Several aspects of the results reported above have been observed previously by other workers, but the fluorescence line shape and anisotropy properties were not simultaneously connected in any prior work, to our knowledge. Gillbro and Cogdell⁸ reported a decrease in the fluorescence emission anisotropy from β -carotene in carbon disulfide at a single emission wavelength, 570 nm, as the excitation wavelength was scanned to the blue over the 500 nm to 400 nm range; fluorescence emission spectra over this excitation tuning range were not shown. The results described above for the S_2 emission are in line with their findings. To explain the anisotropy decrease, Gillbro and Cogdell proposed that the absorption spectrum contains two overlapping bands with distinct emission TDM directions. A similar argument was made by Oustramov et al.⁴⁰ to account for their observation that the fluorescence line shape of β -carotene deviates from mirror symmetry and from that expected from the Stepanov relation, which assumes that no structural rearrangements occur from the Franck–Condon structure and that the emission arises from the lowest vibrational level of the emitting state.¹³⁹ In fact, it was concluded in this work that the majority of the fluorescence emission with excitation near the 0–0 transition arises from optical preparation of the low lying B state of Tavan and Schulten mentioned in the introduction. Tuning of the excitation into the blue wavelengths associated in the present work

with the near-IR fluorescence was not reported nor was there any discussion of fluorescence anisotropy results.

We should point out at this point that the possible presence of overlapping transitions in the mid-visible absorption band of β -carotene does not really provide a satisfactory physical explanation for the correlated changes observed here in the fluorescence line shape and anisotropy. As shown below in the electronic structure calculations and consistent with previous work,^{16,133} the TDMs of all-trans carotenoids are well aligned longitudinally with the direction of the isoprenoid backbone. Contribution from $\pi \rightarrow \pi^*$ transitions with TDMs components in the transverse direction would be expected to be blue shifted from the main band and much weaker in oscillator strength. Further, linear dichroism spectra indicate that photoselection of ground-state molecules with cis configurations does not occur over the 430–500 nm excitation range.¹⁴⁰ The cis band in β -carotene is located at shorter wavelengths, ~300–350 nm.¹⁴¹

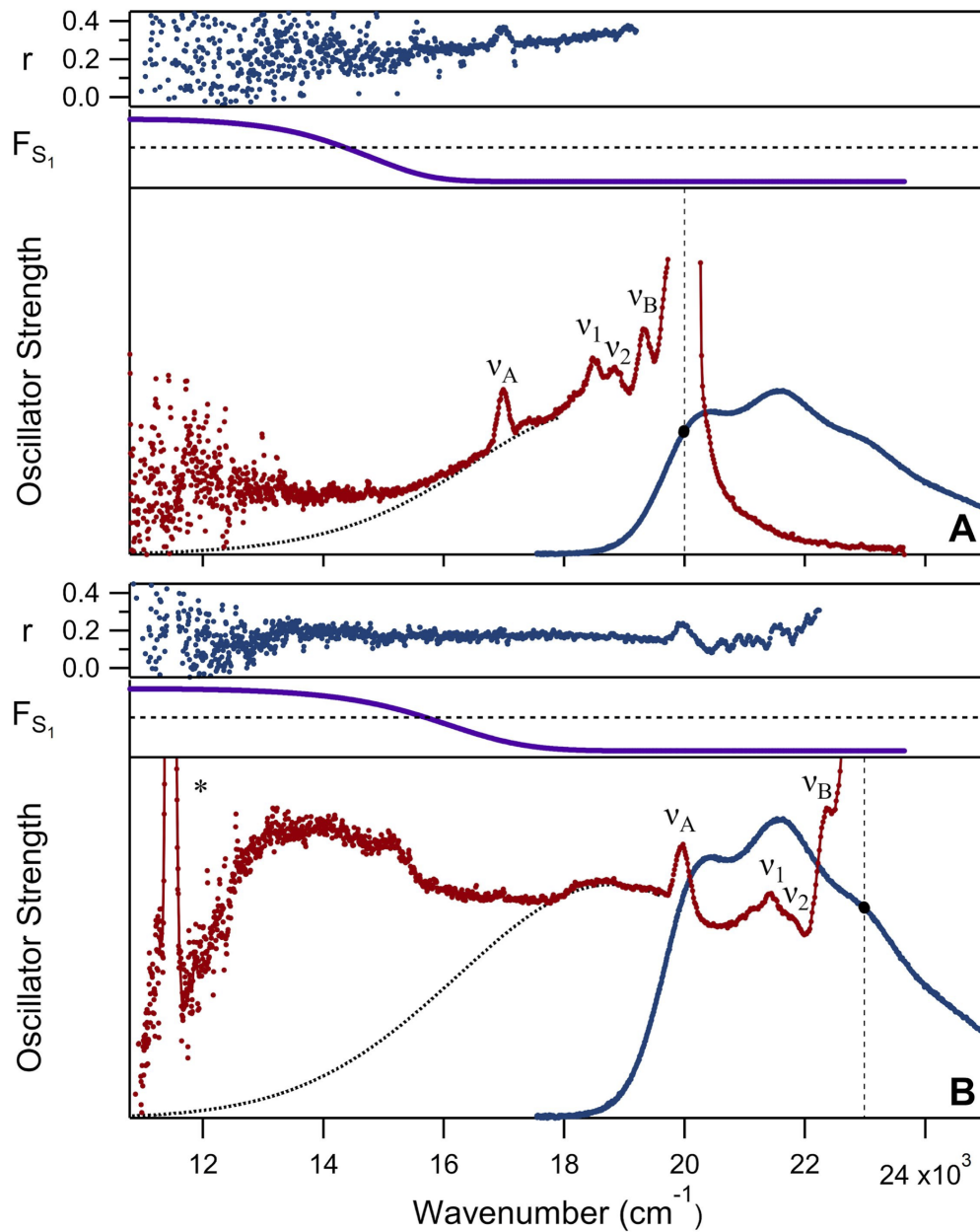


Figure 3.3. Fluorescence oscillator strength and anisotropy (r) spectra for β -carotene in chloroform at 293 K: (a) with excitation at 500 nm ($20,000\text{ cm}^{-1}$); (b) with excitation at 435 nm ($23,000\text{ cm}^{-1}$). Other details are as indicated in the caption to Figure 3.2, including plotting the fluorescence oscillator strength spectra with the same intensity scaling in panels (a) and (b). The positions of resonance Raman peaks from β -carotene ($\nu_1 = 1517\text{ cm}^{-1}$ and $\nu_2 = 1157\text{ cm}^{-1}$)¹³⁴ and non-resonance Raman peaks from the chloroform solvent ($\nu_A = 2966\text{ cm}^{-1}$ and $\nu_B = 732\text{ cm}^{-1}$)¹⁴² are marked.

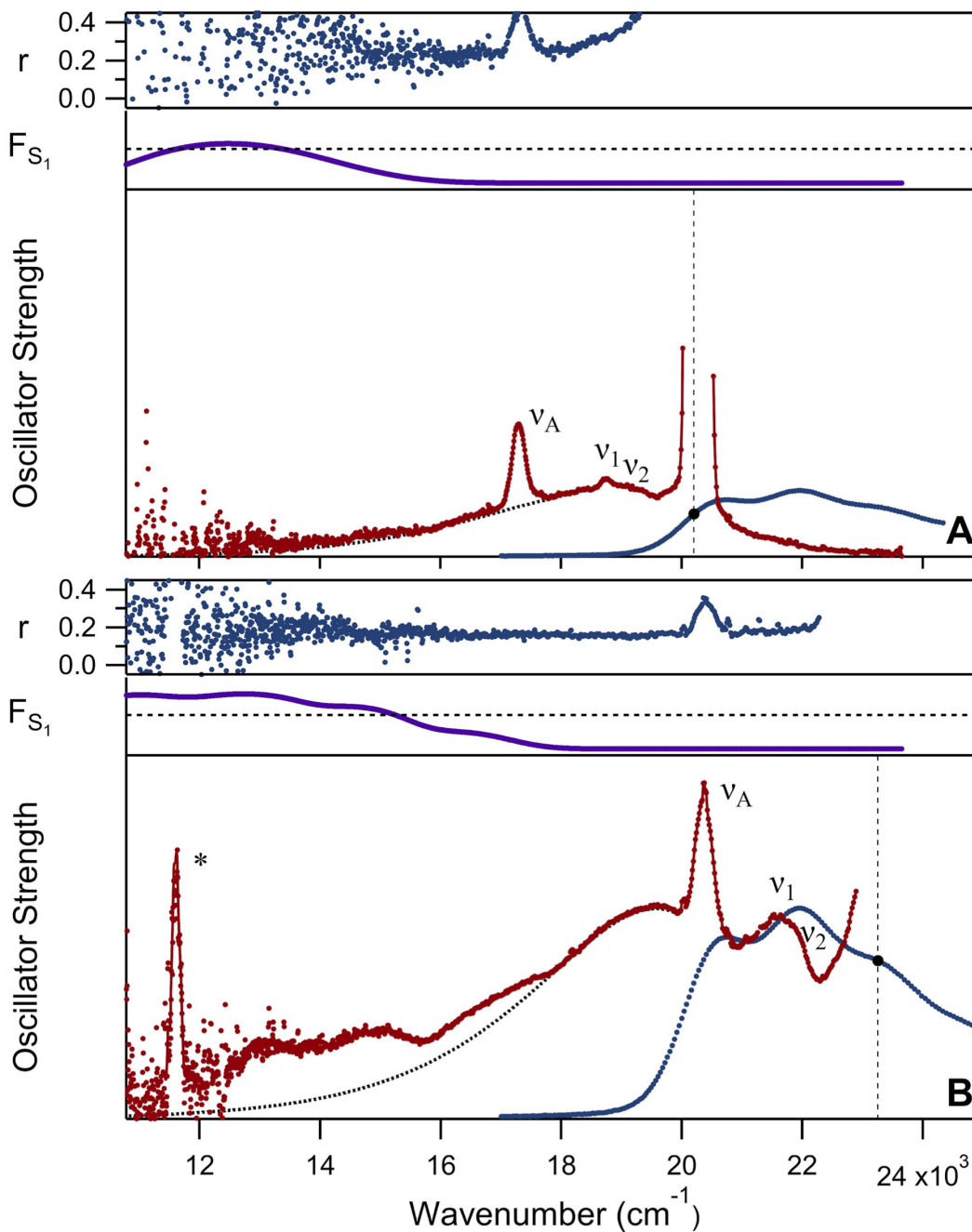


Figure 3.4. Fluorescence oscillator strength and anisotropy (r) spectra for β -carotene in 2-MTHF at 293 K: (a) with excitation at 495 nm ($20,200 \text{ cm}^{-1}$); (b) with excitation at 430 nm ($23,250 \text{ cm}^{-1}$). Other details are as indicated in the caption to Figure 3.2, including plotting the fluorescence oscillator strength spectra with the same intensity scaling in panels (a) and (b). The positions of resonance Raman peaks from β -carotene ($\nu_1 = 1517 \text{ cm}^{-1}$ and $\nu_2 = 1157 \text{ cm}^{-1}$)¹³⁴ and for a non-resonance Raman peak from the 2-MTHF solvent ($\nu_A = 2915 \text{ cm}^{-1}$)¹⁴³ are marked.

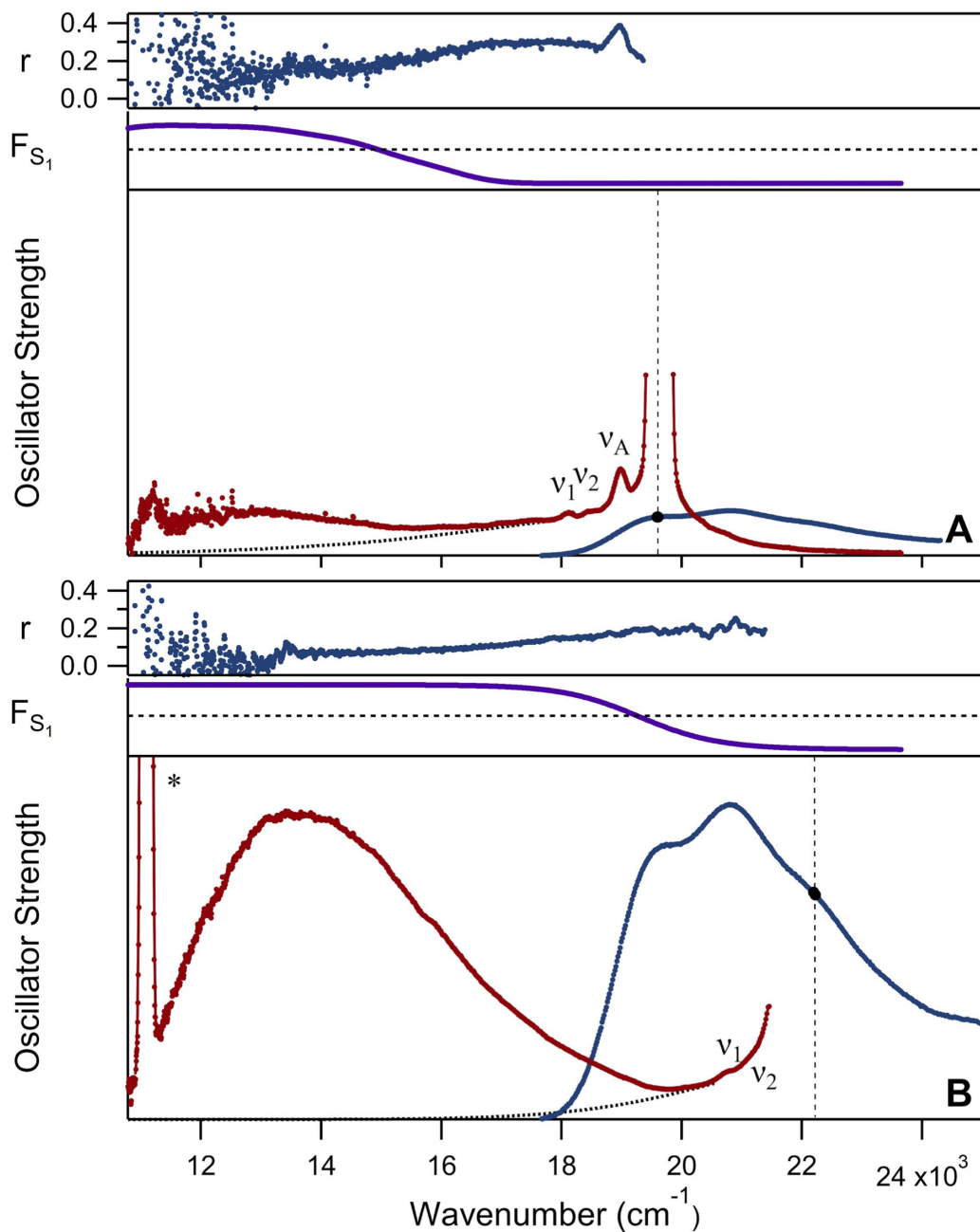


Figure 3.5. Fluorescence oscillator strength and anisotropy (r) spectra for β -carotene in carbon disulfide at 293 K: (a) with excitation at 510 nm ($19,600\text{ cm}^{-1}$); (b) with excitation at 450 nm ($22,200\text{ cm}^{-1}$). Other details are as indicated in the caption to Figure 3.2, including plotting the fluorescence oscillator strength spectra with the same intensity scaling in panels (a) and (b). The positions of resonance Raman peaks from β -carotene ($\nu_1 = 1517\text{ cm}^{-1}$ and $\nu_2 = 1157\text{ cm}^{-1}$)¹³⁴ and for a non-resonance Raman peak from the CS_2 solvent ($\nu_A = 658\text{ cm}^{-1}$)¹⁴⁴ are marked.

Table 3.1. Fluorescence quantum yield and anisotropy parameters for β -carotene

Solvent	λ_{exc}	$\Phi_{\text{F}, \text{S}2}^a$	$\Phi_{\text{F}, \text{S}1}^a$	$r_{\text{S}2}^b$	$\theta_{\text{S}2}^c$	$r_{\text{S}1}^b$	$\theta_{\text{S}1}^c$
<i>n</i> -Hexane	430 nm	1.7×10^{-6}	6.8×10^{-7}	0.28 ± 0.01	26.6 $\pm 2.4^\circ$	0.05 ± 0.04	49.8 $\pm 5.8^\circ$
	490 nm	1.1×10^{-6}	3.2×10^{-8}	0.35 ± 0.04	16.8 $\pm 15.4^\circ$	---	---
Carbon Disulfide	450 nm	5.7×10^{-6}	1.7×10^{-5}	0.20 ± 0.02	35.3 $\pm 4.1^\circ$	0.07 ± 0.01	47.9 $\pm 1.9^\circ$
	510 nm	1.9×10^{-6}	7.0×10^{-7}	0.29 ± 0.01	25.4 $\pm 2.5^\circ$	0.14 ± 0.05	41.2 $\pm 9.7^\circ$
Chloroform	435 nm	3.8×10^{-6}	8.6×10^{-7}	0.16 ± 0.01	39.2 $\pm 1.9^\circ$	0.14 ± 0.11	41.2 $\pm 21.7^\circ$
	500 nm	1.1×10^{-6}	1.2×10^{-7}	0.25 ± 0.02	30.0 $\pm 4.4^\circ$	0.24 ± 0.16	31.1 $\pm 46.9^\circ$
2-MTHF	430 nm	2.0×10^{-6}	4.7×10^{-7}	0.16 ± 0.01	39.2 $\pm 1.9^\circ$	0.17 ± 0.10	38.3 $\pm 21.1^\circ$
	495 nm	7.3×10^{-7}	2.6×10^{-8}	0.24 ± 0.03	31.1 $\pm 6.5^\circ$	---	---

^aAbsolute fluorescence quantum yield

^bMinimum fluorescence anisotropy at long wavelengths for the indicated emission band (Figures 3.3, 3.5, 3.7, and 3.9).

^cRotation angle of the fluorescence emission TDM from the photoselected TDM for the absorption transition, from equation 2.

3.4.4. Temperature dependence of the fluorescence from β -carotene

An alternative explanation for the fluorescence anisotropy results is that the isoprenoid backbone of β -carotene undergoes out-of-plane distortions that rotate the emission TDM while still evolving on the S_2 potential energy surface during the <150 fs emission timescale.^{4,43} The excitation wavelength dependence of the fluorescence anisotropy would then indicate that passage over a low activation barrier from the Franck–Condon region of the S_2 state's potential energy surface, as depicted in Figure 1.1, is required to access to the potential energy gradient with respect to out-of-plane motions. Further, the lower anisotropy observed in the S_1 fluorescence band would be explained by an additional internal rotation of the emission TDM that follows passage through the CI from the S_2 state.

A test of the possible assignments for the fluorescence anisotropy of β -carotene can be made by performing a series of fluorescence observations as a function of temperature. At low temperatures, a high fluorescence anisotropy would be expected if the friction from the surrounding frozen solvent inhibits large amplitude out-of-plane motions from the Franck–Condon S_2 state structure. On the other hand, if tuning of the excitation wavelength to shorter wavelengths changes the fluorescence line shape or anisotropy because of coming into resonance with a low lying B state, the alternative assignment suggested above, the same anisotropy value would be anticipated at low and higher temperatures. Lowering the temperature would then be expected mainly to result in a sharpening of the fluorescence line shape without affecting the anisotropy.

Of the four solvents used in this study, we chose 2-MTHF for a variable temperature study because it forms high quality clear glasses of carotenoid solutions at cryogenic temperatures,¹⁴¹ which would be favored to lower the background light scattering that might obscure the weak

fluorescence signals anticipated from β -carotene. A fixed excitation wavelength was used, 430 nm, which obtains at room temperature the signal shown in Figure 3.4b featuring a low anisotropy value, 0.16, in the S_2 and S_1 bands. The absorption and fluorescence spectra were recorded sequentially at a given temperature with the β -carotene sample in 2-MTHF held in a liquid nitrogen cryostat (80–200 K) or in a Peltier-effect temperature controller (258–296 K). We were unable to operate the liquid nitrogen cryostat reliably at higher temperatures than 200 K, so no spectra are available over the intermediate 200–258 K range. Figure 3.6 shows the absorption and fluorescence spectra from β -carotene in 2-MTHF at four temperatures over the 80–258 K range. The four panels present the fluorescence oscillator strength and anisotropy spectra in these solvents in the same manner used above; the full set of wavelength spectra over the 80–296 K range are presented in the Supporting Information.

As the temperature is lowered, the absorption spectrum from β -carotene in 2-MTHF shifts with respect to the room temperature spectrum to lower wavenumbers and develops a sharpened vibronic structure. The line shape function would be expected to narrow as the temperature is lowered, but simulations using the MBO model¹⁰⁰ of the absorption spectra at 80 K and 296K (shown in the Supporting Information) also indicate that the total solvation reorganization energy increases by about 25% at 80 K compared to that at room temperature. This effect can be attributed to a constriction of the solvent cavity around the β -carotene chromophore in the ground state as the temperature decreases in the dark prior to illumination. The shift of the absorption spectrum to the red as the temperature is lowered arises from the temperature dependence of the solvent polarizability.^{8,16,145,146}

The main result from Figure 3.6, however, is that the integrated oscillator strength of the fluorescence emission from β -carotene with 430 nm excitation markedly increases as the

temperature is lowered due to a new contribution to the emission spectrum from a short-lived spectral "intermediate" along the S_2 to S_1 nonradiative decay pathway. The fluorescence oscillator strength spectra are shown with absolute scaling in Figure 3.6 to make clear how much stronger the emission is at 80 K; the quantum yield determined from the integrated oscillator strength is 78 times larger at 80 K, 1.5×10^{-4} , than that at room temperature, 2.0×10^{-6} . The emission spectrum over the 80–200 K range (Figure 3.6a–c) is dominated by a very broad line shape centered roughly at $16,000 \text{ cm}^{-1}$ (625 nm), well to the red of that observed from S_2 at higher temperatures (Figure 3.6d or Figure 3.4b). As the temperature is raised above 80 K, the fluorescence spectrum maintains its broad lineshape albeit with a small red shift as it decreases in intensity, essentially disappearing above 200 K to reveal the underlying much weaker S_2 and S_1 emission bands characteristic of the high temperature emission spectrum.

The broad emission lineshape observed over the 80–200 K range very likely corresponds to formation of a distorted intermediate moving on the out-of-plane potential energy gradient linking the Franck–Condon S_2 state to the CI with the S_1 state (Figure 1.1). The lineshape is comparable to that determined as the instantaneous species associated difference (SADS) spectrum observed by de Weerd et al.⁴⁸ in a global target analysis of their femtosecond pump–continuum probe spectra with β -carotene at room temperature in three solvents. These signals should not be regarded as arising from a conventional intermediate spectroscopic state; the breadth of the fluorescence signals observed in Figures 3.6ac ($\sim 8000 \text{ cm}^{-1}$ at 80 K) would correspond to uncertainty broadening of a state with an infinitesimal lifetime, $\sim 660 \text{ as}$, which would preclude its detection via fluorescence. Thus, the overall breadth of the fluorescence (and SE) signals from β -carotene reflect the integral of narrower lineshapes from molecules moving rapidly on the S_2 out-of-plane gradient over the $<150 \text{ fs}$ timescale. As the temperature is raised

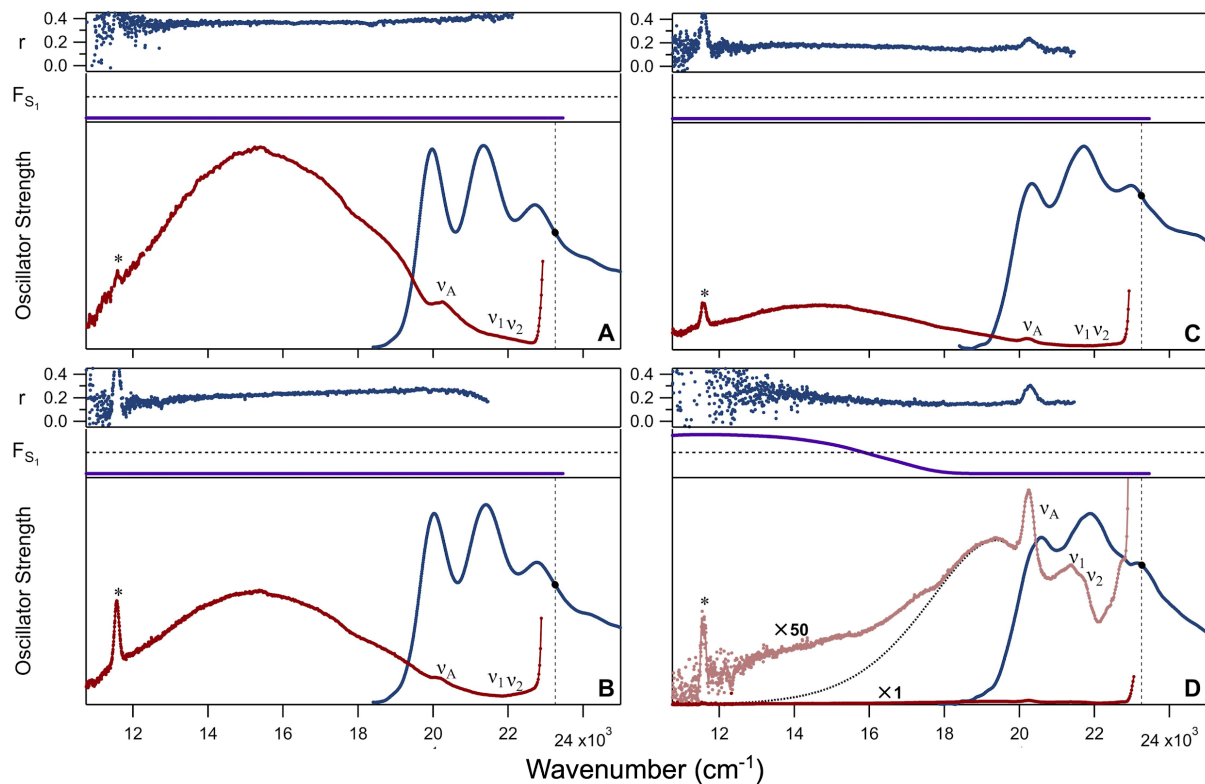


Figure 3.6. Absorption (blue) and fluorescence (red) oscillator strength and anisotropy (r) spectra for β -carotene in 2-MTHF with excitation at 430 nm ($23,250 \text{ cm}^{-1}$) at: (a) 80 K; (b) 120 K; (c) 200 K; and (d) 258 K. Other details are as indicated in the caption to Figure 3.2, including plotting the fluorescence oscillator strength spectra with the same intensity scaling in all four panels. In (d) the fluorescence oscillator strength is also replotted at $\times 50$ scaling. The positions of resonance Raman peaks from β -carotene ($\nu_1 = 1517 \text{ cm}^{-1}$ and $\nu_2 = 1157 \text{ cm}^{-1}$)¹³⁴ and for a non-resonance Raman peak from the 2-MTHF solvent ($\nu_A = 2915 \text{ cm}^{-1}$)¹⁴³ are marked.

over the 80–258 K range for the example spectra in Figure 3.6, the solvent viscosity (and the resulting friction) decreases over many orders of magnitude.¹⁴⁷ Above 200 K it is evident that the time spent by a given molecule on the out-of-plane gradient is very short indeed. Very few fluorescence photons are detected during progress to the CI with the S_1 state, allowing the high temperature S_2 and S_1 emission bands to be observed.

The high fluorescence anisotropy value detected at 80 K, 0.36, (Figure 3.6a) indicates that the isoprenoid backbone of β -carotene is still constrained at 80 K to point roughly along the direction of the equilibrium ground state structure even though the emission spectrum reports the presence of a distorted intermediate. This finding strongly suggests that concerted out-of-plane distortions of more than one bond occur along the isoprenoid backbone of β -carotene when large volumes of motion are constrained by the frozen solvent cavity. The "bicycle pedal"¹⁴⁸ and "hula-twist" mechanisms¹⁴⁹ for the retinal PSBs in rhodopsin or bacteriorhodopsin are well discussed examples of out-of-plane pathways leading to fully photoisomerized structures incorporating torsions of more than one bond along a polyene's length. These structures are termed volume conserving because they can occur from initially all-*trans* configurations despite being confined by the frozen solvent cavity at low temperature.¹⁵⁰ Further, assumption of these structures would not be reported by a large internal rotation of the emission TDM since a large sweep of half of the isoprenoid backbone of β -carotene would not be required as it would for a single-bond distortion.

At higher temperatures, the melting 2-MTHF solvent apparently allows the isoprenoid backbone of β -carotene to lower its conformational potential energy further by relaxing further out-of-plane at a single point along its length. This process results in lower anisotropy values (Figure 3.6bc). Figure 3.7a shows that the minimum anisotropy smoothly decreases over the

80–200 K range to level off at the 0.16 value observed in the S_2 and S_1 emission regions in 2-MTHF at high temperatures. Although the confidence intervals are large and overlap extensively, the anisotropy measured for the S_1 emission exhibits an decreasing trend as the temperature is raised over the 258–296 K range. The lifetime of the S_1 state is ~ 10 ps,^{22,43,137,138} somewhat longer than the 0.5–2 ps timescale associated for vibrational cooling in carotenoids,^{141,151} so the emission spectrum from S_1 would be expected to be that from an ensemble nearly at thermal equilibrium with the surrounding medium.

An estimate for the effective activation energy barrier that constrains the motion of the S_2 molecules on the out-of-plane gradient leading to the CI seam with the S_1 state is obtained from the slope $-E_a/RT$ of an Arrhenius plot (Figure 3.7b), plotted in terms of the ratio of nonradiative and radiative rates of decay, $k_{nr}/k_r = \Phi_F^{-1} - 1$.^{152,153} Over the 80–200 K range, a linear trend with respect to $1/T$ is observed. The slope corresponds to an activation energy of 140 cm^{-1} , which can be identified as a librational mode of the 2-MTHF solvent medium. Almost exactly the same activation energy was observed in fluorescence anisotropy decay measurements in 2-MTHF with a range of fluorescent probes.¹⁵⁴ To be clear, in this picture the barrier between the Franck–Condon region and the out-of-plane gradient of the S_2 potential energy surface has been already crossed by the molecules that emit the broad low-temperature fluorescence spectrum shown in Figure 3.6a–c.

At higher temperatures, the larger slope of the Arrhenius plot determined from the integrated oscillator strength for the high-temperature S_2 and S_1 emission bands indicates an effective activation energy for nonradiative decay, 850 cm^{-1} . This frequency is in the range associated with hydrogen-out-of-plane deformation modes in polyenes.^{155,156} The simple dynamical picture used in the thinking here is that effectively an exchange of vibrational quanta with the surroundings

promotes passage of the β -carotene molecules from the S_2 state to the S_1 state through a CI seam between the two potential energy surfaces, so the quanta of the key promoting modes contributes to the activation energies.

The coupling of the temperature dependence of the fluorescence quantum yield and anisotropy observed here for β -carotene in 2-MTHF has not been reported previously, to our knowledge, but Andersson et al.¹⁵² observed a comparable temperature dependence for the quantum yield of fluorescence from the triene analog of β -carotene, mini-3. The mini-carotenes exhibit a fluorescence spectrum with a more pronounced "dual" character, with bands from the S_2 and S_1 states both apparent.¹⁵⁷ The shortest of these, mini-3, having only a single/double bond backbone between the two β -cyclohexane rings, absorbs in the 250 nm region of the UV and emits in the 360 nm region. The fluorescence quantum yield of mini-3 was observed to follow an Arrhenius dependence with an activation energy of 610 cm^{-1} ; over the 77–110 K temperature range, the quantum yield decreases from 0.61 to 0.04. Andersson et al. discuss this trend in terms of a nonradiative decay mechanism promoted by out-of-plane torsional motions. The fluorescence anisotropy measured at 77 K is high, 0.39, but unfortunately no measurements of the anisotropy at higher temperatures were reported, most likely because the fluorescence quantum yield decreases to very low values in liquid media, rendering it effectively "nonfluorescent."¹⁵² In mini-3, the activation energy barrier (Figure 1.1) for access from the Franck–Condon region of the S_2 potential energy surface to the out-of-plane gradient would be expected to be small or nonexistent compared to that in β -carotene. In comparison, as noted above, the temperature dependence noted for β -carotene in Figures 3.6 and 3.7 was observed with excitation at 430 nm, well above the wavenumber of the 0–0 transition.

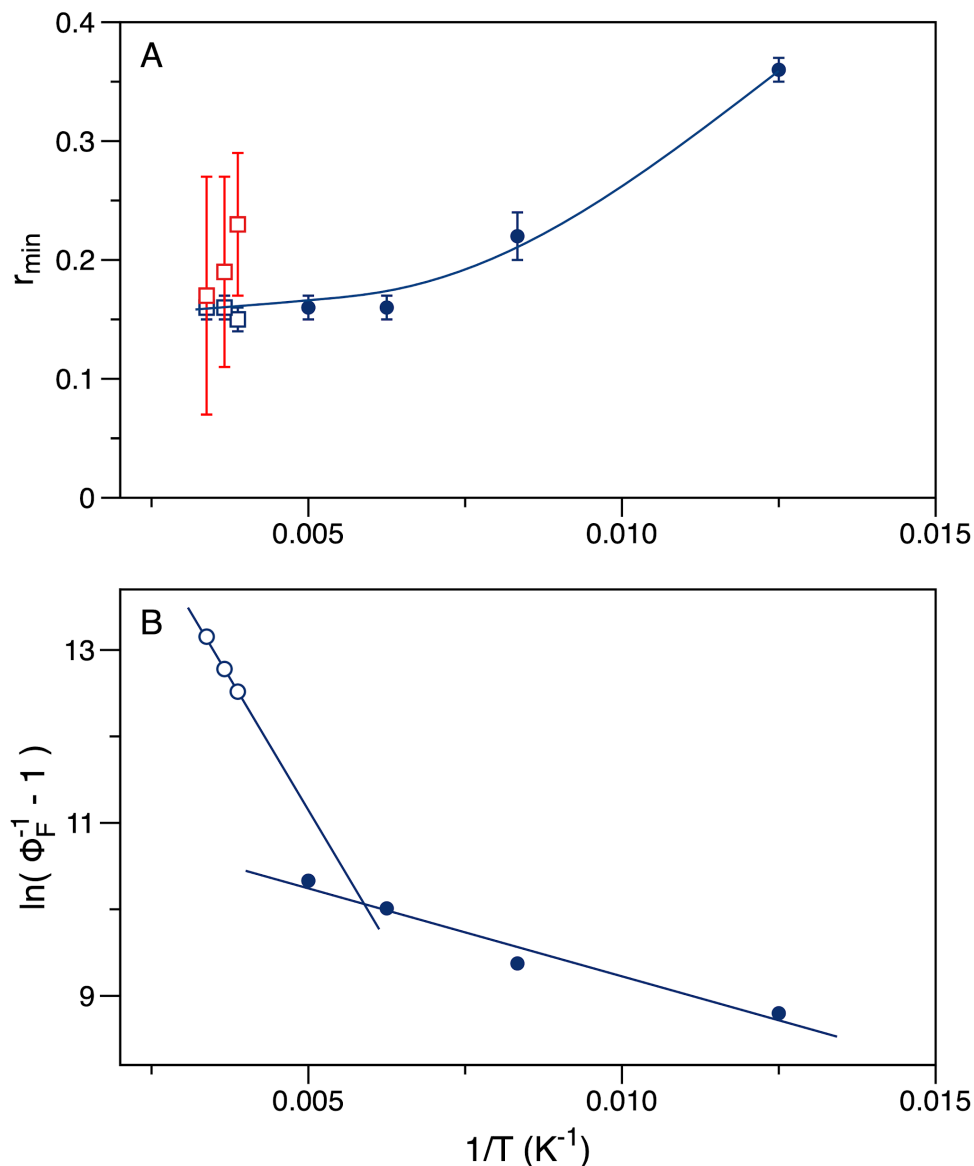


Figure 3.7. Comparison of the temperature dependences of (a) the minimum fluorescence anisotropy and (b) the quantum yield of fluorescence for β -carotene in 2-MTHF solvent with excitation at 430 nm. In (a), the trend of the fluorescence anisotropy measured for the emission from the spectral intermediate (Figure 3.6a–c) observed over the 80–200 K range (\bullet) is extended to compare with the anisotropy measured over the 258–296 K range for the S_2 (\square) and S_1 (\square) bands. Error bars report the \pm standard deviations over the sampled spectral regions. In the Arrhenius-style plot shown in (b), $E_a = 140 \pm 20 \text{ cm}^{-1}$ for 80–200 K (\bullet) and $E_a = 850 \pm 5 \text{ cm}^{-1}$ for 258–296 K (\circ).

3.4.5. DFT Calculations*

To explore how internal out-of-plane structural deformations of the isoprenoid backbone of β -carotene in the S_2 state might cause the emission TDM to rotate, producing the experimentally observed low minimum fluorescence anisotropies (Table 3.1), we computed the electronic structures of a set of torsionally distorted conformers starting from the all-trans structure. As the simplest case, we consider here a single torsional coordinate for the initial excited state relaxation away from the Franck–Condon region of the S_2 potential energy surface. Of course, the possibility that rotations of more than one coordinate of the isoprenoid backbone contribute to the observed rotation of the TDM should not be dismissed arbitrarily. As noted above, concerted or sequential torsions of more than one C–C bond have been discussed, in particular for the photochemistry of retinal PSBs in rhodopsin and bacteriorhodopsin.¹⁵⁰ Further, calculations by Hynes and coworkers¹⁵⁸ on retinal PSB models indicate that the torsional and pyramidal coordinates are strongly coupled, so the out-of-plane distortions observed in β -carotene would very likely involve simultaneous displacements along both coordinates.

Potential energy surface scans in the electronic ground state, S_0 , were conducted with respect to torsion of each of the labeled bonds numbered in Figure 3.8a, with the C–C=C–C dihedral angle varied from 180° for the nominally planar, all-trans structure to 90° . This procedure allows a smooth relaxation of the internal coordinates to accompany the fixed torsional distortion. The computed transition density isosurfaces and the $S_0 \rightarrow S_2$ absorption TDM vectors for the particular example of rotation around the C_{15} – $C_{15'}$ double bond are shown in Figure 3.8b. The

* The calculations presented here were performed by Professor José A. Gascón and coworkers at the University of Connecticut.

colored isosurfaces show how the π -electron density increases or decreases upon optical excitation. The TDM vectors are referenced in each conformation with respect to the center of mass. Figure 3.8c summarizes how the orientation of the TDM depends on which C–C bond in the isoprenoid backbone is twisted to assume a 90° conformation. The rotation angle is determined relative to the orientation of the TDM for the all-trans configuration. This angle would be expected to be comparable to that for the vertical fluorescence emission transition from a distorted S_2 structure to the ground state. Twisting of bonds 14-15, 15-15', and 15'-14' to the 90° conformation rotates the TDM by $28\text{--}35^\circ$, with the largest rotation arising from twisting the central $C_{15}\text{--}C_{15'}$ bond.

The results shown in Figure 3.8c for rotations of the absorption TDM due to torsions of the isoprenoid backbone of β -carotene in the ground state are recapitulated by relaxed scans of the S_2 potential energy surface of a truncated version of β -carotene in which the β -ionone rings have been replaced by hydrogen atoms (Figure 3.8a). This truncation lessens the time and considerable expense required for excited-state optimizations; the π -electron density is mostly resident on this section of the β -carotene structure. Figure 3.8d compares the calculated rotations for the $S_0 \rightarrow S_2$ absorption and $S_2 \rightarrow S_0$ emission TDMs with respect to torsions of the $C_{15}\text{--}C_{15'}$ bond for the truncated model. The TDM rotations were found to agree within 2° . This agreement justifies the use of ground state conformers for the TDM rotation analysis for the full β -carotene structure (Figure 3.8c). The close agreement between these two calculations demonstrates that 90° torsional distortions of a single C–C bond near the center of the isoprenoid backbone are remarkably consistent with the 39° TDM rotations determined by the fluorescence anisotropy values of 0.16 for the S_2 band in the polar solvents, chloroform and 2-MTHF (Table 3.1). The

barrier for torsions would be expected to be the lowest near the center of the isoprenoid backbone, where the BLA amplitude is the smallest along the chain.²⁰

It is important to clearly state the assumptions we are making to model the hypothesised torsional conformations. The purpose of the scan of the torsional angles on the S_0 and S_2 surfaces, the latter for the truncated model, is strictly to make a correlation between the structure and the direction of the vertical transition dipole moment for transitions between the two surfaces. This work is intended to extend the general conclusion^{16,133} that the transition dipole moments of linear polyenes point down the isoprenoid backbone. To our knowledge, there have not been any reports of electronic structure calculations of the TDM directions in twisted conformers or even in *cis* configurations. The structures at each torsional angle should be considered local minima because the energy was minimized at each stated torsional conformation, primarily to avoid steric clashes, but a global minimum energy path was not sought given that we held only one torsion fixed during the energy minimization. Further, we have not attempted calculations of the TDM direction in the S_1 state because it is well known that TDDFT methods should not be used to model states involving a large component of double excitations. There is no reason to suggest, however, that the S_1 state's TDM direction should point in a different direction from that determined for the S_0 or S_2 states.

A physical explanation for the larger rotations of the TDM observed in the nonpolar solvents, 48–50°, requires the displacement of an additional coordinate of the isoprenoid backbone of β -carotene during the fluorescence emission timescale. Of particular interest is the possibility that a pyramidal distortion converts the diradical electron configuration of a twisted bond to the lone-pair configuration consistent with a full ICT.^{50,51} The pyramidal structure corresponds to a candidate for a CI of the S_2 state with the S_1 state. Although determination of a true CI on the S_2

surface is beyond the scope of the present work (and beyond the capabilities of TD-DFT for such a large system), we constructed an *ad hoc* model for the β -carotene CI structure using a template constructed with the internal coordinates of ethylene at the CI determined using spin-flip TD-DFT by Minezawa and Gordon.¹⁵⁹ Specifically, the ethylene CI's structure was superimposed with our 90° rotated structure, as obtained via the relaxed scan discussed above. After that, the four dihedral angles of the C₁₅–C_{15'} bond were manually adjusted to visually maximize the overlap between the C₁₅–C_{15'} adjacent atoms and those of the ethylene CI. The structure was then relaxed in the ground state but keeping the dihedral angles of the C₁₅–C_{15'} bond fixed to minimize steric interactions.

Figure 3.9 shows the superposition of three relevant conformations: the all-*trans* structure, the 90° rotated structure used in Figure 3.8b, which gives rise to a 35° rotation of the TDM, and the pyramidal structure resembling the ethylene CI. For the latter structure, the calculated TDM rotation is 47°. This result is remarkably similar to the 48–50° rotation angle observed in the fluorescence anisotropy measurements for the S₁ state in the nonpolar solvents (Table 3.1).

Figure 3.10 shows how the emission TDM vectors for the Franck–Condon S₂ state and those of the 90° twisted and pyramidal S₂ conformations are oriented with respect to the molecular frame of the ground-state structure of β -carotene. The ground-state all-*trans* structure is shown in two orientations, with the point-of-view directed in the plane and from above. The TDM vectors are drawn with their origins placed at the center-of-mass, which coincides with the midpoint C₁₅–C_{15'} bond.

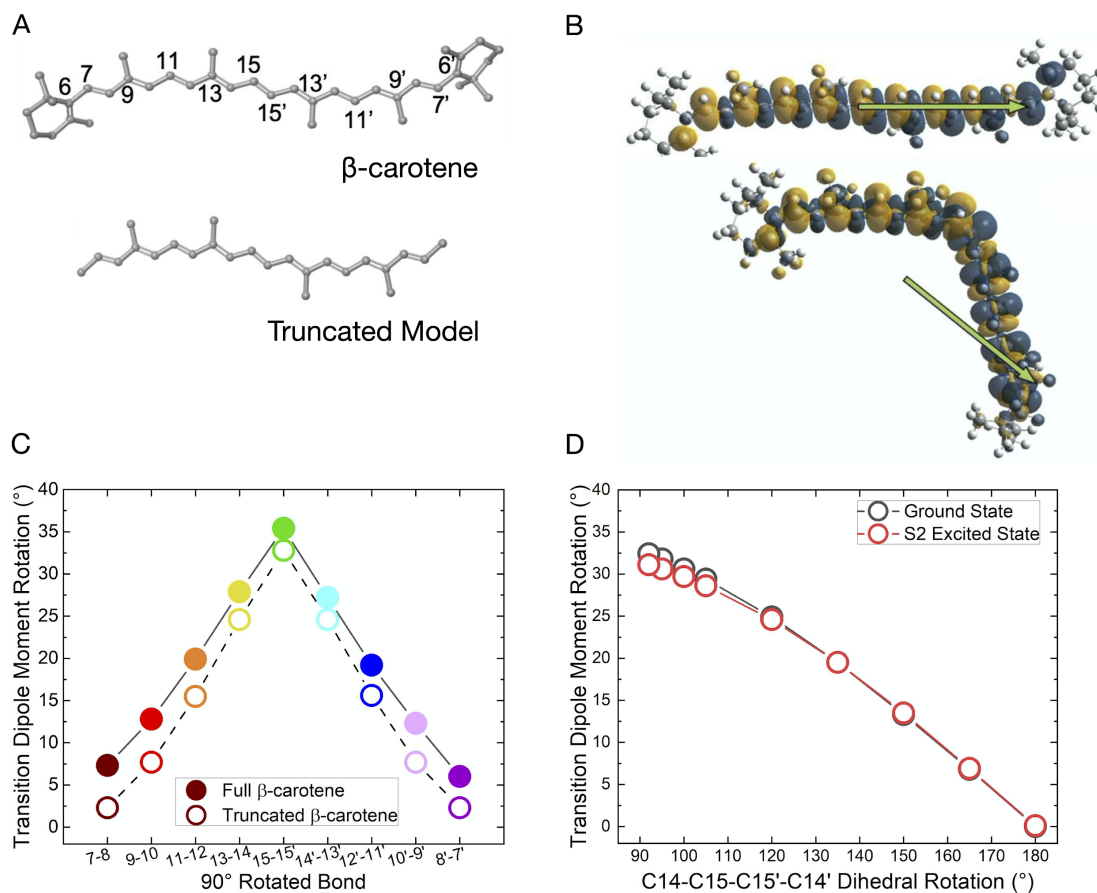


Figure 3.8. (a) Minimum energy structure of β -carotene and of a truncated model, with a numbering scheme indicated (as also used in Scheme 1) for the carbon atoms in the isoprenoid backbone. (b) Optical transition densities for the $S_0 \rightarrow S_2$ absorption transition for the all-*trans* structure and for the C_{15} - $C_{15'}$ 90° -twisted structure. Orange/blue orbital colors denote an instantaneous gain or loss of electron density, respectively, upon excitation. Green arrows indicate the direction of the TDM with the vector origins drawn at the center of mass. (c) Calculated TDM rotations with respect to the all-*trans* structure as a function of the choice of the bond undergoing a 90° torsion for the $S_0 \rightarrow S_2$ absorption TDM, the latter for the truncated model. (d) Calculated rotations for the $S_0 \rightarrow S_2$ absorption and $S_2 \rightarrow S_0$ emission TDMs with respect to torsions of the C_{15} - $C_{15'}$ bond of β -carotene, the latter for the truncated model.

The TDM for the Franck–Condon S_2 state is rotated by 8° with respect to the molecular frame axis, which is chosen here as the vector connecting the C_6 and C_6' atoms on the opposite ends of the isoprenoid backbone. In comparison, Birge et al.¹¹⁶ obtained an estimate of 15° for the orientation of the TDM compared to the molecular frame axis for a conjugated polyene with $N = 11$ conjugated polyene double bonds with the methyl groups included along the backbone, 12.6° if the methyl groups were not included. The effective conjugation length for β -carotene is shorter than this, but similar values were obtained for $N = 8$ – 15 . Similarly, Dolan et al.¹¹⁷ used linear dichroism measurements in squeezed polyacrylamide gels to determine that the absorption TDM is rotated 9.1° from the molecular frame axis in the "corkscrew" ground state conformation of rhodopin glucoside in LH2 from *Rhodospseudomonas acidophila* strain 10050.

Table 3.2 compares the permanent dipole moments in the ground and S_2 states and the rotations of the TDMs for the three structures shown in Figure 3.9. Photoexcitation to the S_2 state results in only a small increase in the non-zero permanent dipole moment exhibited by the ground state structure, which is not perfectly C_2 symmetric. The 90° twisted structure has a larger dipole moment, 1.6 D, which implies a significant polar character. A substantially larger dipole moment is determined for the pyramidal structure, 8.3 D, indicating ICT across the C_{15} - C_{15}' bond and delocalization on either side of it. These results are consistent with the suggestion that evolution on the S_2 surface should be accompanied by a large increase in the solvent friction as the structure nears the CI with the S_1 state.

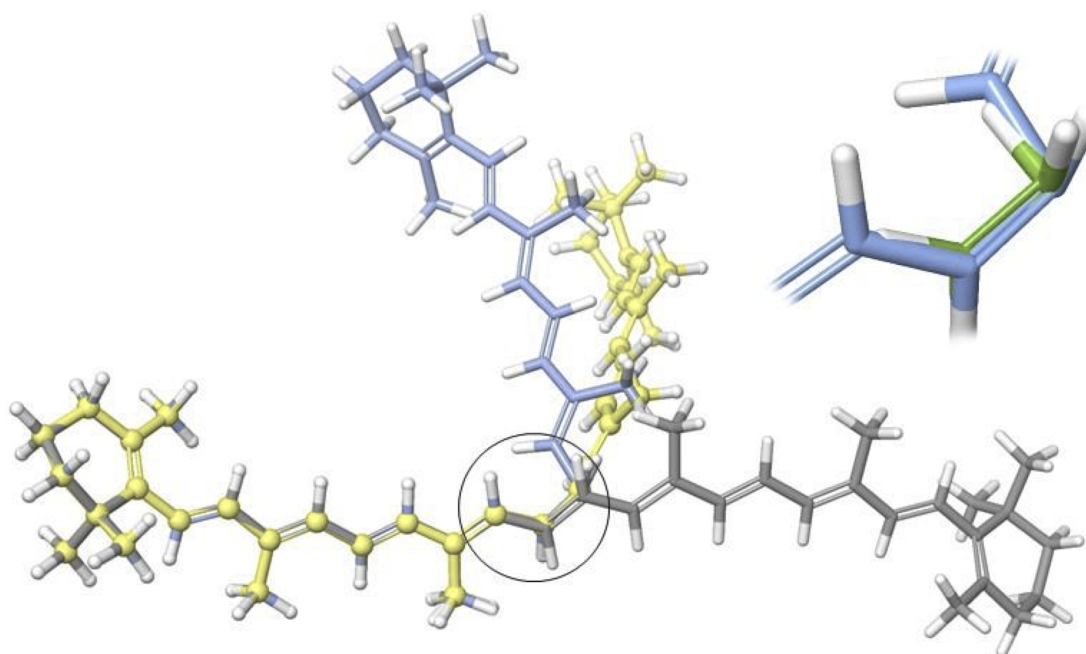


Figure 3.9. Modeled structures representing the Franck-Condon S_2 structure (gray), the 90° twisted conformer (yellow), and a conformer with a pyramidal distortion (light blue). The inset is a zoomed-in view of the circled region, which shows the modeled β -carotene pyramidal structure superimposed with the pyramidal structure of the CI of ethylene.¹⁵⁹

Table 3.2. Permanent dipole moments and TDM rotations for the calculated β -carotene S_2 structures

Structure	Dipole Moment (D)	TDM rotation ^a
S_0	0.1 D	—
S_2 (Franck-Condon)	0.2 D	0° (reference)
S_2 90-twisted	1.6 D	35°
S_2 pyramidal	8.3 D	47°

^aDeviation angle from the direction of the vertical S_2 TDM.

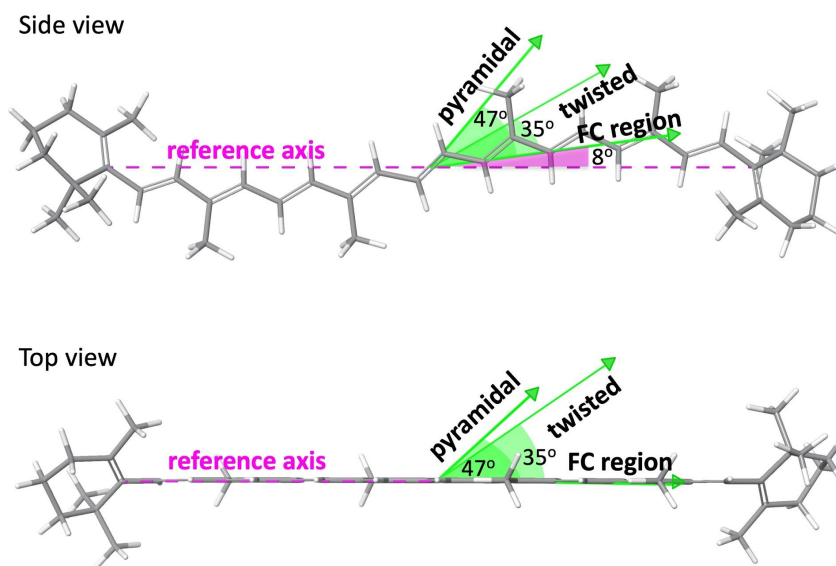


Figure 3.10. Orientations of the emission TDM vectors for the Franck–Condon S_2 state and those of the 90° twisted and pyramidal S_2 conformations with respect to the ground-state structure of β -carotene. The reference axis is the C_6 – $C_{6'}$ vector.

3.5. Discussion

The results presented above suggest a new picture for the photophysical and photochemical properties of carotenoids arising from optical preparation of the bright S_2 state. As demonstrated here with β -carotene in several aprotic solvents, fluorescence emission is observed from two distinct groups of excited-state molecules depending on the excitation wavelength. A fraction is retained by a low activation barrier near the Franck–Condon geometry (Figure 1.1); these molecules are optically prepared by absorption transitions near to the 0–0 transition. The fluorescence spectrum from these S_2 state molecules is roughly mirror symmetric with respect to the absorption spectrum, and the fluorescence anisotropy is at least 0.35, near to the 0.4 value expected for molecules retaining the essentially planar all-trans structure photoselected from the ground state ensemble. An example of a fluorescence spectrum predominantly from these molecules is that observed from β -carotene in hexane with 490 nm excitation (Figures 3.1a and 3.2a).

As the excitation wavelength is tuned to the blue over the $\sim 3000\text{ cm}^{-1}$ range spanned in the vibronic structure from the 0–0 transition to the 0–3 transition, an increasing fraction of S_2 state molecules are able to pass over an activation barrier dividing the planar and out-of-plane distorted regions of the S_2 potential energy surface. This part of the excited-state ensemble contributes at high temperatures to a broadening of the red tail of the S_2 spectrum and to a more prominent and blue-shifted S_1 emission band compared to that observed upon nonradiative decay from the planar molecules retained by the barrier. In carbon disulfide, chloroform, and 2-MTHF, the fraction of S_2 molecules crossing over the activation barrier is significant even at the longest excitation wavelengths used in the present experiments given the observation of fluorescence

anisotropies < 0.3 in the S_2 emission band (Table 3.1). This finding suggests that barrier height is significantly lower in these solvents than in hexane.

The work presented here contributes the key connection that the near-IR portion of the emission from S_2 and the enhanced emission from S_1 observed with blue excitation has a low fluorescence anisotropy. This finding indicates that passage over the activation barrier is followed by evolution on a steep gradient on the S_2 state potential energy surface with respect to the out-of-plane coordinates of the isoprenoid backbone (Figure 1.1), producing emission that is progressively red shifted from the mirror-symmetric S_2 emission. Over the 80–200 K range, we observed a broad emission band with an enhanced emission quantum yield and a temperature dependent anisotropy that arises from a dynamic intermediate, perhaps S_x or its successor evolving on the out-of-plane gradient. Progress along the out-of-plane coordinates in the S_2 state results in rotation of the emission TDM and quenching of the initially strong emission oscillator strength. Further, electronic structure calculations (Table 3.2) indicate that an enhanced permanent dipole moment develops due to ICT as the out-of-plane coordinates advance, especially with pyramidalization. The ICT character imparts some solvent sensitivity to the barrier height because the gradient region of the S_2 potential energy surface is increasingly stabilized in polar or polarizable solvents. Despite being nonpolar, carbon disulfide may have a significant impact on the barrier height in β -carotene because of first solvation shell interactions by the highly polarizable sulfur atoms.

The preceding description of the fluorescence emission from β -carotene is unconventional because it discusses the emission line shape as being *dynamic*, reporting fast, large amplitude motions on the S_2 state potential energy surface. As determined in the present experiments with continuous excitation, the recorded fluorescence line shape is the sum of the instantaneous,

time-resolved line shapes emitted by the evolving excited-state ensemble. This situation is made especially obvious in β -carotene for the barrier-crossing molecules because the structural evolution is ultrafast compared to the vibrational relaxation time. In this dynamic picture, the fluorescence line shape, quantum yield, and anisotropy are very sensitive probes of changes of the molecular properties of a chromophore during the emission process.

Several of these ideas have precedence in the work by Kochendoerfer and Mathies¹³⁹ on the fluorescence of the retinal PSBs in rhodopsin and isorhodopsin.^{139,160} As background on this point, recall that the ordering of the lowest two electronic states for the retinal PSBs is inverted compared to that for carotenoids, with the bright S_1 ($^1B_u^+$) state lying below the dark S_2 ($^1A_g^-$) state.¹⁶¹ The quantum yield of fluorescence from S_1 is very small due to fast nonradiative recovery to the ground state and photochemistry in a significant fraction of events in the proteins, less so in solution. The potential energy surface of the S_1 state is usually considered barrierless for 11-*cis*-retinal in rhodopsin and isorhodopsin.^{162,163} In contrast, a low barrier may precede the torsional gradient on the excited state potential energy surface for all-*trans*-retinal in bacteriorhodopsin.^{164,165}

Kochendoerfer and Mathies¹³⁹ observed that the maximum of the fluorescence spectrum from retinal in rhodopsin and isorhodopsin tracks the excitation wavelength as it is tuned to shorter wavelengths. At the same time, however, it is notable that the fluorescence line shape broadens considerably into the near-IR. These behaviors are very similar to those reported here for the fluorescence of β -carotene. By tuning to shorter wavelengths, the energy of the Franck–Condon structure is increased on the excited-state potential energy surface. Given the present paper's context, the increased breadth of the fluorescence spectrum observed by Kochendoerfer and Mathies with excitation at blue wavelengths is probably consistent with the presence of a low

barrier on the retinal excited-state potential energy surface. Although measurements of the fluorescence anisotropy were not reported by Kochendoerfer and Mathies, low fluorescence anisotropies were observed with excitation at shorter wavelengths in early studies of fluorescence in rhodopsin and bacteriorhodopsin.^{166,167} It is also notable that a low anisotropy was observed in the SE signals detected in femtosecond pump–probe anisotropy measurements in bacteriorhodopsin by Haran et al.¹⁶⁸

The present work develops for the first time, however, that fluorescence anisotropy can provide information on the structure of the isoprenoid backbone of a carotenoid prior to and after nonradiative passage from the S_2 state to the S_1 state. As listed in Table 3.1, the minimum fluorescence anisotropy measured in the S_2 and S_1 bands for β -carotene with 430 nm excitation in the polar solvents, chloroform and 2-MTHF, is fully consistent with that calculated for a 90° twist of one of the carbon–carbon bonds in the middle of the isoprenoid backbone (Figure 3.8). This finding indicates that nonradiative decay from S_2 to S_1 occurs when the isoprenoid backbone is significantly distorted along the coupled torsional and pyramidal coordinates but very likely not at the minimum along the S_2 gradient. The S_2 and S_1 emission bands overlap extensively, so an unambiguous determination of the fluorescence anisotropy reached at the CI seam is not possible. But it is clear that the S_1 emission TDM is rotated even further in the nonpolar solvents, to a rotation of almost 50° . This observation is consistent with the rotation of the emission TDM calculated for a pyramidalized, zwitterionic structure. One explanation for this solvent effect is that solvent friction arising from the developing ICT character significantly slows the progress made on the out-of-plane gradient in the S_2 state. Note that the S_1 state apparently retains a distorted conformation over its 10 ps fluorescence lifetime, which is

significantly longer than that expected for vibrational relaxation and thermal equilibration on the S_1 surface.

This discussion indicates that a multicoordinate anharmonic picture is required even to understand qualitatively the excitation wavelength-dependent S_1 emission observed from β -carotene in the four solvents. The weaker and red-shifted S_1 emission band arising from photoexcited molecules retained by the activation barrier originates from a minimum on the S_1 potential energy surface in the Franck–Condon region, which is not displaced very much with respect to the out-of-plane coordinates of the isoprenoid backbone. In comparison, a significantly stronger and somewhat blue shifted S_1 emission band is observed from the molecules that pass over the activation barrier. This emission arises from a distinct minimum on the S_1 potential energy surface with a significant displacement from the Franck–Condon structure along the out-of-plane coordinates. The enhanced strength of the emission from the distorted S_1 minimum can be attributed to an enhanced intensity borrowing from the S_2 state that accompanies out-of-plane distortions of the isoprenoid backbone. Note that the apparent enhancement of the depth of the vibronic structure in the S_1 emission suggests the possibility that this minimum has a larger displacement along the BLA coordinates than the Franck–Condon minimum.

The discussion of solvent friction brings up the important question of how a carotenoid would be expected to behave when bound in a nonpolar site in a photosynthetic light-harvesting protein or reaction center. As noted above, all-*trans* configurations of carotenoids in protein binding sites usually exhibit distorted conformations, which would already favor out-of-plane distortions following the vertical optical transition from the ground state. The present study of the low-temperature fluorescence properties of β -carotene now makes it clear that large amplitude out-of-plane motions are possible even when motions of the isoprenoid backbone are

strongly hindered by the surrounding medium, as they perhaps would be in a protein binding site. The finding that the dynamic intermediate observed over the 80–200 K range exhibits a decreasing fluorescence anisotropy as the solvent melts is proof, however, that the isoprenoid backbone can be further stabilized by undergoing a larger volume of rotation, principally with respect to one of the carbon–carbon bonds near the center of the chain.

The conclusion that out-of-plane distorted S_2 structures can be formed despite steric hindrance from the surrounding medium is fully consistent with the recent studies by Geiger, Borhan, and coworkers^{169,170} on engineered model retinal PSB-binding proteins, where full photoisomerization, not just conformational distortion, is observed even in protein crystals. In these studies, the X-ray crystal structures indicate that the TDM of the photochemical product species would be restricted to point along the binding site's principal axis. A similar conclusion would be made on the basis of Warshel's early analysis of the photoisomerization mechanism in rhodopsin, where the "bicycle pedal" isomerization mechanism is proposed.¹⁴⁸

Part of the motivation behind the present study of β -carotene has been our interest in understanding the spectroscopy of ketocarotenoids, especially those that function in light harvesting and photoprotection in photosynthetic organisms.^{171,172} The presence of a carbonyl substituent on the isoprenoid backbone would be expected to have an especially large impact on the dynamics on the S_2 and S_1 surfaces due to its electron-withdrawing character, which would enhance the permanent dipole moment due to ICT and increase the solvent friction. In previous work from this laboratory, we suggested that evolution from the Franck-Condon S_2 state of peridinin to the S_x state involves twisting and pyramidal distortions of the isoprenoid backbone, both in solution and in the peridinin–chlorophyll protein.^{44,112} As noted above, the lifetime of the S_x state of peridinin is proposed to be significantly longer than that for carotenoids lacking

carbonyl substitution, like β -carotene, because passage on the out-of-plane gradient to the CI seam to the S_1 state would be significantly slowed by solvent friction.^{43–45}

More connected to the present work, however, are the observations we made previously of the fluorescence properties of the ketocarotenoids 3'-hydroxyechinenone and canthaxanthin in the orange carotenoid protein. These two ketocarotenoids exhibit broad, mirror-asymmetric fluorescence spectra assigned to the S_2 state with many of the line shape properties reported here for β -carotene.¹¹⁹ The carbonyl substituents are located on one or both β -ionone end rings, respectively, where they would not be especially strongly coupled to the π -electron density because the rings are canted out of plane with respect to the isoprenoid backbone. These were the first fluorescence studies performed in this laboratory on carotenoids, so we did not examine the S_1 emission bands at that time. The quantum yield of emission from S_2 for 3'-hydroxyechinenone and canthaxanthin in OCP, however, was measured to be several orders of magnitude larger than observed here for β -carotene. We suggested that this finding might be explained if the ketocarotenoid binding site in OCP hinders the out-of-plane distortions that promote nonradiative decay to the S_1 state especially owing to hydrogen-bonding interactions between the carbonyls on the β -ionone end rings and the surrounding protein. This suggestion is in line with the present finding that much larger quantum yields of emission are observed from the β -carotene dynamic intermediate at low temperature over the 80–200 K region.

It could be considered remarkable to conclude from fluorescence anisotropy results that large excited-state torsional distortion could occur within OCP⁰ during fluorescence emission due to the surrounding protein preventing it. However, a similar argument was discussed by Kochendoerfer and Mathies regarding the photoisomerization of retinal in bacteriorhodopsin and rhodopsin¹⁶⁰ where the protein is considered to “catalyze” the torsional motions leading to

photoproducts in those systems.¹⁷³ As a way to informally assess whether it may be reasonable to suggest that such motions of the carotenoid could occur within OCP⁰, we built a series of models in which CAN undergoes right-hand torsional distortions within OCP⁰ (Figure 3.11). These models show that large twists may be possible due to the existence of a cavity on the CTD end of the binding site at the interface between the CTD and NTD of the protein. In these models, the central C₁₅-C₁₅ bond is restricted to a torsion of <70° by the binding site surface. The model structure shown is further distorted by small twists in several bonds¹⁵⁰ on the CTD end of the polyene. This would result in the β-cyclohexene ring moving from a hydrophobic region to the hydrophilic aperture between the CTD and NTD, which would stabilize the developing ICT character of the ketocarotenoid as the torsional motion proceeds.

As a concluding comment, the extent to which the ketocarotenoids can move conformationally out of plane of the isoprenoid backbone after photoexcitation to the S₂ state when bound in a protein site is not well understood at present. In future work, it will clearly be of considerable interest to determine how the fluorescence anisotropy in the near-IR emission bands of the ketocarotenoids is impacted by the presence of the carbonyl substituent. Knowledge of the direction of the emission TDM will allow a better understanding of the evolution of the structure as relaxation occurs on the S₂ potential energy surface and of the nature of the mixing with the S₁ state.

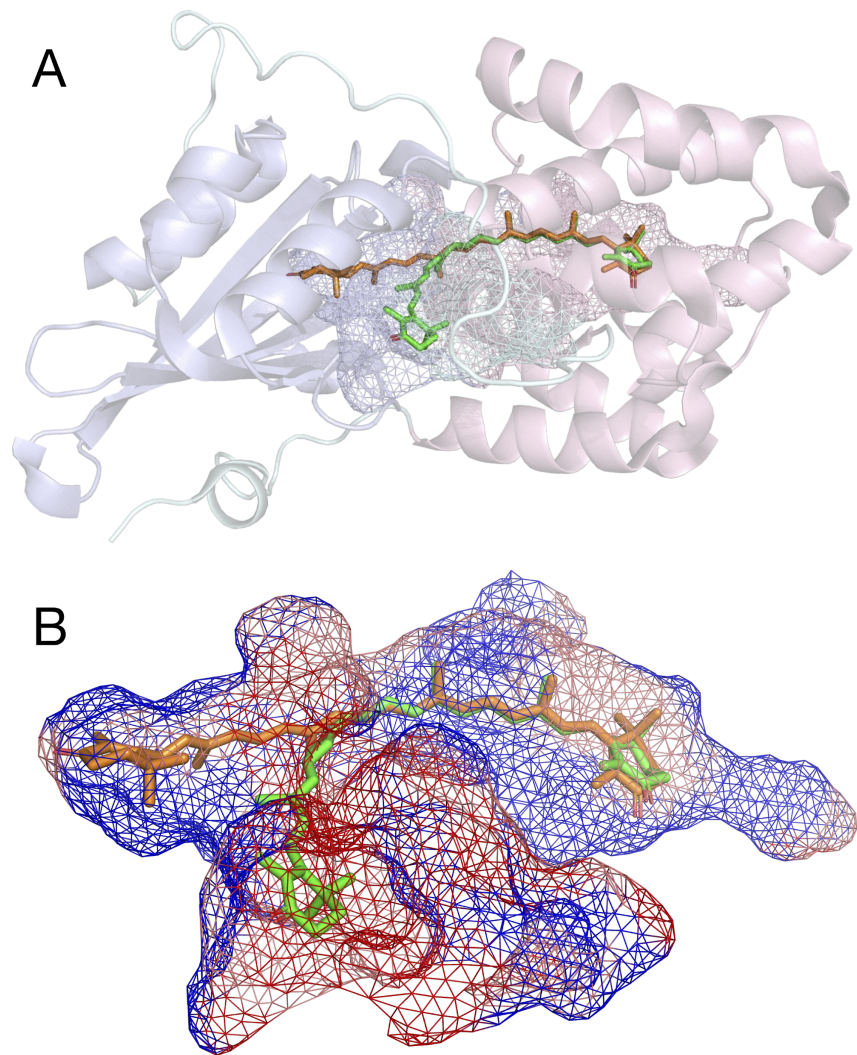


Figure 3.11. Preliminary structural hypothesis for the photoswitching response in OCP⁰ using the *Synechocystis* PCC 6803 (4xb5.pdb) structure. The resting CAN structure (orange) is superimposed with a hypothetical distorted S₂ structure (green) with torsions of the polyene along the C₉-C₁₀, C₁₁-C₁₂, C₁₃-C₁₄, and C₁₅-C₁₅ bonds. (b) Detail of the binding site, with protein surfaces tinted to indicate hydrophobic (blue), polar (pink), and charged/hydrophobic (red) residues.

3.S. Supporting Information

3.S.1. Materials and Experimental Methods

3.S.1.1. Purification of β -carotene

β -carotene purchased from Sigma/Aldrich (C9750-5G) was purified by Amy LaFountain in the Frank laboratory at the University of Connecticut by high-performance liquid chromatography (HPLC) on a Waters 600E/600S multisolvent delivery system equipped with a 2996 photodiode array detector, which has been described previously.^{118,141} For the present samples, the separation employed a Waters Atlantis Prep T3 OBD 5 μ m column (19 x 100 mm). Acetonitrile was delivered isocratically at a flow rate of 7.0 mL/min. All-*trans*- β -carotene fractions collected from the HPLC were dried under nitrogen gas and stored in a freezer at -70°C in darkness until required for experiments.

3.S.1.2. Sample Handling for Fluorescence Spectroscopy

β -carotene was removed from freezer storage and dissolved in one of the four solvents to obtain an absorbance of 0.2 at 460 nm with a 1 cm optical path length. The four solvents, chloroform (Sigma/Aldrich 372978), carbon disulfide (Sigma/Aldrich 335266), *n*-Hexane (EMD HX0295-6), and 2-methyltetrahydrofuran (Sigma/Aldrich 414247), were used as received from freshly opened bottles. Each sample was centrifuged at 17000 \times g prior to recording fluorescence spectra to pellet undissolved, light-scattering particles. Samples were held in 1 cm fused-silica cuvettes either in a Quantum Northwest Peltier-effect temperature controller or in a Janis liquid nitrogen cryostat.

3.S.1.3. Linear Absorption Spectra

Absorption spectra were acquired at room temperature (23 °C) with a Shimadzu UV-2600 spectrophotometer with a spectral bandpass of 2 nm.

In variable temperature work, absorption spectra were acquired with the sample in situ in a Janis liquid nitrogen cryostat or a Peltier cuvette temperature controller (Quantum Northwest) before and after fluorescence measurements. The absorption measurements were carried out using a home-built, fiber optic absorption spectrometer. The light source was an Ocean Optics DH-2000 deuterium/quartz halogen fiber illuminator. Ocean Optics QP400-1-UV-VIS fiber optic cables were used with fiber collimators before and after the sample. The transmitted light was detected by an Ocean Optics USB4000 spectrograph/CCD detector. LabVIEW (National Instruments) programs were used to acquire blank and sample transmission spectra using this apparatus and then to calculate the absorption spectrum.

3.S.1.4. Fluorescence Instrumentation

The home-built fluorescence spectrometer used in the current work was also used for the experiments reported previously on the fluorescence of the ketocarotenoids 3'-hydroxyechinenone and canthaxanthin in the orange carotenoid protein.¹¹⁹ The following specifies improvements to the instrument that were made since that work, and specific details are provided about the polarization optics and the methods used for measurement of the fluorescence anisotropy spectra.

A schematic diagram of the fluorescence spectrometer is provided as Figure 3S.1. Excitation light was obtained from a Thorlabs MNWHL4 broadband LED and a Spectral Products CM112 double monochromator operated in an additive configuration. The monochromator was equipped

with 1200 gr/mm gratings blazed at 500 nm (Spectral Products AG1200-00500-303) and entrance and intermediate slits selected to obtain a spectral bandpass of 2 nm (100 cm^{-1} at 430 nm, 80 cm^{-1} at 500 nm). A Thorlabs SH1 shutter was placed between the LED and monochromator to turn on and off the excitation beam. The monochromatic excitation light selected by the double monochromator was routed to the sample cuvette by fused silica plano-convex collimating and focusing lenses. A Glan-Thompson calcite polarizer (10 mm aperture, Newport) was placed in the collimated excitation beam between the two lenses and manually rotated to set the linear plane of polarization vertically, as outlined below. As an example, the average power delivered to the sample was $5.86 \mu\text{W}$ at 460 nm, as measured by a Newport model 818-SL silicon photodiode detector and a model 835 picowatt optical power meter.

For experiments at 258 K, 273 K, and 298 K, the sample cuvette (fused silica, 1 cm path length) was mounted in a Quantum Northwest LUMA 40 Peltier-type cuvette holder, which was controlled by a Quantum Northwest TC 125 temperature controller. For the experiments at 80 K, 120 K, 160 K, and 200 K, the sample cuvette was mounted in a Janis Research Company VPF-100 cryostat, which was controlled by a Lakeshore Cryotronics Model 321 temperature controller.

Fluorescence emission and Raman scattering was collected 90° from the excitation beam by a f2 fused-silica spherical lens. The collimated emission beam between was passed through a Glan-Taylor calcite polarizer (20 mm aperture, Melles-Griot). The polarizer was mounted in a Newport 495B-A motorized rotation stage, which was driven by a Newport PMC200-P motion controller. After passage through the Glan Taylor polarizer, the collimated fluorescence beam was focused onto the input slit of an Acton Research SP-150 spectrograph (150 mm focal length)

by a second fused-silica spherical lens. The fluorescence emission was dispersed in the spectrograph by a 300 gr/mm diffraction grating (500 nm blaze wavelength). The input slit was adjusted to obtain a spectral bandpass of 4 nm (110 cm^{-1} at 600 nm), as determined by the breadth of Hg emission lines. The grating was turned to image the 423 to 927 nm range of the emission spectrum onto a Princeton Instruments Versarray 1300B CCD detector (back-illuminated sensor chip, liquid nitrogen cooled), which was equipped with a shutter controlled by the Princeton Instruments ST-133 detector controller. The spectrograph and CCD detector were calibrated using an Ocean Optics HG-1 Hg calibration lamp mounted at the sample's position. The wavelength dependence of the sensitivity of the spectrograph and CCD detector was calibrated using the emission spectrum of the quartz halogen lamp in the Ocean Optics DH-2000 fiber illuminator. Data acquisition was controlled using LabVIEW (National Instruments) and Scientific Imaging Toolkit for LabVIEW (R Cubed Software Consultants, LLC) routines, the latter providing subroutines to operate the CCD detector.

3.S.1.5. Data Acquisition

Fluorescence data acquisition was performed by recording dark background (excitation beam shutter closed), magic angle (54.7°), and horizontal (90°) fluorescence emission spectra, with the given angle specifying the orientation of the emission polarizer relative to the vertical excitation polarizer. For each excitation wavelength, four 5-minute exposures of the CCD detector were accumulated sequentially for the dark background, magic angle polarization, and horizontal polarization spectra. This procedure was repeated four times, which obtains a total of 16 five-minute CCD exposures for each type. Accordingly, each data acquisition sequence required 4 hours in total, with the sample repeatedly allowed to recover in the dark for 20 minute periods

during the procedure during the acquisition of background spectra. 2.5 minute CCD exposures were employed for the 2-MTHF series over the 80–200 K range owing to the larger quantum yields observed.

The absorption spectrum of the β -carotene samples was measured before and after the fluorescence data acquisition cycle in order to determine if permanent photobleaching occurred or if photoproducts were accumulated. No changes in absorption were detected in any of the samples monitored during these experiments.

3.S.1.6. Data Processing

After data acquisition using the protocol described above, cosmic ray spikes were removed from the vertically binned emission and dark background spectra by comparing the detected emission intensities of the 16 equivalent CCD exposures to that of the mean on a horizontal pixel-by-pixel (dispersed wavelength) basis. A reading from one of the scans was rejected from the set if its intensity was outside of 0.9 times the standard deviation of the mean. The surviving readings were then averaged. After subtraction of the averaged background spectrum, the magic-angle intensity spectra reported in this paper were then corrected for the wavelength dependence of the emission spectrograph and CCD detector sensitivity using a reference spectrum from an Ocean Optics DH-2000 quartz halogen lamp (2960 K). Intensity correction was not performed when computing the fluorescence anisotropy spectra because the correction factor is cancelled out by the anisotropy ratio calculation.

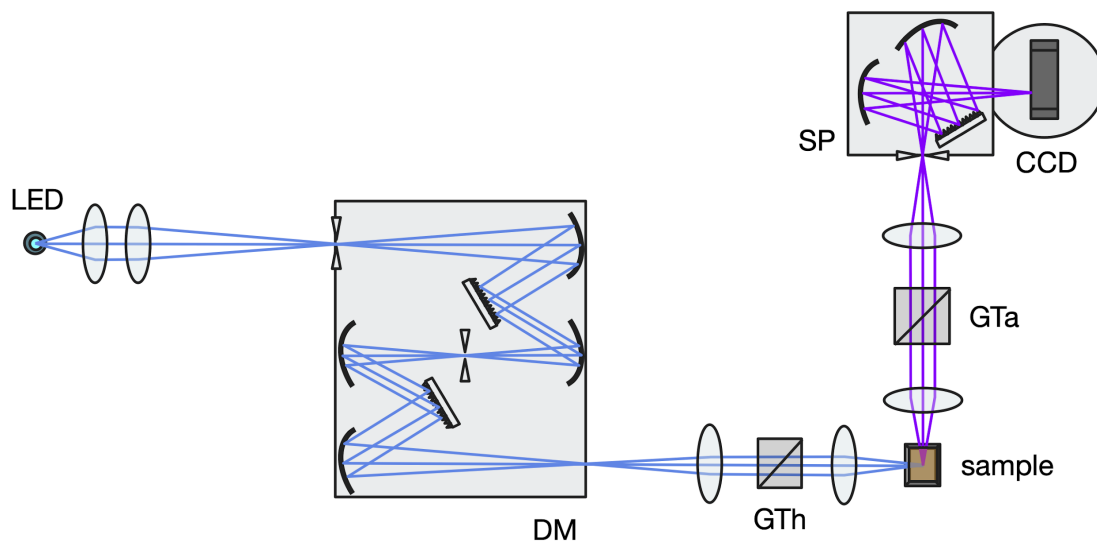


Figure 3S.1. Schematic diagram of the home-built fluorescence spectrometer used in the present work. Symbols: DM, double monochromator; GTh, Glan-Thompson polarizer; GTa, Glan-Taylor polarizer; SP, grating spectrograph.

3.S.1.7. Determination of Fluorescence Anisotropy

The fluorescence anisotropy spectrum from the β -carotene samples was obtained by measuring the fluorescence emission spectrum with the emission polarizer oriented 90° and at the magic angle, 54.7° , from the vertically oriented excitation polarizer, as described above. This procedure was adopted in lieu of the usual practice of recording 90° and 0° spectra because it obtains anisotropy spectra with an improved signal/noise ratio. Owing to the low fluorescence quantum yield for β -carotene, it was necessary to use long exposures of the CCD detector to obtain good signal/noise ratios. With 0° polarization, however, the length of time that the CCD detector could be exposed is significantly reduced owing to the presence of several relatively intense Raman scattering lines, which are highly polarized.

The calculations used to determine the anisotropy using the 90° and 54.7° spectra is described below. As shown below in Figure 3S.2, this procedure returns fluorescence anisotropy spectra that are indistinguishable from those conventionally recorded with 0° and 90° spectra with a reference fluorophore, rhodamine 6G.

The equations that follow specify the orientation of the emission and excitation polarizers in the fluorescence spectrometer using subscripts. For example, F_{xy} indicates the fluorescence intensity spectrum recorded as a function of emission wavelength when the excitation polarizer is in the x orientation and the emission polarizer is in the y orientation. The subscript V indicates that the plane of linear polarization for the polarizer is vertical; H indicates a horizontal polarization, and M indicates orientation at the magic angle, 54.7° .

Using this notation, the total fluorescence emission spectrum, F_T , is obtained as

$$F_T = 2 G F_{VH} + F_{VV} \quad (3S.1)$$

The G factor used in equation 3S.1 is determined as the ratio of vertically and horizontally polarized emission spectra from a reference fluorophore, in our case rhodamine 6G in methanol, with horizontally polarized excitation.

$$G = \frac{F_{HV}}{F_{HH}} \quad (3S.2)$$

G is determined by the efficiencies of the diffraction grating and curved mirrors in the emission spectrograph.⁸⁸ The total fluorescence F_T is proportional to the polarized fluorescence intensity measured with the emission polarizer at the magic angle,

$$F_T = C F_{VM} \quad (3S.3)$$

Combining equations 3S.1 and 3S.3,

$$F_T = C F_{VM} = 2 G F_{VH} + F_{VV} \quad (3S.4)$$

Rearranging equation 3S.4 obtains two results

$$C = \frac{2 G F_{VH} + F_{VV}}{F_{VM}} \quad (3S.5)$$

$$F_{VV} = C F_{VM} - 2 G F_{VH} \quad (3S.6)$$

The anisotropy spectrum can be calculated from the 90° and magic-angle emission spectra using these results as

$$r = \frac{F_{VV} - G F_{VH}}{F_{VV} + 2 G F_{VH}} = \frac{C F_{VM} - 2 G F_{VH} - G F_{VH}}{C F_{VM} - 2 G F_{VH} + 2 G F_{VH}} = \frac{C F_{VM} - 3 G F_{VH}}{C F_{VM}} \quad (3S.7)$$

3.S.1.8. Rhodamine 6G reference spectra

Figure 3S.2 shows a determination of the fluorescence anisotropy from a reference chromophore, rhodamine 6G in glycerol, using 90° and magic-angle spectra. The results are not

distinguishable from those obtained with 0° and 90° spectra. Also note that the anisotropy is flat all the way across the fluorescence emission spectrum except near the excitation wavelength, where highly polarized scattered light is observed. This response should be compared to the emission fluorescence anisotropy spectra reported in this paper for β -carotene, which often exhibit a pronounced decrease in the near-IR region of the spectrum. The rhodamine 6G anisotropy spectrum establishes that the low anisotropies determined for β -carotene do not arise from deficiencies in the optics nor from the data acquisition or data processing procedures.

3.S.1.9. Determination of Fluorescence Quantum Yield

The fluorescence quantum yield was estimated in comparison to that for rhodamine 6G in methanol as a standard, for which $\Phi_F = 0.93$.¹⁷⁴ The integrated area of the fluorescence emission spectrum for a β -carotene solution was determined by fitting it to a normalized lognormal line shape⁹⁶ or to a sum of lognormal line shapes. The absolute quantum yield was then calculated as discussed in reference¹⁵⁷ using

$$\Phi_{f,car} = \Phi_{f,ref} \frac{F_{car}}{F_{ref}} \frac{[1 - 10^{-A_{ref}} n_{car}^2]}{[1 - 10^{-A_{car}} n_{ref}^2]} \quad (3S.8)$$

where $\Phi_{F,car}$ and $\Phi_{F,ref}$ are the quantum yields, F_{car} and F_{ref} are the integrated areas of the fluorescence spectra, A_{car} and A_{ref} are the absorptions at the excitation wavelengths, and n_{car} and n_{ref} are the indices of refraction of the two solvents used in the β -carotene (car) and rhodamine 6G (ref) samples, respectively. The fitted lognormal line shapes were optimized to avoid interference from the excitation light scattering and Raman scattering peaks in the fluorescence spectra. The resulting estimates of the absolute fluorescence quantum yield reliably allow a comparison of the yields in the different solvents.

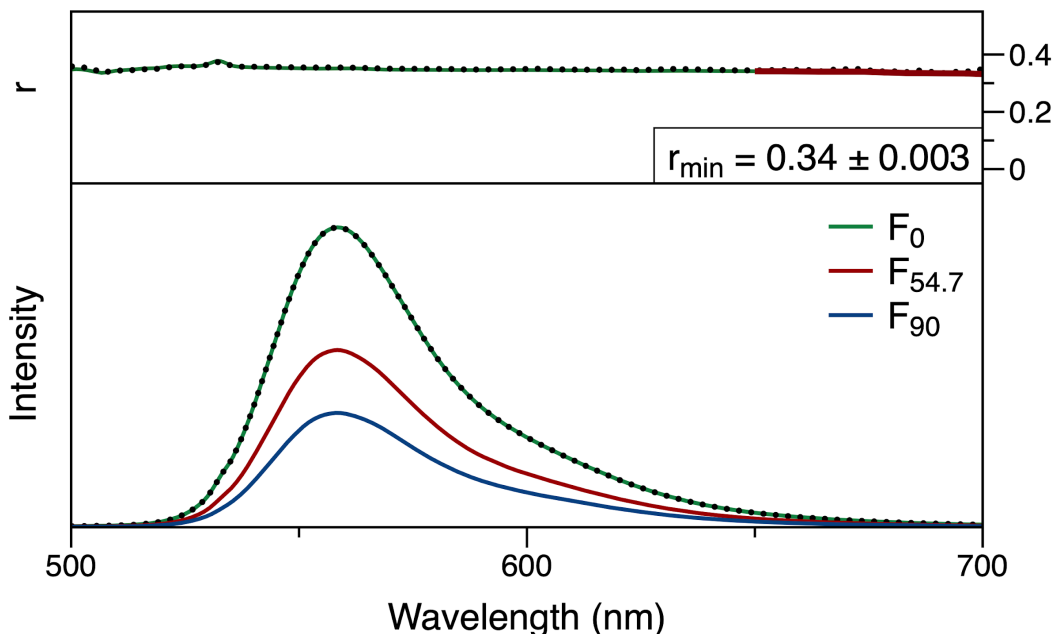


Figure 3S.2. Fluorescence emission anisotropy (top panel) and linearly polarized fluorescence emission spectra (bottom panel) from rhodamine 6G in glycerol at 23 °C with excitation at 532 nm. The angles indicated for the emission polarizer are with respect to the vertically polarized excitation polarizer. The green anisotropy trace was calculated conventionally using the F_0 and F_{90} spectra. The superimposed dotted anisotropy trace was calculated using the magic angle, $F_{54.7}$, and F_{90} spectra using equations 3S.1–3S.7. The red trendline in the >650 nm region of the anisotropy spectrum was used to calculate the minimum anisotropy value, 0.34 ± 0.003 .

Notes: The fluorescence anisotropy reported previously for rhodamine B and rhodamine 101 in glycerol solvent is 0.38-0.39.^{175,176} Similarly, the fluorescence anisotropy for rhodamine 6G in glycerol and propane-1,2-diol is 0.37.¹⁷⁷ These values were determined at the peak emission wavelength. The results we obtained for rhodamine 6G are comparable to these published values. Figure 3S.2 shows that the fluorescence anisotropy for rhodamine 6G is 0.35 at 560 nm and 0.34 as averaged over the >650 nm region.

3.S.1.10. Excitation wavelength dependence of the fluorescence emission and anisotropy wavelength spectra from β -carotene

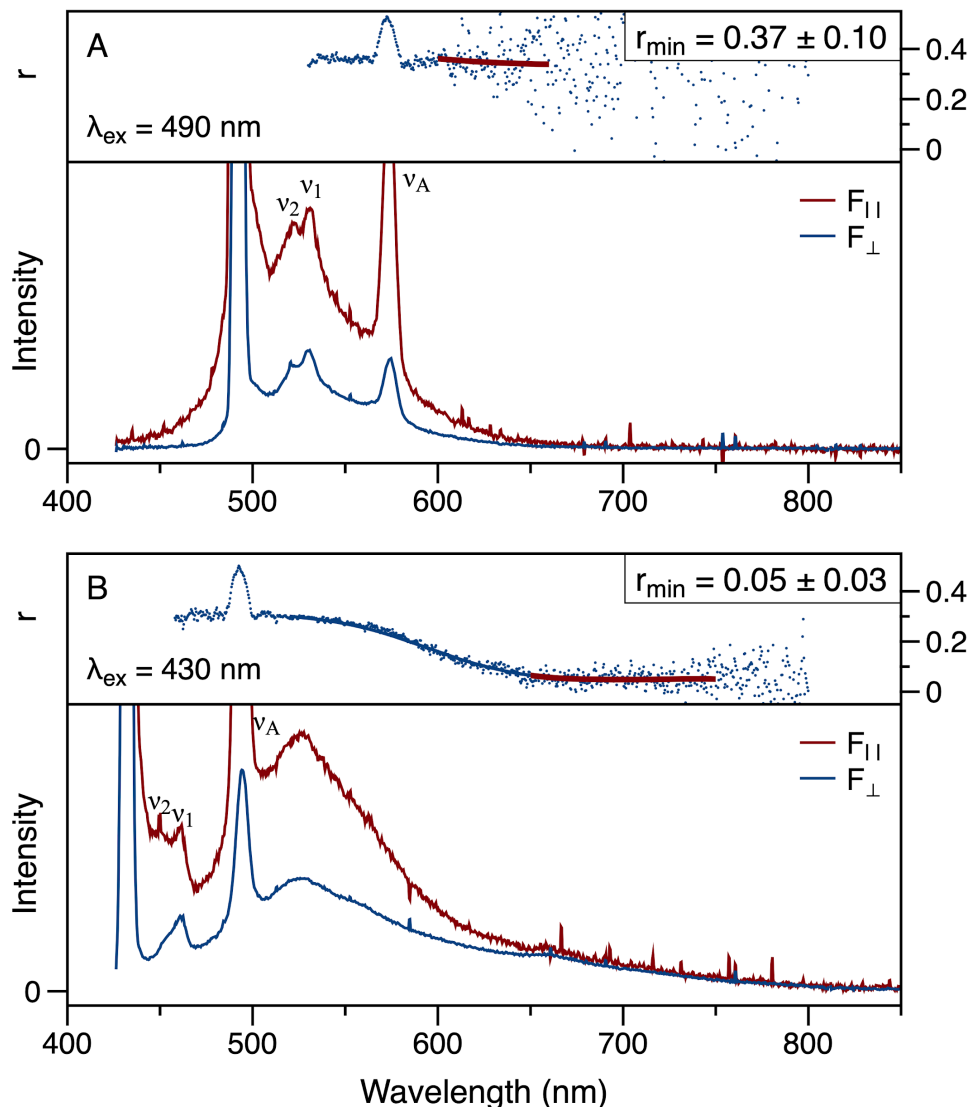


Figure 3S.3. Parallel (F_{\parallel} , red) and perpendicular (F_{\perp} , blue) polarization components of the fluorescence emission and the fluorescence anisotropy (r) for β -carotene in hexane at 23 °C, with excitation at (a) 490 nm and (b) 430 nm. The anisotropy spectrum is superimposed with a smoothing spline trendline, with the red bolded section indicating the region used to estimate the minimum anisotropy and its confidence interval. The positions of resonance Raman peaks from β -carotene ($\nu_1 = 1517 \text{ cm}^{-1}$ and $\nu_2 = 1157 \text{ cm}^{-1}$)¹³⁴ and of a non-resonant Raman peak from the hexane solvent ($\nu_A = 2966 \text{ cm}^{-1}$)¹³⁵ are marked.

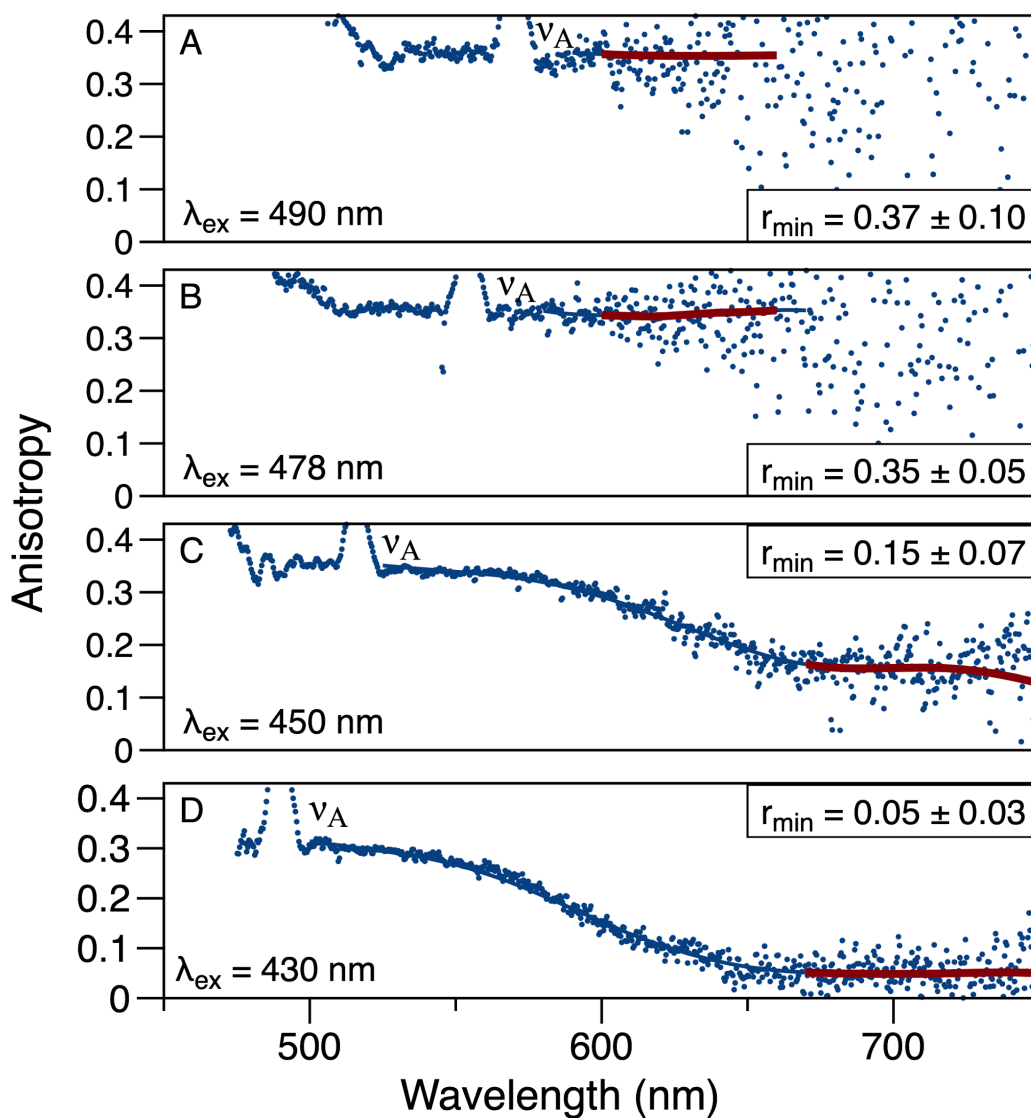


Figure 3S.4. Excitation wavelength (λ_{ex}) dependence of the fluorescence anisotropy for β -carotene in hexane solvent at 23 °C, with the trend indicated by a smoothing spline curve. The minimum anisotropy, r_{min} , was determined by averaging over the wavelength region marked in red. The highly polarized Raman scattering peak from the hexane solvent ($\nu_{\text{A}} = 2966 \text{ cm}^{-1}$)¹³⁵ is marked.

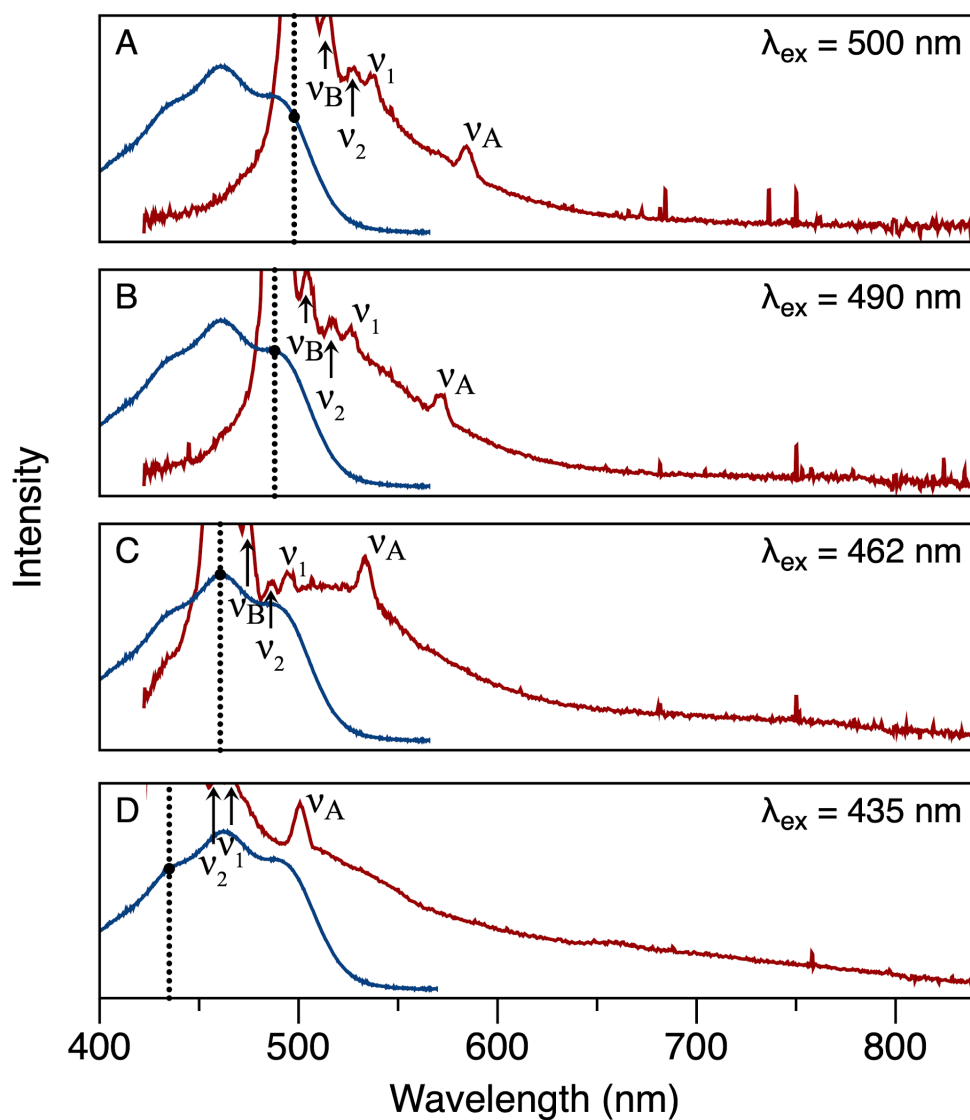


Figure 3S.5. Absorption (blue) and fluorescence emission (red) spectra at four excitation wavelengths from β -carotene in chloroform solvent at 23 °C. The emission polarizer was oriented at the magic angle (54.6°) with respect to the excitation polarizer for the fluorescence spectra. The excitation wavelength (dotted black line) and Raman scattering peaks from β -carotene ($\nu_1 = 1517$ cm^{-1} and $\nu_2 = 1157$ cm^{-1})¹³⁴ and from the chloroform solvent ($\nu_A = 2966$ cm^{-1} and $\nu_B = 732$ cm^{-1})¹⁴² are marked.

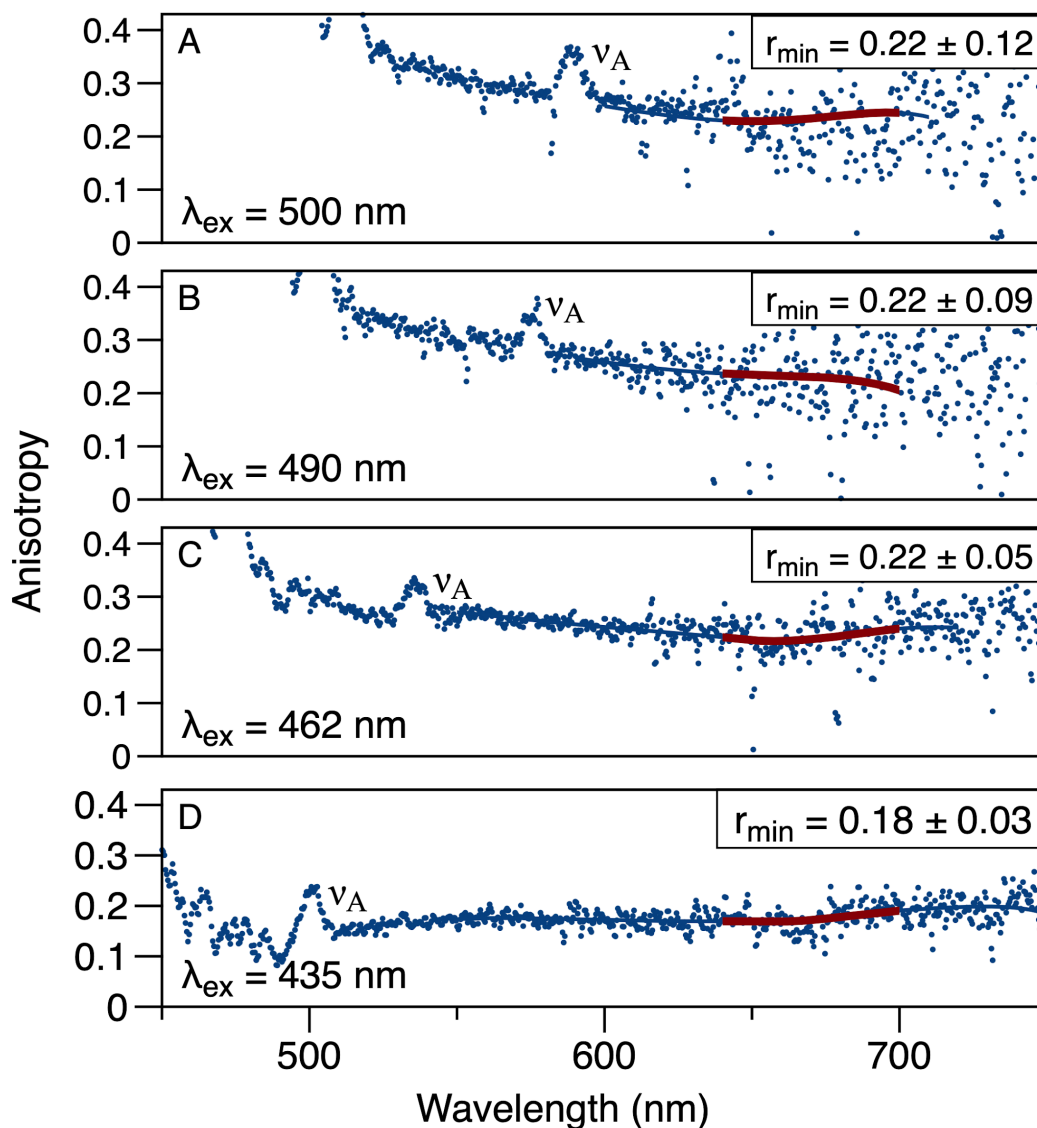


Figure 3S.6. Excitation wavelength (λ_{ex}) dependence of the fluorescence lineshape and anisotropy for β -carotene in chloroform solvent at 23 °C, with the trend indicated by a smoothing spline curve. The minimum anisotropy, r_{min} , was determined by averaging over the wavelength region marked in red. The highly polarized Raman scattering peak from the chloroform solvent ($\nu_A = 2966 \text{ cm}^{-1}$)¹⁴² is marked.

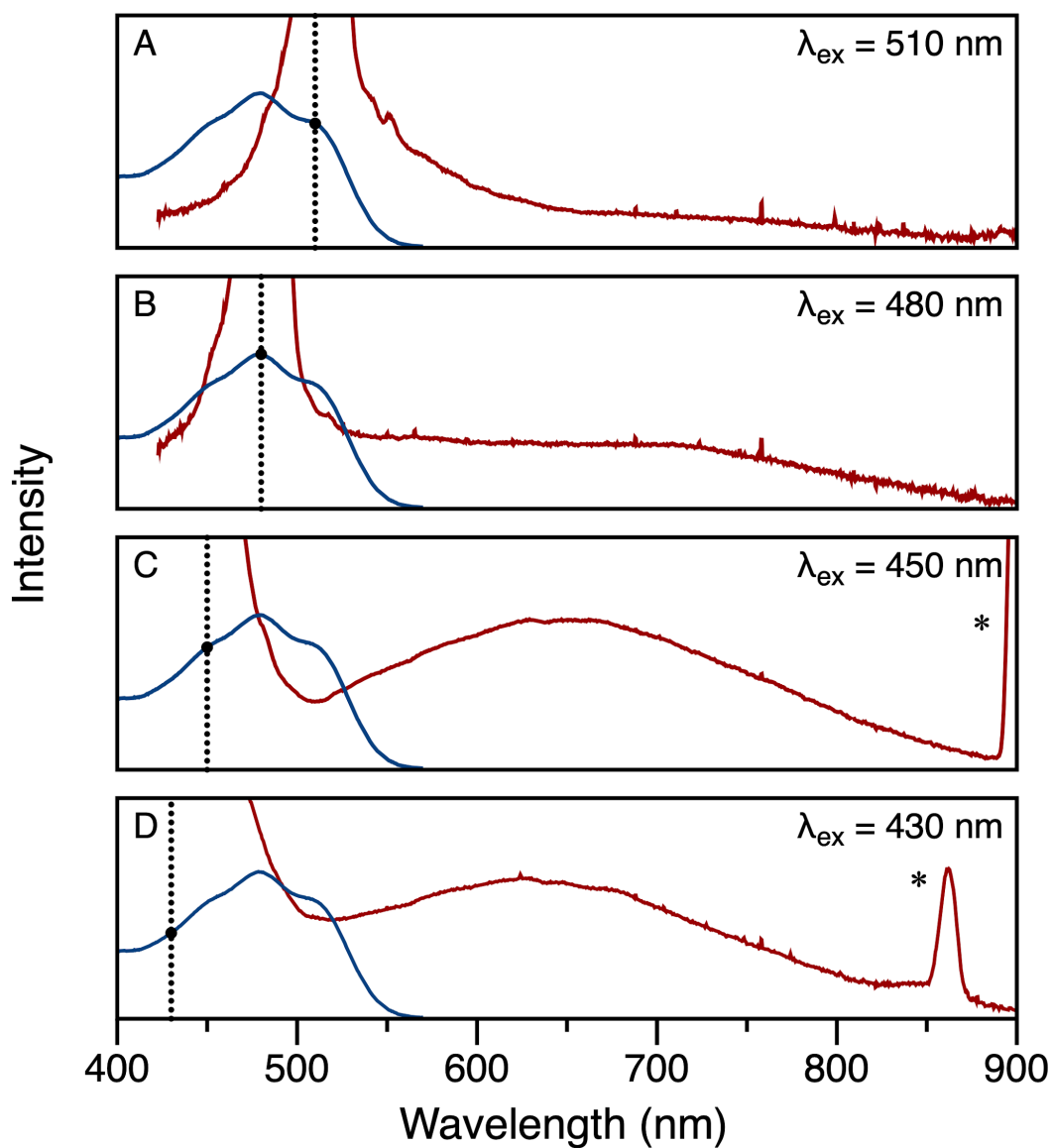


Figure 3S.7. Absorption (blue) and fluorescence emission (red) spectra at four excitation wavelengths from β -carotene in carbon disulfide solvent at 23 °C. For the fluorescence spectra, the emission polarizer was oriented at the magic angle (54.6°) with respect to the excitation polarizer for the fluorescence spectra. The excitation wavelength (dotted black line) is marked. Also marked (*) is the second-order excitation light scattering peak.

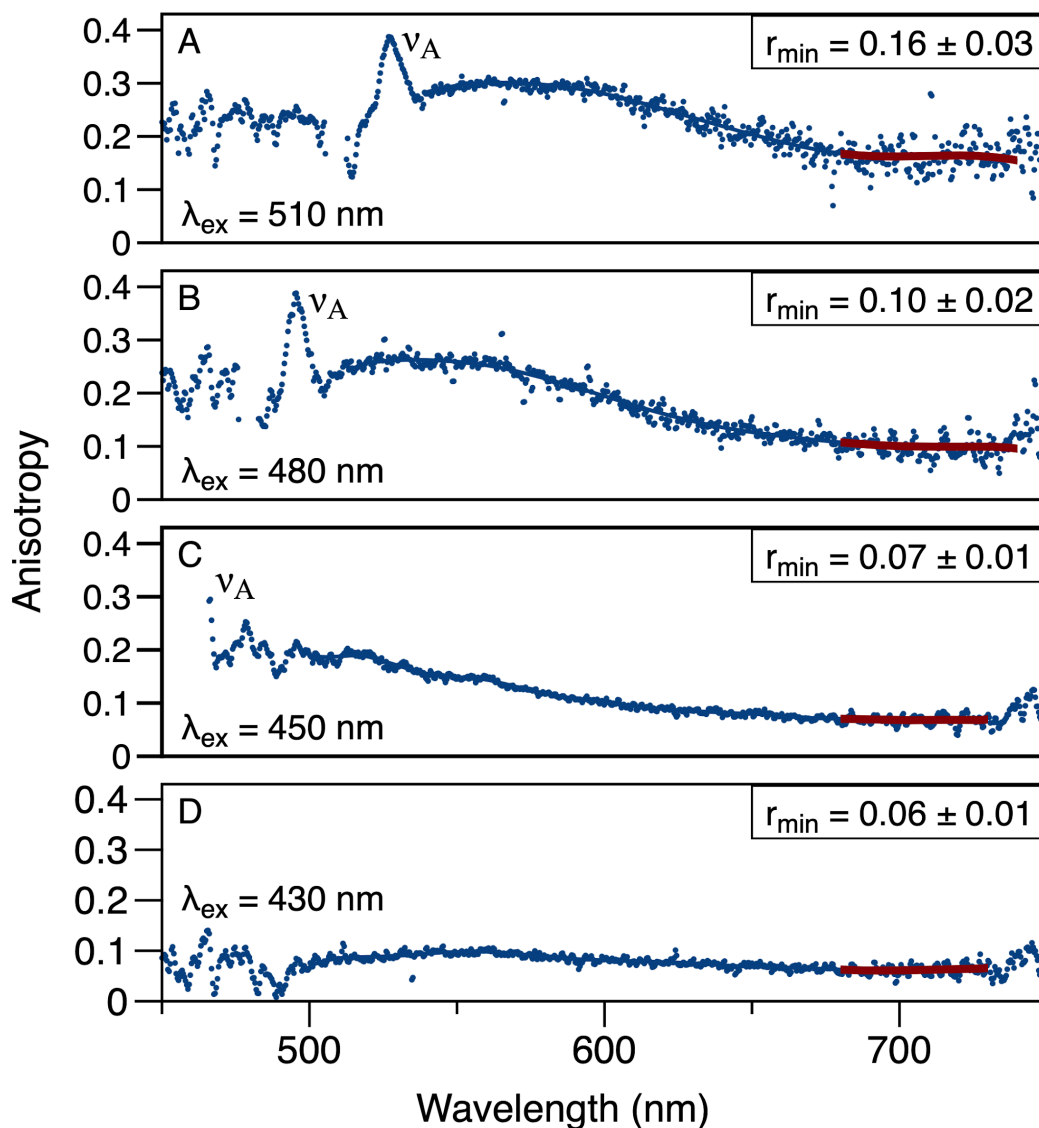


Figure 3S.8. Excitation wavelength (λ_{ex}) dependence of the fluorescence lineshape and anisotropy for β -carotene in carbon disulfide solvent at 293 K, with the trend indicated by a smoothing spline curve. The minimum anisotropy, r_{min} , was determined by averaging over the wavelength region marked in red. The highly polarized Raman scattering peak from the CS_2 solvent ($\nu_{\text{A}} = 658 \text{ cm}^{-1}$)¹⁴⁴ is marked.

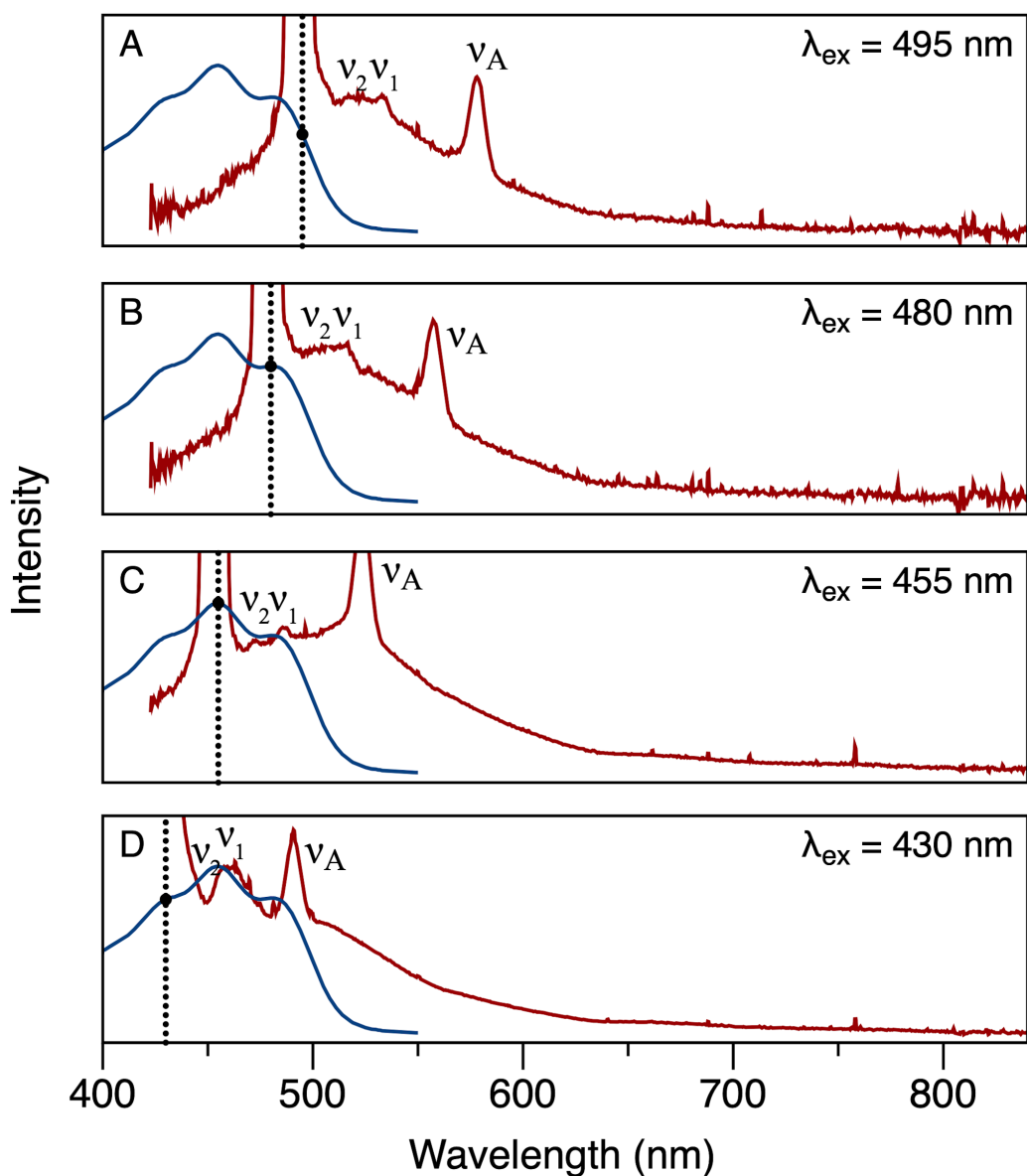


Figure 3S.9. Absorption (blue) and fluorescence emission (red) spectra at four excitation wavelengths from β -carotene in 2-MTHF at 23 °C. For the fluorescence spectra, the emission polarizer was oriented at the magic angle (54.6°) with respect to the excitation polarizer for the fluorescence spectra. The excitation wavelength (dotted black line) and Raman scattering features from β -carotene ($\nu_1 = 1517 \text{ cm}^{-1}$ and $\nu_2 = 1157 \text{ cm}^{-1}$)¹³⁴ and from the 2-MTHF solvent ($\nu_A = 2915 \text{ cm}^{-1}$)¹⁴³ are marked.

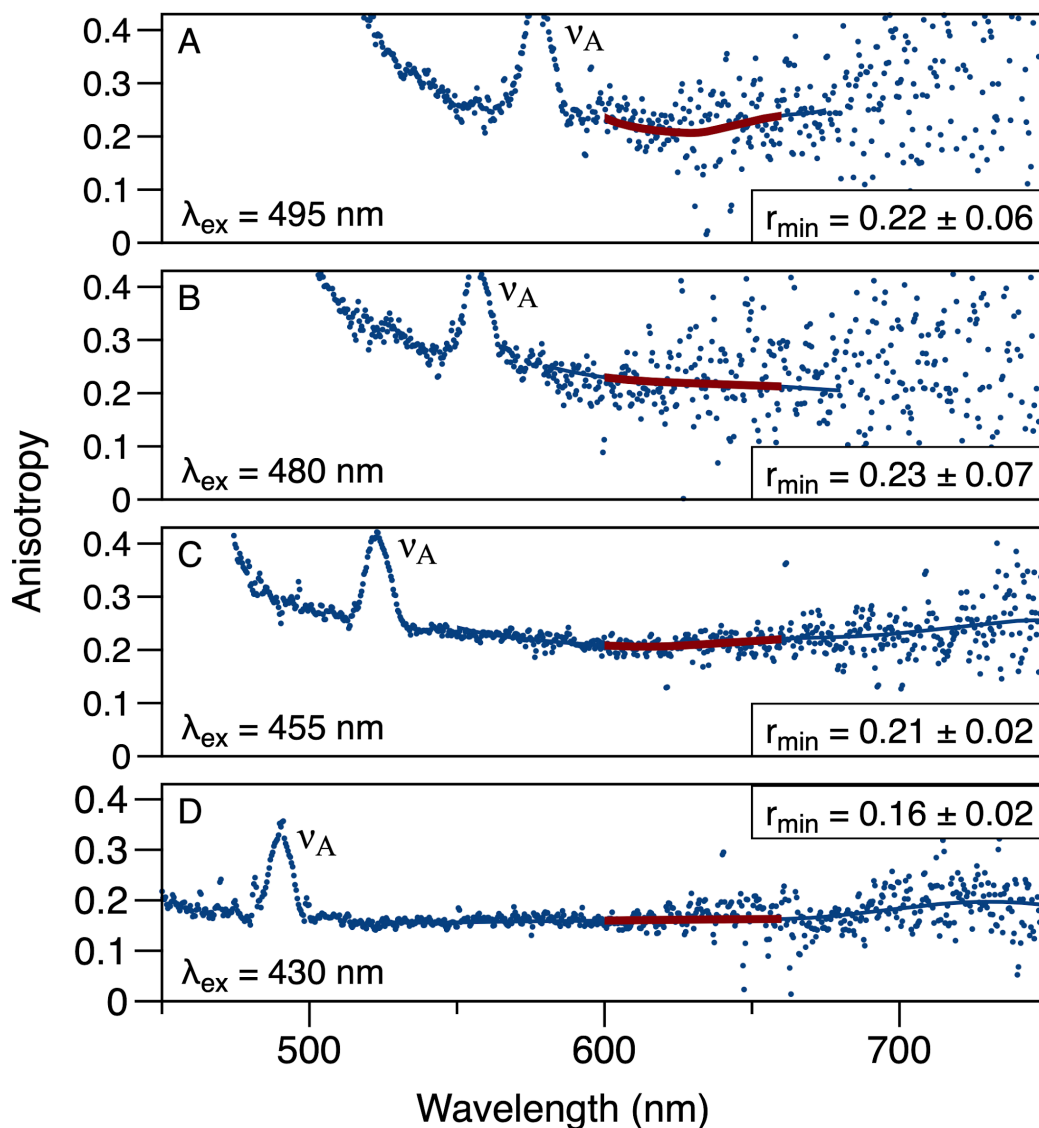


Figure 3S.10. Excitation wavelength (λ_{ex}) dependence of the fluorescence anisotropy for β -carotene in 2-MTHF at 293 K, with the trend shown superimposed with a smoothing spline curve. The minimum anisotropy, r_{min} , was determined by averaging over the wavelength region marked in red. The highly polarized Raman scattering peak from the 2-MTHF solvent ($\nu_A = 2915 \text{ cm}^{-1}$)¹⁴³ is marked.

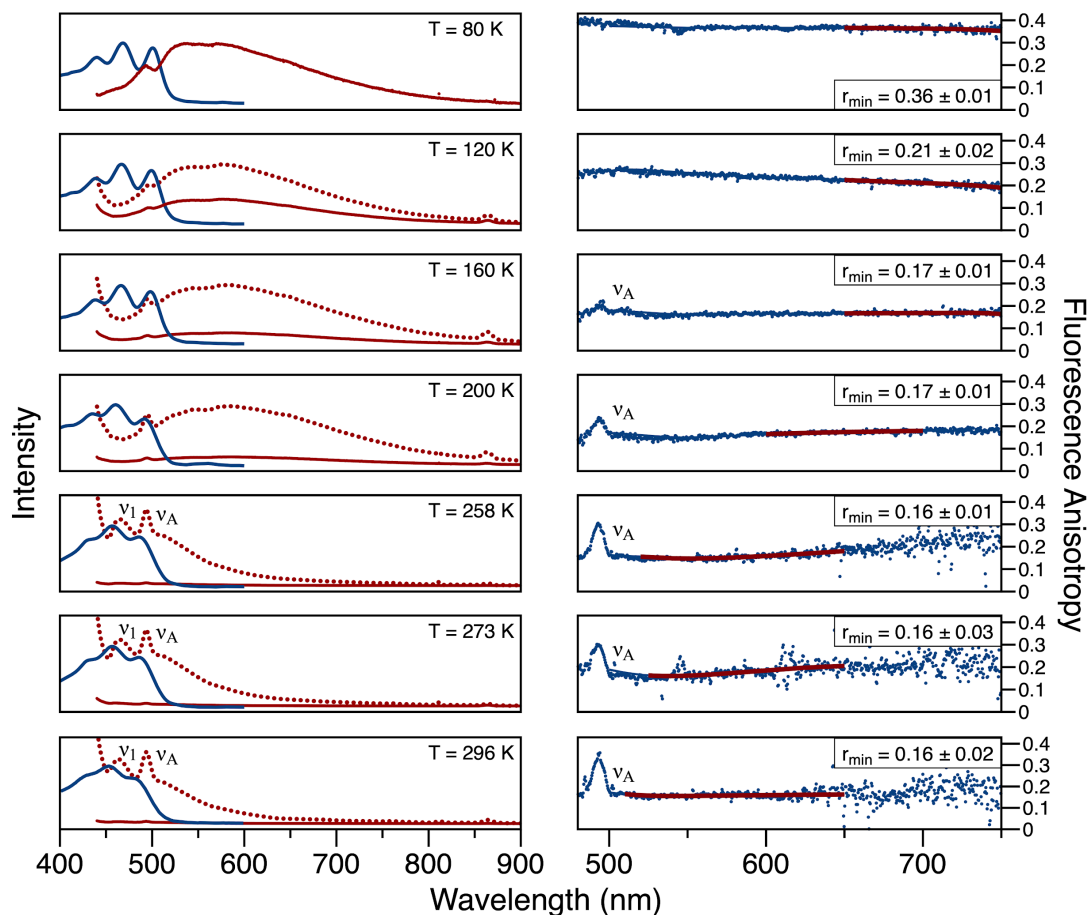


Figure 3S.11. Absorption, fluorescence emission, and fluorescence anisotropy spectra of β -carotene in 2-MTHF over the 80–296 K range. The absorption (blue) and fluorescence (red) spectra (left panel) are scaled relative to those at 80 K; autoscaled fluorescence spectra (red dotted) are superimposed to allow comparison of the emission line shapes. The fluorescence anisotropy spectra (right panel) are shown superimposed with a smoothing spline curve. The Raman scattering features from β -carotene ($\nu_1 = 1517 \text{ cm}^{-1}$ and $\nu_2 = 1157 \text{ cm}^{-1}$)¹³⁴ and from the 2-MTHF solvent ($\nu_A = 2915 \text{ cm}^{-1}$)¹⁴³ are marked.

3.S.2. MBO Simulations

The absorption spectrum of β -carotene displays a partially resolved set of vibronic lines owing to a progression in the resonance Raman-active BLA modes of the isoprenoid backbone at 1517 cm^{-1} and 1157 cm^{-1} .¹³⁴ Simulations of the absorption spectrum using the Multimode Brownian Oscillator (MBO) model in hexane and 2-MTHF solvent, Figures S3.8 and S3.9, respectively, show that the depth of the resolved vibronic structure in the absorption spectrum decreases as the reorganization energy (or system–bath coupling) increases.

Our implementation of the MBO model for simulations of the linear absorption spectrum and of the third-order transient grating spectrum have been described previously in the supporting information for chapter 2.^{43,119} The MBO model parameters (Tables S3.1–S3.3) were optimized here to fit the experimental absorption spectrum; in addition to the two vibrational frequencies, two exponential and two underdamped vibrational components were incorporated in the model's energy-gap time-correlation function.¹⁰⁰ The simulation accurately describes the experimental spectrum from the low wavenumber/long wavelength onset up to the peak of the absorption spectrum at the second vibronic peak. Only the two principal BLA vibrational coordinates were included in the model, which partly accounts for the divergence of the observed and simulated spectra at shorter wavelengths. Although the β -carotene samples used in these experiments were purified by HPLC to isolate the all-trans configuration, the ground-state ensemble may also include small contributions from cis configurations, which exhibit an absorption peak assigned to the $S_0 \rightarrow S_3$ transition in the 300–350 nm ($28500\text{--}33,300\text{ cm}^{-1}$) region of the spectrum.¹⁴¹

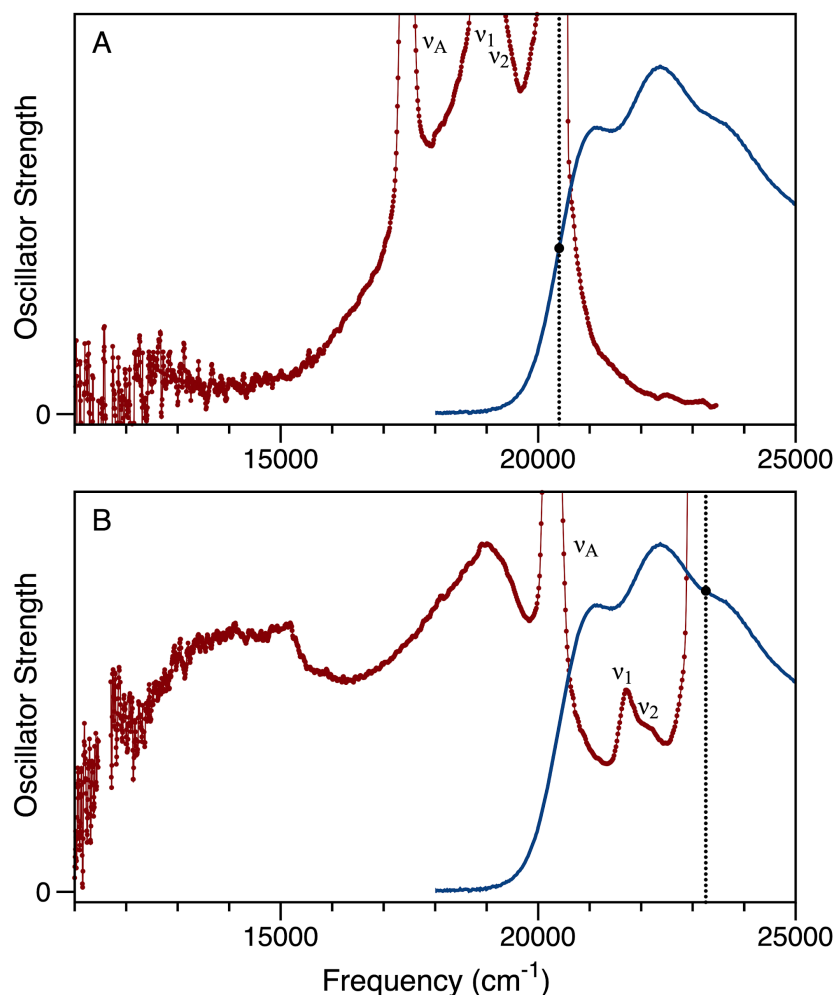


Figure 3S.12. Absorption (blue) and fluorescence emission (red) spectra at 23 °C from β -carotene in hexane, plotted with arbitrary vertical scaling as relative oscillator strengths, $\epsilon(\nu)/\nu$ and $\lambda^2 F(\nu)/\nu^3$, respectively, as a function of the wavenumber ν . The fluorescence spectra were recorded with excitation at (a) 490 nm ($20,400 \text{ cm}^{-1}$) and (b) 430 nm ($23,260 \text{ cm}^{-1}$), as indicated by dotted black lines. The positions of resonance Raman peaks from β -carotene ($\nu_1 = 1517 \text{ cm}^{-1}$ and $\nu_2 = 1157 \text{ cm}^{-1}$)¹³⁴ and of a non-resonant Raman peak from the hexane solvent ($\nu_A = 2966 \text{ cm}^{-1}$)¹³⁵ are marked. Numerical simulations of the absorption and fluorescence emission oscillator strength spectra (blue and red dashed, respectively) using the MBO model are superimposed. The model parameters (Table 2S.1) were optimized to fit the experimental absorption spectrum; two exponential and two underdamped vibrational components were incorporated in the model, as previously implemented.¹¹⁹

Table 3S.1. Energy gap time-correlation function parameters^a in the MBO model for the absorption spectrum from β -carotene in hexane at 296 K in Figure 3S.8.

Mode	λ (cm ⁻¹)	ω_v (cm ⁻¹)	τ (fs)
Gaussian	130	————	10
Exponential 1	350	————	500
Exponential 2	430	————	1000
Vibration 1	410	1150	2000
Vibration 2	1370	1525	2000
Total	2690	————	————

^aVertical S₀–S₂ energy gap: $\omega_{eg} = 22780$ cm⁻¹; reorganization energy, λ ; mode frequency, ω_v ; damping time, τ .

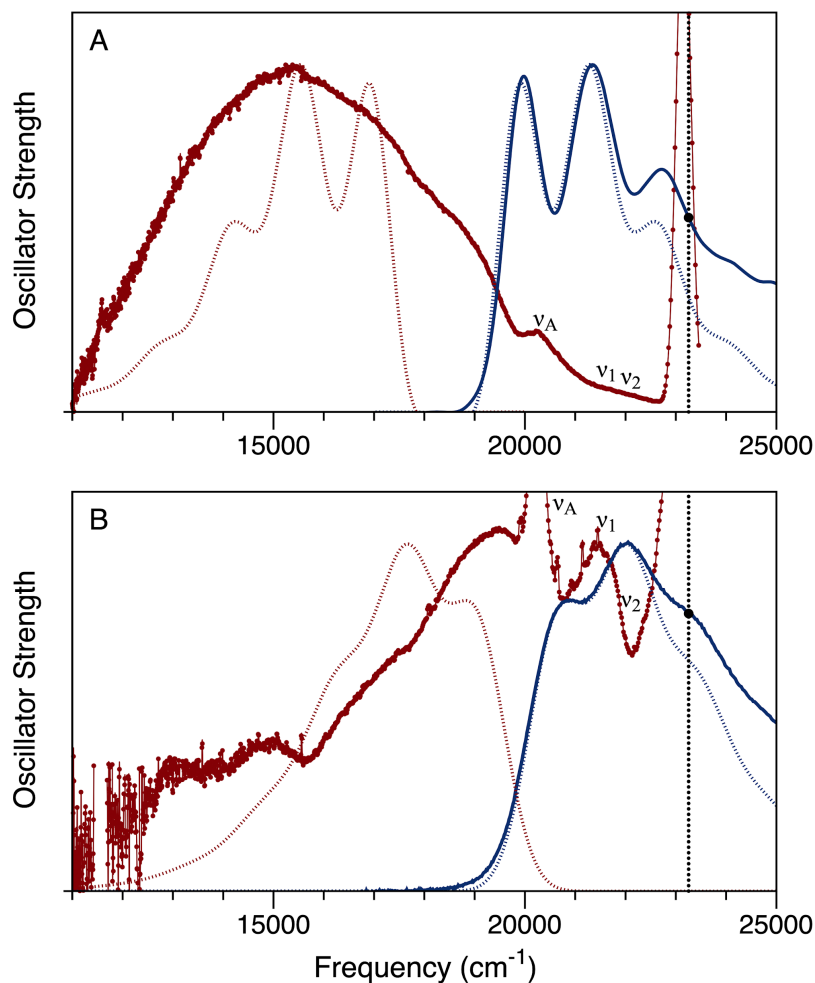


Figure 3S.13. Absorption (blue) and fluorescence emission (red) spectra at 296 K from β -carotene in 2-MTHF, plotted with arbitrary vertical scaling as relative oscillator strengths, $\epsilon(\nu)/\nu$ and $\lambda^2 F(\nu)/\nu^3$, respectively, as a function of the wavenumber ν . The sample temperature was maintained at (a) 80 K and (b) 296 K. The fluorescence spectra were recorded with excitation at 430 nm ($23,300 \text{ cm}^{-1}$), as indicated by dotted black lines. The positions of resonance Raman lines from β -carotene ($\nu_1 = 1517 \text{ cm}^{-1}$ and $\nu_2 = 1157 \text{ cm}^{-1}$)¹³⁴ and of a non-resonant Raman line from the 2-MTHF solvent ($\nu_A, 2915 \text{ cm}^{-1}$)¹⁴³ are marked. Numerical simulations of the absorption and fluorescence emission oscillator strength spectra (blue and red dashed, respectively) using the MBO model are superimposed. The model parameters (Tables 2S.2 and 2S.3) were optimized to fit the experimental absorption spectrum at each temperature; two exponential and two underdamped vibrational components were incorporated in the model, as previously implemented.¹¹⁹

Table 3S.2. Energy gap time-correlation function parameters^a in the MBO model for the absorption spectrum from β -carotene in 2-MTHF at 80 K in Figure 3.12a.

Mode	λ (cm ⁻¹)	ω_v (cm ⁻¹)	τ (fs)
Gaussian (G)	300	————	10
Exponential (E,1)	600	————	500
Exponential (E,2)	750	————	1000
Vibrational (v,1)	550	1150	2000
Vibrational (v,2)	950	1525	2000
Total	3150	————	————

^aVertical S₀–S₂ energy gap: $\omega_{eg} = 21560$ cm⁻¹; reorganization energy, λ ; mode frequency, ω_v ; damping time, τ .

Table 3S.3. Energy gap time-correlation function parameters^a in the MBO model for the absorption spectrum from β -carotene in 2-MTHF at 296 K in Figure 3.12b.

Mode	λ (cm ⁻¹)	ω_v (cm ⁻¹)	τ (fs)
Gaussian (G)	160	————	10
Exponential (E,1)	300	————	500
Exponential (E,2)	400	————	1000
Vibrational (v,1)	550	1150	2000
Vibrational (v,2)	1150	1525	2000
Total	2560	————	————

^aVertical S₀–S₂ energy gap: $\omega_{eg} = 22400$ cm⁻¹; reorganization energy, λ ; mode frequency, ω_v ; damping time, τ .

REFERENCES

REFERENCES

- (1) Polívka, T.; Sundström, V. Ultrafast Dynamics of Carotenoid Excited States—from Solution to Natural and Artificial Systems. *Chem. Rev.* **2004**, *104* (4), 2021–2071.
- (2) Polívka, T.; Frank, H. A. Molecular Factors Controlling Photosynthetic Light Harvesting by Carotenoids. *Acc. Chem. Res.* **2010**, *43* (8), 1125–1134.
- (3) Polívka, T.; Sundström, V. Dark Excited States of Carotenoids: Consensus and Controversy. *Chem. Phys. Lett.* **2009**, *477*, 1–11.
- (4) Beck, W. F.; Bishop, M. M.; Roscioli, J. D.; Ghosh, S.; Frank, H. A. Excited State Conformational Dynamics in Carotenoids: Dark Intermediates and Excitation Energy Transfer. *Arch. Biochem. Biophys.* **2015**, *572*, 175–183.
- (5) Hashimoto, H.; Uragami, C.; Yukihiro, N.; Gardiner, A. T.; Cogdell, R. J. Understanding/unravelling Carotenoid Excited Singlet States. *J. R. Soc. Interface* **2018**, *15* (141), 20180026.
- (6) Tully, J. C. Perspective: Nonadiabatic Dynamics Theory. *J. Chem. Phys.* **2012**, *137* (22), 22A301.
- (7) Levine, B. G. Nonadiabatic Dynamics of *cis–trans* Photoisomerization—a First Principles Study. Ph. D. dissertation, University of Illinois at Urbana-Champaign, Urbana, Illinois, 2007.
- (8) Gillbro, T.; Cogdell, R. J. Carotenoid Fluorescence. *Chem. Phys. Lett.* **1989**, *158* (3), 312–316.
- (9) Demchenko, A. P.; Tomin, V. I.; Chou, P.-T. Breaking the Kasha Rule for More Efficient Photochemistry. *Chem. Rev.* **2017**, *117* (21), 13353–13381.
- (10) Christensen, R. L. The Electronic States of Carotenoids. In *The Photochemistry of Carotenoids*; Frank, H. A., Young, A. J., Britton, G., Cogdell, R. J., Eds.; Springer Netherlands: Dordrecht, 1999; pp 137–159.
- (11) Frank, H. A.; Christensen, R. L. Excited Electronic States and the Photochemistry and Photophysics of Carotenoids. In *The Carotenoids*; Britton, G., Liaaen-Jensen, S., Pfander, H., Eds.; Birkhauser Verlag: Basel, 2008; pp 167–188.
- (12) Schulten, K.; Karplus, M. On the Origin of a Low-Lying Forbidden Transition in Polyenes and Related Molecules. *Chem. Phys. Lett.* **1972**, *14*, 305–309.
- (13) Hudson, B.; Kohler, B. Linear Polyene Electronic Structure and Spectroscopy. *Annu. Rev. Phys. Chem.* **1974**, *25* (1), 437–460.

- (14) Holtom, G. R.; McClain, W. M. Two-Photon Excitation Spectra of the Low Energy Excited States of Diphenylhexatriene and Diphenyloctatetraene. *Chem. Phys. Lett.* **1976**, *44* (3), 436–439.
- (15) Hudson, B. S.; Kohler, B. E. A Low-Lying Weak Transition in the Polyene α,ω -Diphenyloctatetraene. *Chem. Phys. Lett.* **1972**, *14* (3), 299–304.
- (16) Hudson, B. S.; Kohler, B. E.; Schulten, K. Linear Polyene Electronic Structure and Potential Surfaces. In *Excited States*; Lim, E. C., Ed.; Elsevier, 1982; Vol. 6, pp 1–95.
- (17) Nagae, H.; Kuki, M.; Zhang, J.-P.; Sashima, T.; Mukai, Y.; Koyama, Y. Vibronic Coupling through the In-Phase, C=C Stretching Mode Plays a Major Role in the $2A_g^-$ to $1A_g^-$ Internal Conversion of All-*trans*- β -Carotene. *J. Phys. Chem. A* **2000**, *104* (18), 4155–4166.
- (18) Yarkony, D. R. Conical Intersections: Diabolical and Often Misunderstood. *Acc. Chem. Res.* **1998**, *31*, 511–518.
- (19) Levine, B. G.; Martínez, T. J. Isomerization through Conical Intersections. *Annu. Rev. Phys. Chem.* **2007**, *58*, 613–634.
- (20) Fuß, W.; Haas, Y.; Zilberg, S. Twin States and Conical Intersections in Linear Polyenes. *Chem. Phys.* **2000**, *259* (2), 273–295.
- (21) Ruiz, D. S.; Cembran, A.; Garavelli, M.; Olivucci, M.; Fuß, W. Structure of the Conical Intersections Driving the *cis*–*trans* Photoisomerization of Conjugated Molecules. *Photochem. Photobiol.* **2002**, *76* (6), 622–633.
- (22) Wasielewski, M. R.; Kispert, L. D. Direct Measurement of the Lowest Excited Singlet State Lifetime of All-*Trans*- β -Carotene and Related Carotenoids. *Chem. Phys. Lett.* **1986**, *128*, 238–243.
- (23) Frank, H. A.; Bautista, J. A.; Josue, J.; Pendon, Z.; Hiller, R. G.; Sharples, F. P.; Gosztola, D.; Wasielewski, M. R. Effect of the Solvent Environment on the Spectroscopic Properties and Dynamics of the Lowest Excited States of Carotenoids. *J. Phys. Chem. B* **2000**, *104* (18), 4569–4577.
- (24) Warshel, A.; Karplus, M. Calculation of $\pi\pi^*$ Excited State Conformations and Vibronic Structure of Retinal and Related Molecules. *J. Am. Chem. Soc.* **1974**, *96*, 5677–5689.
- (25) Hemley, R.; Kohler, B. E. Electronic Structure of Polyenes Related to the Visual Chromophore. A Simple Model for the Observed Band Shapes. *Biophys. J.* **1977**, *20* (3), 377–382.
- (26) Requena, A.; Cerón-Carrasco, J. P.; Bastida, A.; Zúñiga, J.; Miguel, B. A Density Functional Theory Study of the Structure and Vibrational Spectra of β -Carotene, Capsanthin, and Capsorubin. *J. Phys. Chem. A* **2008**, *112* (21), 4815–4825.

- (27) Fiedor, L.; Pilch, M. Side Methyl Groups Control the Conformation and Contribute to Symmetry Breaking of Isoprenoid Chromophores. *Angew. Chem. Int. Ed Engl.* **2018**, *57* (22), 6501–6506.
- (28) Andersson, P. O.; Takaichi, S.; Cogdell, R. J.; Gillbro, T. Photophysical Characterization of Natural *cis*-Carotenoids. *Photochem. Photobiol.* **2001**, *74* (4), 549–557.
- (29) Fiedor, L.; Heriyanto; Fiedor, J.; Pilch, M. Effects of Molecular Symmetry on the Electronic Transitions in Carotenoids. *J. Phys. Chem. Lett.* **2016**, *7*, 1821–1829.
- (30) Wei, T.; Balevičius, V.; Polívka, T.; Ruban, A. V.; Duffy, C. D. P. How Carotenoid Distortions May Determine Optical Properties: Lessons from the Orange Carotenoid Protein. *Phys. Chem. Chem. Phys.* **2019**, *21* (41), 23187–23197.
- (31) Kuhlman, T. S.; Glover, W. J.; Mori, T.; Møller, K. B.; Martínez, T. J. Between Ethylene and Polyenes—the Non-Adiabatic Dynamics of Cis-Dienes. *Faraday Discuss.* **2012**, *157*, 193–212; discussion 243–284.
- (32) Levine, B. G.; Martínez, T. J. Ab Initio Multiple Spawning Dynamics of Excited Butadiene: Role of Charge Transfer. *J. Phys. Chem. A* **2009**, *113*, 12815–12824.
- (33) Shu, Y.; Truhlar, D. G. Doubly Excited Character or Static Correlation of the Reference State in the Controversial 2^1A_g State of Trans-Butadiene? *J. Am. Chem. Soc.* **2017**, *139* (39), 13770–13778.
- (34) Glover, W. J.; Mori, T.; Schuurman, M. S.; Boguslavskiy, A. E.; Schalk, O.; Stolow, A.; Martínez, T. J. Excited State Non-Adiabatic Dynamics of the Smallest Polyene, Trans 1,3-Butadiene. II. Ab Initio Multiple Spawning Simulations. *J. Chem. Phys.* **2018**, *148* (16), 164303.
- (35) Andreussi, O.; Knecht, S.; Marian, C. M.; Kongsted, J.; Mennucci, B. Carotenoids and Light-Harvesting: From DFT/MRCI to the Tamm–Dancoff Approximation. *J. Chem. Theory Comput.* **2015**, *11* (2), 655–666.
- (36) Spezia, R.; Knecht, S.; Mennucci, B. Excited State Characterization of Carbonyl Containing Carotenoids: A Comparison between Single and Multireference Descriptions. *Phys. Chem. Chem. Phys.* **2017**, *19* (26), 17156–17166.
- (37) Sashima, T.; Koyama, Y.; Yamada, T.; Hashimoto, H. The $1B_u^+$, $1B_u^-$, and $2A_g^-$ Energies of Crystalline Lycopene, β -Carotene, and Mini-9- β -Carotene as Determined by Resonance-Raman Excitation Profiles: Dependence of the $1B_u^-$ State Energy on the Conjugation Length. *J. Phys. Chem. B* **2000**, *104* (20), 5011–5019.
- (38) Cerullo, G.; Polli, D.; Lanzani, G.; De Silvestri, S.; Hashimoto, H.; Cogdell, R. J. Photosynthetic Light Harvesting by Carotenoids: Detection of an Intermediate Excited State. *Science* **2002**, *298* (5602), 2395–2398.

- (39) Polli, D.; Cerullo, G.; Lanzani, G.; De Silvestri, S.; Yanagi, K.; Hashimoto, H.; Cogdell, R. Conjugation Length Dependence of Internal Conversion in Carotenoids: Role of the Intermediate State. *Phys. Rev. Lett.* **2004**, *93*, 163002.
- (40) Ostroumov, E.; Müller, M. G.; Marian, C. M.; Kleinschmidt, M.; Holzwarth, A. R. Electronic Coherence Provides a Direct Proof for Energy-Level Crossing in Photoexcited Lutein and β -Carotene. *Phys. Rev. Lett.* **2009**, *103* (10), 108302.
- (41) Ostroumov, E. E.; Mulvaney, R. M.; Cogdell, R. J.; Scholes, G. D. Broadband 2D Electronic Spectroscopy Reveals a Carotenoid Dark State in Purple Bacteria. *Science* **2013**, *340* (6128), 52–56.
- (42) Tavan, P.; Schulten, K. Electronic Excitations in Finite and Infinite Polyenes. *Phys. Rev. B Condens. Matter* **1987**, *36* (8), 4337–4358.
- (43) Ghosh, S.; Bishop, M. M.; Roscioli, J. D.; Mueller, J. J.; Shepherd, N. C.; LaFountain, A. M.; Frank, H. A.; Beck, W. F. Femtosecond Heterodyne Transient-Grating Studies of Nonradiative Decay of the S_2 ($1^1B_u^+$) State of β -Carotene: Contributions from Dark Intermediates and Double-Quantum Coherences. *J. Phys. Chem. B* **2015**, *119* (47), 14905–14924.
- (44) Ghosh, S.; Bishop, M. M.; Roscioli, J. D.; LaFountain, A. M.; Frank, H. A.; Beck, W. F. Femtosecond Heterodyne Transient Grating Studies of Nonradiative Deactivation of the S_2 ($1^1B_u^+$) State of Peridinin: Detection and Spectroscopic Assignment of an Intermediate in the Decay Pathway. *J. Phys. Chem. B* **2016**, *120*, 3601–3614.
- (45) Ghosh, S.; Roscioli, J. D.; Bishop, M. M.; Gurchiek, J. K.; LaFountain, A. M.; Frank, H. A.; Beck, W. F. Torsional Dynamics and Intramolecular Charge Transfer in the S_2 ($1^1B_u^+$) Excited State of Peridinin: A Mechanism for Enhanced Mid-Visible Light Harvesting. *J. Phys. Chem. Lett.* **2016**, *7* (18), 3621–3626.
- (46) Sanchez-Galvez, A.; Hunt, P.; Robb, M. A.; Olivucci, M.; Vreven, T.; Schlegel, H. B. Ultrafast Radiationless Deactivation of Organic Dyes: Evidence for a Two-State Two-Mode Pathway in Polymethine Cyanines. *J. Am. Chem. Soc.* **2000**, *122* (12), 2911–2924.
- (47) Ben-Nun, M.; Martínez, T. J. Photodynamics of Ethylene: Ab Initio Studies of Conical Intersections. *Chem. Phys.* **2000**, *259* (2), 237–248.
- (48) de Weerd, F. L.; van Stokkum, I. H. M.; van Grondelle, R. Subpicosecond Dynamics in the Excited State Absorption of All-*trans*- β -Carotene. *Chem. Phys. Lett.* **2002**, *354*, 38–43.
- (49) Bonačić-Koutecký, V.; Bruckmann, P.; Hiberty, P.; Koutecký, J.; Leforestier, C.; Salem, L. Sudden Polarization in the Zwitterionic Z1 Excited States of Organic Intermediates. Photochemical Implications. *Angew. Chem. Int. Ed.* **1975**, *14* (8), 575–576.
- (50) Bonačić-Koutecký, V.; Koutecký, J.; Michl, J. Neutral and Charged Biradicals, Zwitterions, Funnels in S_1 , and Proton Translocation: Their Role in Photochemistry, Photophysics, and Vision. *Angew. Chem. Int. Ed.* **1987**, *26* (3), 170–189.

- (51) Michl, J.; Bonačić-Koutecký, V. *Electronic Aspects of Organic Photochemistry*; Wiley, 1990.
- (52) Liebel, M.; Schnedermann, C.; Kukura, P. Vibrationally Coherent Crossing and Coupling of Electronic States during Internal Conversion in β -Carotene. *Phys. Rev. Lett.* **2014**, *112* (19), 198302.
- (53) Wu, Y. P.; Krogmann, D. W. The Orange Carotenoid Protein of *Synechocystis* PCC 6803. *Biochim. Biophys. Acta* **1997**, *1322* (1), 1–7.
- (54) Kerfeld, C. A.; Sawaya, M. R.; Brahmamdam, V.; Cascio, D.; Ho, K. K.; Trevithick-Sutton, C. C.; Krogmann, D. W.; Yeates, T. O. The Crystal Structure of a Cyanobacterial Water-Soluble Carotenoid Binding Protein. *Structure* **2003**, *11*, 55–65.
- (55) Kerfeld, C. A. Water-Soluble Carotenoid Proteins of Cyanobacteria. *Arch. Biochem. Biophys.* **2004**, *430* (1), 2–9.
- (56) Boulay, C.; Abasova, L.; Six, C.; Vass, I.; Kirilovsky, D. Occurrence and Function of the Orange Carotenoid Protein in Photoprotective Mechanisms in Various Cyanobacteria. *Biochim. Biophys. Acta* **2008**, *1777* (10), 1344–1354.
- (57) Wilson, A.; Punginelli, C.; Gall, A.; Bonetti, C.; Alexandre, M.; Routaboul, J. M.; Kerfeld, C. A.; van Grondelle, R.; Robert, B.; Kennis, J. T.; Kirilovsky, D. A Photoactive Carotenoid Protein Acting as Light Intensity Sensor. *Proc. Natl. Acad. Sci. U. S. A.* **2008**, *105*, 12075–12080.
- (58) Berera, R.; van Stokkum, I. H.; d’Haene, S.; Kennis, J. T.; van Grondelle, R.; Dekker, J. P. A Mechanism of Energy Dissipation in Cyanobacteria. *Biophys. J.* **2009**, *96* (6), 2261–2267.
- (59) Wilson, A.; Kinney, J. N.; Zwart, P. H.; Punginelli, C.; D’Haene, S.; Perreau, F.; Klein, M. G.; Kirilovsky, D.; Kerfeld, C. A. Structural Determinants Underlying Photoprotection in the Photoactive Orange Carotenoid Protein of Cyanobacteria. *J. Biol. Chem.* **2010**, *285*, 18364–18375.
- (60) Leverenz, R. L.; Sutter, M.; Wilson, A.; Gupta, S.; Thurotte, A.; de Carbon, C. B.; Petzold, C. J.; Ralston, C.; Perreau, F.; Kirilovsky, D.; Kerfeld, C. A. A 12 Å Carotenoid Translocation in a Photoswitch Associated with Cyanobacterial Photoprotection. *Science* **2015**, *348*, 1463–1466.
- (61) Manodori, A.; Melis, A. Cyanobacterial Acclimation to Photosystem I or Photosystem II Light. *Plant Physiol.* **1986**, *82*, 185–189.
- (62) Wilson, A.; Ajlani, G.; Verbavatz, J. M.; Vass, I.; Kerfeld, C. A.; Kirilovsky, D. A Soluble Carotenoid Protein Involved in Phycobilisome-Related Energy Dissipation in Cyanobacteria. *Plant Cell* **2006**, *18*, 992–1007.

- (63) Kirilovsky, D.; Kerfeld, C. A. Cyanobacterial Photoprotection by the Orange Carotenoid Protein. *Nat. Plants* **2016**, *2*, 16180.
- (64) Kerfeld, C. A.; Melnicki, M. R.; Sutter, M.; Dominguez-Martin, M. A. Structure, Function and Evolution of the Cyanobacterial Orange Carotenoid Protein and Its Homologs. *New Phytol.* **2017**, *215*, 937–951.
- (65) Campbell, D.; Hurry, V.; Clarke, A. K.; Gustafsson, P.; Öquist, G. Chlorophyll Fluorescence Analysis of Cyanobacterial Photosynthesis and Acclimation. *Microbiol. Mol. Biol. Rev.* **1998**, *62*, 667–683.
- (66) Rakhimberdieva, M. G.; Stadnichuk, I. N.; Elanskaya, I. V.; Karapetyan, N. V. Carotenoid-Induced Quenching of the Phycobilisome Fluorescence in Photosystem II-Deficient Mutant of *Synechocystis* Sp. *FEBS Lett.* **2004**, *574* (1-3), 85–88.
- (67) Gorbunov, M. Y.; Kuzminov, F. I.; Fadeev, V. V.; Kim, J. D.; Falkowski, P. G. A Kinetic Model of Non-Photochemical Quenching in Cyanobacteria. *Biochim. Biophys. Acta* **2011**, *1807* (12), 1591–1599.
- (68) Gwizdala, M.; Wilson, A.; Kirilovsky, D. In Vitro Reconstitution of the Cyanobacterial Photoprotective Mechanism Mediated by the Orange Carotenoid Protein in *Synechocystis* PCC 6803. *Plant Cell* **2011**, *23*, 2631–2643.
- (69) Leverenz, R. L.; Jallet, D.; Li, M. D.; Mathies, R. A.; Kirilovsky, D.; Kerfeld, C. A. Structural and Functional Modularity of the Orange Carotenoid Protein: Distinct Roles for the N- and C-Terminal Domains in Cyanobacterial Photoprotection. *Plant Cell* **2014**, *26*, 426–437.
- (70) Zhang, H.; Liu, H.; Niedzwiedzki, D. M.; Prado, M.; Jiang, J.; Gross, M. L.; Blankenship, R. E. Molecular Mechanism of Photoactivation and Structural Location of the Cyanobacterial Orange Carotenoid Protein. *Biochemistry* **2014**, *53* (1), 13–19.
- (71) Gupta, S.; Guttman, M.; Leverenz, R. L.; Zhumadilova, K.; Pawlowski, E. G.; Petzold, C. J.; Lee, K. K.; Ralston, C. Y.; Kerfeld, C. A. Local and Global Structural Drivers for the Photoactivation of the Orange Carotenoid Protein. *Proc. Natl. Acad. Sci. U. S. A.* **2015**, *112* (41), E5567–E5574.
- (72) Punginelli, C.; Wilson, A.; Routaboul, J. M.; Kirilovsky, D. Influence of Zeaxanthin and Echinenone Binding on the Activity of the Orange Carotenoid Protein. *Biochim. Biophys. Acta* **2009**, *1787* (4), 280–288.
- (73) Bautista, J. A.; Hiller, R. G.; Sharples, F. P.; Gosztola, D.; Wasielewski, M.; Frank, H. A. Singlet and Triplet Energy Transfer in the Peridinin–Chlorophyll *a*–Protein from *Amphidinium Carterae*. *J. Phys. Chem. A* **1999**, *103* (14), 2267–2273.
- (74) Zigmantas, D.; Polívka, T.; Hiller, R. G.; Yartsev, A.; Sundström, V. Spectroscopic and Dynamic Properties of the Peridinin Lowest Singlet Excited States. *J. Phys. Chem. A* **2001**, *105* (45), 10296–10306.

- (75) Zigmantas, D.; Hiller, R. G.; Yartsev, A.; Sundström, V.; Polívka, T. Dynamics of Excited States of the Carotenoid Peridinin in Polar Solvents: Dependence on Excitation Wavelength, Viscosity, and Temperature. *J. Phys. Chem. B* **2003**, *107* (22), 5339–5348.
- (76) Zigmantas, D.; Hiller, R. G.; Sharples, F. P.; Frank, H. A.; Sundström, V.; Polívka, T. Effect of a Conjugated Carbonyl Group on the Photophysical Properties of Carotenoids. *Phys. Chem. Chem. Phys.* **2004**, *6* (11), 3009–3016.
- (77) Polívka, T.; Pascher, T.; Sundström, V.; Hiller, R. G. Tuning Energy Transfer in the Peridinin-Chlorophyll Complex by Reconstitution with Different Chlorophylls. *Photosynth. Res.* **2005**, *86* (1-2), 217–227.
- (78) Polívka, T.; Kaligotla, S.; Chábera, P.; Frank, H. A. An Intramolecular Charge Transfer State of Carbonyl Carotenoids: Implications for Excited State Dynamics of Apo-Carotenals and Retinal. *Phys. Chem. Chem. Phys.* **2011**, *13*, 10787–10796.
- (79) Chábera, P.; Durchan, M.; Shih, P. M.; Kerfeld, C. A.; Polívka, T. Excited-State Properties of the 16kDa Red Carotenoid Protein from *Arthrospira Maxima*. *Biochim. Biophys. Acta* **2011**, *1807* (1), 30–35.
- (80) Berera, R.; Gwizdala, M.; van Stokkum, I. H.; Kirilovsky, D.; van Grondelle, R. Excited States of the Inactive and Active Forms of the Orange Carotenoid Protein. *J. Phys. Chem. B* **2013**, *117* (31), 9121–9128.
- (81) Šlouf, V.; Kuznetsova, V.; Fuciman, M.; de Carbon, C. B.; Wilson, A.; Kirilovsky, D.; Polívka, T. Ultrafast Spectroscopy Tracks Carotenoid Configurations in the Orange and Red Carotenoid Proteins from Cyanobacteria. *Photosynth. Res.* **2017**, *131* (1), 105–117.
- (82) Myers, A. B. Resonance Raman Intensity Analysis of Excited-State Dynamics. *Acc. Chem. Res.* **1997**, *30* (12), 519–527.
- (83) Kish, E.; Pinto, M. M.; Kirilovsky, D.; Spezia, R.; Robert, B. Echinonone Vibrational Properties: From Solvents to the Orange Carotenoid Protein. *Biochim. Biophys. Acta* **2015**, *1847*, 1044–1054.
- (84) Fujisawa, T.; Leverenz, R. L.; Nagamine, M.; Kerfeld, C. A.; Unno, M. Raman Optical Activity Reveals Carotenoid Photoactivation Events in the Orange Carotenoid Protein in Solution. *J. Am. Chem. Soc.* **2017**, *139*, 10456–10460.
- (85) McHale, J. L. *Molecular Spectroscopy*; Prentice Hall: Upper Saddle River, New Jersey, 1999.
- (86) Kelley, A. M. *Condensed-Phase Molecular Spectroscopy and Photophysics*; John Wiley & Sons: Hoboken, New Jersey, 2013.
- (87) Cunningham, F. X.; Gantt, E. A Portfolio of Plasmids for Identification and Analysis of Carotenoid Pathway Enzymes: Adonis Aestivalis as a Case Study. *Photosynth. Res.* **2007**, *92*, 245–259.

- (88) Lakowicz, J. R. *Principles of Fluorescence Spectroscopy*, 3rd ed.; Springer: New York, 2006.
- (89) Polívka, T.; Kerfeld, C. A.; Pascher, T.; Sundström, V. Spectroscopic Properties of the Carotenoid 3'-Hydroxyechinenone in the Orange Carotenoid Protein from the Cyanobacterium *Arthrospira Maxima*. *Biochemistry* **2005**, *44*, 3944–4003.
- (90) Polívka, T.; Chabera, P.; Kerfeld, C. A. Carotenoid-Protein Interaction Alters the S₁ Energy of Hydroxyechinenone in the Orange Carotenoid Protein. *Biochim. Biophys. Acta* **2013**, *1827*, 248–254.
- (91) Niedzwiedzki, D. M.; Liu, H.; Blankenship, R. E. Excited State Properties of 3'-Hydroxyechinenone in Solvents and in the Orange Carotenoid Protein from *Synechocystis* Sp. PCC 6803. *J. Phys. Chem. B* **2014**, *118* (23), 6141–6149.
- (92) De Re, E.; Schlau-Cohen, G. S.; Leverenz, R. L.; Huxter, V. M.; Oliver, T. A.; Mathies, R. A.; Fleming, G. R. Insights into the Structural Changes Occurring upon Photoconversion in the Orange Carotenoid Protein from Broadband Two-Dimensional Electronic Spectroscopy. *J. Phys. Chem. B* **2014**, *118* (20), 5382–5389.
- (93) Berman, H. M.; Westbrook, J.; Feng, Z.; Gilliland, G.; Bhat, T. N.; Weissig, H.; Shindyalov, I. N.; Bourne, P. E. The Protein Data Bank. *Nucleic Acids Res.* **2000**, *28*, 235–242.
- (94) Delano, W. L. *The PyMOL Molecular Graphics System*; DeLano Scientific: San Carlos, California, 2002.
- (95) Greco, J. A.; LaFountain, A. M.; Kinashi, N.; Shinada, T.; Sakaguchi, K.; Katsumura, S.; Magdaong, N. C.; Niedzwiedzki, D. M.; Birge, R. R.; Frank, H. A. Spectroscopic Investigation of the Carotenoid Deoxyperidin: Direct Observation of the Forbidden S₀ → S₁ Transition. *J. Phys. Chem. B* **2016**, *120*, 2731–2744.
- (96) Siano, D. B.; Metzler, D. E. Band Shapes of the Electronic Spectra of Complex Molecules. *J. Chem. Phys.* **1969**, *51*, 1856–1861.
- (97) Magde, D.; Wong, R.; Seybold, P. G. Fluorescence Quantum Yields and Their Relation to Lifetimes of Rhodamine 6G and Fluorescein in Nine Solvents: Improved Absolute Standards for Quantum Yields. *Photochem. Photobiol.* **2002**, *75*, 327–334.
- (98) Jørgensen, K.; Stapelfeldt, H.; Skibsted, L. H. Fluorescence of Carotenoids. Effect of Oxygenation and Cis/trans Isomerization. *Chem. Phys. Lett.* **1992**, *190*, 514–519.
- (99) Shimanouchi, T. Trichloromethane: Vibrational And/or Electronic Energy Levels. In *Tables of Molecular Vibrational Frequencies Consolidated Volume I*; National Bureau of Standards, 1972; pp 1–160.
- (100) Fleming, G. R.; Cho, M. Chromophore-Solvent Dynamics. *Annu. Rev. Phys. Chem.* **1996**, *47*, 109–134.

- (101) Yan, Y. J.; Mukamel, S. Photon Echoes of Polyatomic Molecules in Condensed Phases. *J. Chem. Phys.* **1991**, *94*, 179–190.
- (102) Mukamel, S. *Principles of Nonlinear Optical Spectroscopy*; Oxford University Press: New York, 1995.
- (103) Joo, T.; Jia, Y.; Yu, J.; Lang, M. J.; Fleming, G. R. Third-order Nonlinear Time Domain Probes of Solvation Dynamics. *J. Chem. Phys.* **1996**, *104* (16), 6089–6108.
- (104) Ohta, K.; Larsen, D. S.; Yang, M.; Fleming, G. R. Influence of Intramolecular Vibrations in Third-Order, Time-Domain Resonant Spectroscopies. II. Numerical Calculations. *J. Chem. Phys.* **2001**, *114* (18), 8020–8039.
- (105) Christensson, N.; Milota, F.; Nemeth, A.; Sperling, J.; Kauffmann, H. F.; Pullerits, T.; Hauer, J. Two-Dimensional Electronic Spectroscopy of Beta-Carotene. *J. Phys. Chem. B* **2009**, *113* (51), 16409–16419.
- (106) Sugisaki, M.; Fujiwara, M.; Nair, S. V.; Ruda, H. E.; Cogdell, R. J.; Hashimoto, H. Excitation-Energy Dependence of Transient Grating Spectroscopy in β -Carotene. *Phys. Rev. B Condens. Matter* **2009**, *80*, 035118.
- (107) Bagchi, B.; Fleming, G. R.; Oxtoby, D. W. Theory of Electronic Relaxation in Solution in the Absence of an Activation Barrier. *J. Chem. Phys.* **1983**, *78* (12), 7375–7385.
- (108) van der Zwan, G.; Hynes, J. T. Nonequilibrium Solvation Dynamics in Solution Reactions. *J. Chem. Phys.* **1983**, *78*, 4174–4185.
- (109) Jordanides, X. J.; Lang, M. J.; Song, X.; Fleming, G. R. Solvation Dynamics in Protein Environments Studied by Photon Echo Spectroscopy. *J. Phys. Chem. B* **1999**, *103* (37), 7995–8005.
- (110) Wilson, A.; Punginelli, C.; Couturier, M.; Perreau, F.; Kirilovsky, D. Essential Role of Two Tyrosines and Two Tryptophans on the Photoprotection Activity of the Orange Carotenoid Protein. *Biochim. Biophys. Acta* **2011**, *1807* (3), 293–301.
- (111) Bandara, S.; Ren, Z.; Lu, L.; Zeng, X.; Shin, H.; Zhao, K. H.; Yang, X. Photoactivation Mechanism of a Carotenoid-Based Photoreceptor. *Proc. Natl. Acad. Sci. U. S. A.* **2017**, *114*, 6286–6291.
- (112) Ghosh, S.; Bishop, M. M.; Roscioli, J. D.; LaFountain, A. M.; Frank, H. A.; Beck, W. F. Excitation Energy Transfer by Coherent and Incoherent Mechanisms in the Peridinin–chlorophyll *a* Protein. *J. Phys. Chem. Lett.* **2017**, *8*, 463–469.
- (113) Bishop, M. M.; Roscioli, J. D.; Ghosh, S.; Mueller, J. J.; Shepherd, N. C.; Beck, W. F. Vibrationally Coherent Preparation of the Transition State for Photoisomerization of the Cyanine Dye Cy5 in Water. *J. Phys. Chem. B* **2015**, *119*, 6905–6915.

- (114) Levine, B. G.; Ko, C.; Quenneville, J.; Martínez, T. J. Conical Intersections and Double Excitations in Time-Dependent Density Functional Theory. *Mol. Phys.* **2006**, *104* (5-7), 1039–1051.
- (115) Klessinger, M.; Michl, J. *Excited States and Photochemistry of Organic Molecules*; VCH Publishers: New York, 1995.
- (116) Birge, R. R.; Zgierski, M. Z.; Serrano-Andres, L.; Hudson, B. S. Transition Dipole Orientation of Linear Polyenes: Semiempirical Models and Extrapolation to the Infinite Chain Limit. *J. Phys. Chem. A* **1999**, *103* (14), 2251–2255.
- (117) Dolan, P. M.; Miller, D.; Cogdell, R. J.; Birge, R. R.; Frank, H. A. Linear Dichroism and the Transition Dipole Moment Orientation of the Carotenoid in the LH2 Antenna Complex in Membranes of *Rhodospseudomonas Acidophila* Strain 10050. *J. Phys. Chem. B* **2001**, *105* (48), 12134–12142.
- (118) Enriquez, M. M.; Fuciman, M.; LaFountain, A. M.; Wagner, N. L.; Birge, R. R.; Frank, H. A. The Intramolecular Charge Transfer State in Carbonyl-Containing Polyenes and Carotenoids. *J. Phys. Chem. B* **2010**, *114*, 12416–12426.
- (119) Gurchiek, J. K.; Bao, H.; Domínguez-Martín, M. A.; McGovern, S. E.; Marquardt, C. E.; Roscioli, J. D.; Ghosh, S.; Kerfeld, C. A.; Beck, W. F. Fluorescence and Excited-State Conformational Dynamics of the Orange Carotenoid Protein. *J. Phys. Chem. B* **2018**, *122* (6), 1792–1800.
- (120) Jeevarajan, A. S.; Kispert, L. D.; Avdievich, N. I.; Forbes, M. D. E. Role of Excited Singlet State in the Photooxidation of Carotenoids: A Time-Resolved Q-Band EPR Study. *J. Phys. Chem.* **1996**, *100* (2), 669–671.
- (121) Mortensen, A.; Skibsted, L. H. Kinetics of Photobleaching of β -Carotene in Chloroform and Formation of Transient Carotenoid Species Absorbing in the Near Infrared. *Free Radic. Res.* **1996**, *25* (4), 355–368.
- (122) Zhang, J.-P.; Fujii, R.; Koyama, Y.; Rondonuwu, F. S.; Watanabe, Y.; Mortensen, A.; Skibsted, L. H. The $1B_u$ -Type Singlet State of β -Carotene as a Precursor of the Radical Cation Found in Chloroform Solution by Sub-Picosecond Time-Resolved Absorption Spectroscopy. *Chem. Phys. Lett.* **2001**, *348* (3), 235–241.
- (123) Becke, A. D. Density-functional Thermochemistry. III. The Role of Exact Exchange. *J. Chem. Phys.* **1993**, *98* (7), 5648–5652.
- (124) Stephens, P. J.; Devlin, F. J.; Chabalowski, C. F.; Frisch, M. J. Ab Initio Calculation of Vibrational Absorption and Circular Dichroism Spectra Using Density Functional Force Fields. *J. Phys. Chem.* **1994**, *98* (45), 11623–11627.

- (125) Frisch, M. J.; Trucks, G. W.; Schlegel, H. B.; Scuseria, G. E.; Robb, M. A.; Cheeseman, J. R.; Scalmani, G.; Barone, V.; Petersson, G. A.; Nakatsuji, H.; Li, X.; Caricato, M.; Marenich, A. V.; Bloino, J.; Janesko, B. G.; Gomperts, R.; Mennucci, B.; Hratchian, H. P.; Ortiz, J. V.; Izmaylov, A. F.; Sonnenberg, J. L.; Williams; Ding, F.; Lipparini, F.; Egidi, F.; Goings, J.; Peng, B.; Petrone, A.; Henderson, T.; Ranasinghe, D.; Zakrzewski, V. G.; Gao, J.; Rega, N.; Zheng, G.; Liang, W.; Hada, M.; Ehara, M.; Toyota, K.; Fukuda, R.; Hasegawa, J.; Ishida, M.; Nakajima, T.; Honda, Y.; Kitao, O.; Nakai, H.; Vreven, T.; Throssell, K.; Montgomery, J. A., Jr.; Peralta, J. E.; Ogliaro, F.; Bearpark, M. J.; Heyd, J. J.; Brothers, E. N.; Kudin, K. N.; Staroverov, V. N.; Keith, T. A.; Kobayashi, R.; Normand, J.; Raghavachari, K.; Rendell, A. P.; Burant, J. C.; Iyengar, S. S.; Tomasi, J.; Cossi, M.; Millam, J. M.; Klene, M.; Adamo, C.; Cammi, R.; Ochterski, J. W.; Martin, R. L.; Morokuma, K.; Farkas, O.; Foresman, J. B.; Fox, D. J. *Gaussian 16 Rev. A.01*; Wallingford, CT, 2016.
- (126) Yanai, T.; Tew, D. P.; Handy, N. C. A New Hybrid Exchange–correlation Functional Using the Coulomb-Attenuating Method (CAM-B3LYP). *Chem. Phys. Lett.* **2004**, *393* (1), 51–57.
- (127) Lu, T.; Chen, F. Multiwfn: A Multifunctional Wavefunction Analyzer. *J. Comput. Chem.* **2012**, *33* (5), 580–592.
- (128) Cantor, C. R.; Schimmel, P. R. *Biophysical Chemistry. Part II: Techniques for the Study of Biological Structure and Function*; W. H. Freeman and Company: San Francisco, 1980.
- (129) Yu, A.; Tolbert, C. A.; Farrow, D. A.; Jonas, D. M. Solvatochromism and Solvation Dynamics of Structurally Related Cyanine Dyes. *J. Phys. Chem. A* **2002**, *106* (41), 9407–9419.
- (130) Ejder, E. Methods of Representing Emission, Excitation, and Photoconductivity Spectra. *J. Opt. Soc. Amer.* **1969**, *59* (2), 223–224.
- (131) Melhuish, W. H. Absolute Spectrofluorimetry. *J. Res. Natl. Bur. Stand.* **1972**, *76A*, 547–560.
- (132) Mooney, J.; Kambhampati, P. Get the Basics Right: Jacobian Conversion of Wavelength and Energy Scales for Quantitative Analysis of Emission Spectra. *J. Phys. Chem. Lett.* **2013**, *4* (19), 3316–3318.
- (133) Andersson, P. O.; Bachilo, S. M.; Chen, R.-L.; Gillbro, T. Solvent and Temperature Effects on Dual Fluorescence in a Series of Carotenes. Energy Gap Dependence of the Internal Conversion Rate. *J. Phys. Chem.* **1995**, *99* (44), 16199–16209.
- (134) Saito, S.; Tasumi, M.; Eugster, C. H. Resonance Raman Spectra (5800–40 cm^{-1}) of All-*trans* and 15-*cis* Isomers of β -Carotene in the Solid State and in Solution. Measurements with Various Laser Lines from Ultraviolet to Red. *J. Raman Spectrosc.* **1983**, *14*, 299–309.

- (135) Sverdlov, L. M.; Kovner, M. A.; Krař. *Vibrational Spectra of Polyatomic Molecules*; John Wiley & Sons, 1973.
- (136) Ricci, M.; Torre, R.; Foggi, P.; Kamalov, V.; Righini, R. Molecular Dynamics of β -Carotene in Solution by Resonance Enhanced Optical Kerr Effect. *J. Chem. Phys.* **1995**, *102* (24), 9537.
- (137) Bondarev, S. L.; Bachilo, S. M.; Dvornikov, S. S.; Tikhomirov, S. A. $S_2 \rightarrow S_0$ Fluorescence and Transient $S_n \leftarrow S_1$ Absorption of All-Trans- β -Carotene in Solid and Liquid Solutions. *J. Photochem. Photobiol. A Chem.* **1989**, *46* (3), 315–322.
- (138) Shreve, A. P.; Trautman, J. K.; Owens, T. G.; Albrecht, A. C. Determination of the S_2 Lifetime of β -Carotene. *Chem. Phys. Lett.* **1991**, *178* (1), 89–96.
- (139) Kochendoerfer, G. G.; Mathies, R. A. Spontaneous Emission Study of the Femtosecond Isomerization Dynamics of Rhodopsin. *J. Phys. Chem.* **1996**, *100* (34), 14526–14532.
- (140) Norden, B.; Lindblom, G.; Jonas, I. Linear Dichroism Spectroscopy as a Tool for Studying Molecular Orientation in Model Membrane Systems. *J. Phys. Chem.* **1977**, *81* (22), 2086–2093.
- (141) Niedzwiedzki, D. M.; Enriquez, M. M.; Lafountain, A. M.; Frank, H. A. Ultrafast Time-Resolved Absorption Spectroscopy of Geometric Isomers of Xanthophylls. *Chem. Phys.* **2010**, *373* (1-2), 80–89.
- (142) Dickson, A. D.; Mills, I. M.; Crawford, B. Vibrational Intensities. VIII. CH₃ and CD₃ Chloride, Bromide, and Iodide. *J. Chem. Phys.* **1957**, *27* (2), 445–455.
- (143) Durig, J. R.; Kizer, K. L.; Karriker, J. M. Spectra and Structure of Small Ring Compounds. XXXVI. 2-Methyl-1,3-Dioxolane; 2-Methyl-1,3-Dioxolane-d₄; 2-Methyltetrahydrofuran; and Methylcyclopentane. *J. Raman Spectrosc.* **1973**, *1* (1), 17–45.
- (144) Shimanouchi, T. *Tables of Molecular Vibrational Frequencies Consolidated Volume I*; National Bureau of Standards, 1972; pp 1–160.
- (145) Andersson, P. O.; Gillbro, T.; Ferguson, L.; Cogdell, R. J. Absorption Spectral Shifts of Carotenoids Related to Medium Polarizability. *Photochem. Photobiol.* **1991**, *54*, 353–360.
- (146) Qu, G.; Xin, M.; Jia, Q.; Cai, P.; Jin, G.; Zhou, Y.; Liu, C.; Tan, Y.; Zhang, Y.; Yao, Z.; Feng, A.; Cai, H. Resonance Raman Features All-Trans- β -Carotene during Phase Transition and Theoretical Investigation Analysis. *Optik* **2019**, *185*, 191–198.
- (147) Ling, A. C.; Willard, J. E. Viscosities of Some Organic Glasses Used as Trapping Matrixes. *J. Phys. Chem.* **1968**, *72* (6), 1918–1923.
- (148) Warshel, A. Bicycle-Pedal Model for the First Step in the Vision Process. *Nature* **1976**, *260* (5553), 679–683.

- (149) Liu, R. S.; Asato, A. E. The Primary Process of Vision and the Structure of Bathorhodopsin: A Mechanism for Photoisomerization of Polyenes. *Proc. Natl. Acad. Sci. U. S. A.* **1985**, *82* (2), 259–263.
- (150) Liu, R. S. H. Photoisomerization by Hula-Twist: A Fundamental Supramolecular Photochemical Reaction. *Acc. Chem. Res.* **2001**, *34* (7), 555–562.
- (151) Ostroumov, E. E.; Reus; Müller, M. G.; Michael; Holzwarth, A. R. On the Nature of the “Dark S*” Excited State of β -Carotene. *J. Phys. Chem. A* **2011**, *115* (16), 3698–3712.
- (152) Andersson, P. O.; Gillbro, T.; Asato, A. E.; Liu, R. S. H. Temperature and Viscosity Sensitive S₁ Emission from a Highly Substituted Triene. *Chem. Phys. Lett.* **1995**, *235* (1), 76–82.
- (153) Menter, J. M. Temperature Dependence of Collagen Fluorescence. *Photochem. Photobiol. Sci.* **2006**, *5* (4), 403–410.
- (154) Brocklehurst, B.; Young, R. N. Fluorescence Anisotropy Decays and Viscous Behaviour of 2-Methyltetrahydrofuran. *Journal of the Chemical Society, Faraday Transactions.* 1994, p 271. <https://doi.org/10.1039/ft9949000271>.
- (155) Palings, I.; Van den Berg, E. M. M.; Lugtenburg, J.; Mathies, R. A. Complete Assignment of the Hydrogen out-of-Plane Wagging Vibrations of Bathorhodopsin: Chromophore Structure and Energy Storage in the Primary Photoproduct of Vision. *Biochemistry* **1989**, *28* (4), 1498–1507.
- (156) Schapiro, I.; Ryazantsev, M. N.; Frutos, L. M.; Ferré, N.; Lindh, R.; Olivucci, M. The Ultrafast Photoisomerizations of Rhodopsin and Bathorhodopsin Are Modulated by Bond Length Alternation and HOOP Driven Electronic Effects. *J. Am. Chem. Soc.* **2011**, *133* (10), 3354–3364.
- (157) Andersson, P. O.; Gillbro, T.; Asato, A. E.; Liu, R. S. H. Dual Singlet State Emission in a Series of Mini-Carotenes. *J. Lumin.* **1992**, *51* (1-3), 11–20.
- (158) Malhado, J. P.; Spezia, R.; Hynes, J. T. Dynamical Friction Effects on the Photoisomerization of a Model Protonated Schiff Base in Solution. *J. Phys. Chem. A* **2011**, *115*, 3720–3735.
- (159) Minezawa, N.; Gordon, M. S. Optimizing Conical Intersections by Spin-Flip Density Functional Theory: Application to Ethylene. *J. Phys. Chem. A* **2009**, *113* (46), 12749–12753.
- (160) Kochendoerfer, G. G.; Mathies, R. A. Ultrafast Spectroscopy of Rhodopsins—photochemistry at Its Best! *Isr. J. Chem.* **1995**, *35* (3-4), 211–226.
- (161) Birge, R. R. Nature of the Primary Photochemical Events in Rhodopsin and Bacteriorhodopsin. *Biochim. Biophys. Acta* **1990**, *1016* (3), 293–327.

- (162) Kukura, P.; McCamant, D. W.; Yoon, S.; Wandschneider, D. B.; Mathies, R. A. Structural Observation of the Primary Isomerization in Vision with Femtosecond-Stimulated Raman. *Science* **2005**, *310* (5750), 1006–1009.
- (163) Schnedermann, C.; Liebel, M.; Kukura, P. Mode-Specificity of Vibrationally Coherent Internal Conversion in Rhodopsin during the Primary Visual Event. *J. Am. Chem. Soc.* **2015**, *137* (8), 2886–2891.
- (164) Hasson, K. C.; Gai, F.; Anfinrud, P. A. The Photoisomerization of Retinal in Bacteriorhodopsin: Experimental Evidence for a Three-State Model. *Proc. Natl. Acad. Sci. U. S. A.* **1996**, *93* (26), 15124–15129.
- (165) Song, L.; El-Sayed, M. A. Primary Step in Bacteriorhodopsin Photosynthesis: Bond Stretch Rather than Angle Twist of Its Retinal Excited-State Structure. *J. Am. Chem. Soc.* **1998**, *120* (34), 8889–8890.
- (166) Lewis, A.; Spoonhower, J. P.; Perreault, G. J. Observation of Light Emission from a Rhodopsin. *Nature* **1976**, *260*, 675.
- (167) Kouyama, T.; Kinosita, K., Jr; Ikegami, A. Excited-State Dynamics of Bacteriorhodopsin. *Biophys. J.* **1985**, *47* (1), 43–54.
- (168) Haran, G.; Wynne, K.; Xie, A.; He, Q.; Chance, M.; Hochstrasser, R. M. Excited State Dynamics of Bacteriorhodopsin Revealed by Transient Stimulated Emission Spectra. *Chem. Phys. Lett.* **1996**, *261* (4), 389–395.
- (169) Nosrati, M.; Berbasova, T.; Vasileiou, C.; Borhan, B.; Geiger, J. H. A Photoisomerizing Rhodopsin Mimic Observed at Atomic Resolution. *J. Am. Chem. Soc.* **2016**, *138* (28), 8802–8808.
- (170) Ghanbarpour, A.; Nairat, M.; Nosrati, M.; Santos, E. M.; Vasileiou, C.; Dantus, M.; Borhan, B.; Geiger, J. H. Mimicking Microbial Rhodopsin Isomerization in a Single Crystal. *J. Am. Chem. Soc.* **2019**, *141* (4), 1735–1741.
- (171) Bautista, J. A.; Connors, R. E.; Raju, B. B.; Hiller, R. G.; Sharples, F. P.; Gosztola, D.; Wasielewski, M. R.; Frank, H. A. Excited State Properties of Peridinin: Observation of a Solvent Dependence of the Lowest Excited Singlet State Lifetime and Spectral Behavior Unique among Carotenoids. *J. Phys. Chem. B* **1999**, *103* (41), 8751–8758.
- (172) Kirilovsky, D. Photoprotection in Cyanobacteria: The Orange Carotenoid Protein (OCP)-Related Non-Photochemical-Quenching Mechanism. *Photosynth. Res.* **2007**, *93* (1-3), 7–16.
- (173) Song, L.; El-Sayed, M. A.; Lanyi, J. K. Protein Catalysis of the Retinal Subpicosecond Photoisomerization in the Primary Process of Bacteriorhodopsin Photosynthesis. *Science* **1993**, *261* (5123), 891–894.

- (174) Magde, D.; Wong, R.; Seybold, P. G. Fluorescence Quantum Yields and Their Relation to Lifetimes of Rhodamine 6G and Fluorescein in Nine Solvents: Improved Absolute Standards for Quantum Yields. *Photochem. Photobiol.* **2002**, *75* (4), 327–334.
- (175) Ameloot, M.; vandeVen, M.; Acuña, A. U.; Valeur, B. Fluorescence Anisotropy Measurements in Solution: Methods and Reference Materials (IUPAC Technical Report). *J. Macromol. Sci. Part A Pure Appl. Chem.* **2013**, *85* (3), 589–608.
- (176) Prazeres, T. J. V.; Fedorov, A.; Barbosa, S. P.; Martinho, J. M. G.; Berberan-Santos, M. N. Accurate Determination of the Limiting Anisotropy of Rhodamine 101. Implications for Its Use as a Fluorescence Polarization Standard. *J. Phys. Chem. A* **2008**, *112* (23), 5034–5039.
- (177) Johansson, L. B.-Å. Limiting Fluorescence Anisotropies of Perylene and Xanthene Derivatives. *J. Chem. Soc. Faraday Trans.* **1990**, *86* (12), 2103–2107.